OUKA
The University of Osaka
Institutional Knowledge Archive

Title	Orientational Ordering of Partially Deuterated Methyl Groups in Molecular Solids
Author(s)	Suzuki, Hal
Citation	大阪大学, 2011, 博士論文
Version Type	VoR
URL	https://hdl.handle.net/11094/27642
rights	
Note	

The University of Osaka Institutional Knowledge Archive : OUKA

https://ir.library.osaka-u.ac.jp/

The University of Osaka

理学 1466 8

DOCTORAL THESIS

Orientational Ordering of Partially Deuterated Methyl Groups in Molecular Solids

by

Hal Suzuki

Research Center for Structural Thermodynamics

Department of Chemistry
Graduate School of Science
Osaka University

2011

DOCTORAL THESIS

Orientational Ordering of Partially Deuterated Methyl Groups in Molecular Solids

(分子固体における部分重水素化メチル基の配向秩序化)

by

Hal Suzuki

Research Center for Structural Thermodynamics

Department of Chemistry
Graduate School of Science
Osaka University

2011

Abstract

In this study, orientational ordering of partially deuterated methyl groups in solid is investigated for 4-methylpyridine, 2,6-dichlorotoluene, 2,6-dibromotoluene, toluene, methyl iodide and methanol. A combination of calorimetric methods (adiabatic and relaxation calorimetry) and infrared absorption spectroscopy is used to obtain the structural and thermodynamic information of the ordering processes.

For each compound, heat capacity measurements are made for four isotopic species (R-CH_3, R-CH_2D, R-CHD_2 and R-CD_3) in the temperature range from 0.35 K to 300 K. The temperature dependence of the heat capacity reveals how the ordering occurs. The entropies calculated from the heat capacities elucidate the degree of ordering. The infrared absorption measurements are made in the temperature range from 6 K to 100 K over the spectral range from 400 cm^{-1} to 4000 cm^{-1}. The C-H or C-D stretching modes of the methyl groups are investigated to obtain the occupancy of ground torsional levels at different orientations. The calorimetric and spectroscopic results thus obtained are verified to be consistent.

The results of the heat capacity measurements for 4-methylpyridine (C_5H_4N-CH_3) and its methyl deuterated analogs (C_5H_4N-CH_2D, C_5H_4N-CHD_2 and C_5H_4N-CD_3) reveal that three methyl-deuterated compounds undergo phase transitions below 30 K, which is not the case for C_5H_4N-CH_3. The transition entropy of C_5H_4N-CD_3 is about 3.0 J K^{-1} mol^{-1}, which is explained by the orientational ordering model of coupled methyl groups, i.e. $\Delta S = (1/2)\, R \ln 2 = 2.88$ J K^{-1} mol^{-1}. The transition entropies of C_5H_4N-CH_2D and C_5H_4N-CHD_2 are 7.9 J K^{-1} mol^{-1} and 10.1 J K^{-1} mol^{-1}, respectively. They are significantly smaller than the values expected by the coupled rotor model, i.e. $\Delta S = (1/2)\, R \ln 18 = 12.02$ J K^{-1} mol^{-1}, indicating two possibilities either freezing of the ordering process or the existence of low lying energy levels.

The methyl-partially-deuterated 2,6-dichlorotoluenes ($C_6H_3Cl_2$-CH_2D and $C_6H_3Cl_2$-CHD_2) show the Schottky heat capacity with three energy levels below 40 K. The spacing from the ground state is 267 μeV and 2950 μeV for $C_6H_3Cl_2$-CH_2D and 2400 μeV and 2700 μeV for $C_6H_3Cl_2$-CHD_2. Each of the three levels corresponds to the ground torsional state at three different orientations of the methyl groups. The excess entropies amount to $R \ln 3 = 9.13$ J K^{-1} mol^{-1}, which is due to the symmetry breaking of the methyl groups by partial deuteration. The results of the infrared spectroscopy support this interpretation. Combining the results obtained by calorimetry, infrared spectroscopy and some simple quantum mechanical calculations, the orientation of the methyl groups at low temperature is supposed to be all the protons pointing out of the molecular plane.

The methyl-partially-deuterated 2,6-dibromotoluenes ($C_6H_3Br_2$-CH_2D and $C_6H_3Br_2$-CHD_2) also show the Schottky heat capacities with three levels below 40 K, which are analogous to the results of

2,6-dichlorotoluene. The spacing from the ground state is 1200 μeV and 1700 μeV for $C_6H_3Br_2$-CH_2D and 240 μeV and 1700 μeV for $C_6H_3Br_2$-CHD_2. It is also indicated that the energy levels of $C_6H_3Br_2$-CH_2D have some density distribution in energy. Combining the results obtained by calorimetry and infrared spectroscopy, the orientation of the methyl groups at low temperature is supposed to be one proton sitting almost on the molecular plane, which is in contrast to that of 2,6-dichlorotoluene.

The methyl-partially-deuterated toluenes (C_6H_5-CH_2D and C_6H_5-CHD_2) in the α-phase also show the excess heat capacities, but the entropies are significantly less than R ln 3. The orientational ordering seems to be frozen at low temperature. This interpretation is supported by the results of the infrared spectroscopy.

The partially deuterated methyl iodides (CH_2DI and CHD_2I) also show the excess heat capacity, but only below 5 K. The excess heat capacities are fitted by a Schottky function with three levels. The spacing from the ground state is 10.5 μeV (doubly degenerated) for CH_2DI and 10 μeV and 42 μeV for CHD_2I.

The methyl-partially-deuterated methanols (CH_2DOH and CHD_2OH) in the α-phase show the Schottky heat capacity with two levels below 30 K. The spacing from the ground state is 870 μeV for CH_2DOH and 900 μeV for CHD_2OH. The upper level for CH_2DOH and the lower one for CHD_2OH are doubly degenerated. This interpretation is supported by the results of the infrared spectroscopy.

It is concluded that (1) the orientations of the deuterated methyl groups order in solids at low temperature, (2) the ordering occurs either in cooperative or non-cooperative manner, and (3) the ground torsional levels of -CH_2D and -CHD_2 depend on the orientation of the methyl groups as well as the structure of the molecular frame.

Contents

Chapter 1

Introduction

1.1 Structural Thermodynamic Study on Materials

1.1.1 Statistical-mechanical Approach

It is the main goal of condensed matter physics and physical chemistry to understand the nature of materials. It is often achieved by the agreement of microscopic picture with macroscopic experimental results. Statistical mechanics provides the framework of relating the states of microscopic units (atoms, molecules or their motions) to the states of macroscopic system. The statistical mechanical calculation starts by selecting the proper units, which gives the possible states of the system. This is usually done by quantum mechanics with the aid of structural information. Once the possible states are identified, their energy levels are calculated taking into account the interactions among elements. If many elements interact with each other at the same time, accurate estimation of the total interaction becomes extremely difficult, which is often called "many-body-problem". Usually, in such cases, some approximation or computational simulations are applied instead of the exact analytical calculations. Once the energy levels are determined, the sum of the states, called partition function, is obtained by summing up all the states with proper weighting for their energy levels. In this stage, symmetry of the system plays an important role. Since symmetry operations give indistinguishable states which cannot be counted twice, a factor called "symmetry number" has to be introduced to reduce the number of possible states. The partition function gives the free energy of the system from which all the thermodynamic quantities are derived through the thermodynamic relations. The physical quantity of interest can also be derived from them. The disadvantage of the statistical mechanics as well as the computer simulations is that the small errors in the interacting force leads to a huge difference in the macroscopic physical properties. This is because the number of elements exceeds 10^{23} and because the many-body-problem cannot be solved easily. Therefore the adequacy of the statistical model has to be checked by comparing the calculated values with the experimental results.

1.1.2 Structural Thermodynamic Study

In general, thermodynamics itself does not provide a molecular picture of nature. Therefore, in a simple system, thermodynamic quantities are used mostly to check the adequacy of the statistical models. However there are many complicated systems for which a molecular theory is not possible yet. Thus thermodynamics is advantageous because it can still be applied to such systems with confidence and exactness regardless of the complexity in molecular levels [1]. Most of thermodynamics is concerned with processes of heat. Heat is an energy transfer to the "hidden" atomic modes [2] which are not macroscopically observable. In the molecular interpretation, heat is an energy transfer through random molecular motions. Direct measurement of the heat of physical and chemical changes is called calorimetry, which is quite useful if the atomic modes of interest are "hidden". In other words, calorimetry has no selection rule. Structural thermodynamic study is a structural study based on calorimetry, which is the fundamental of this work. As mentioned above, structural information of the system is essential for connecting the microscopic picture with the macroscopic observation. In this sense, structural study and thermodynamic study complement each other. Structural thermodynamic study proposes to extract some structural insight of a condensed system from calorimetric data. It is generally quite difficult because these data involve too much information of the atomic motions which would be hidden by means of other experimental methods. However, from another point of view, this all-inclusive feature of calorimetry can be a big advantage since it definitely includes the information of the atomic motions of interest. When it is possible to separate the molecular motions properly, nothing is better than calorimetry. At low temperatures where the extent of thermal agitation is relatively small, such separation of modes is more probable.

1.2 Deuteration Effect on Phase Behavior

1.2.1 Isotope Effect

Isotopes are different types of atoms of the same chemical element, each having a different number of neutrons but the same number of protons and electrons. Since electronic states are practically independent of the number of neutrons, the chemical properties of isotopes are usually quite similar. However in some cases, isotope substitution brings dramatic change in the physical properties of materials reflecting a subtle balance of interaction. One of the well known examples is the kinetic isotope effect (KIE) characterized by the rate of chemical reaction depending on the isotope identity of an atom in the reactant. KIE is usually explained by noting that the mass of an

atom affects the vibrational frequency of the chemical bond that it forms [3]. Isotope effect on condensed phase behavior is also well known. Deuteration effect on the ferroelectric phase transition of KH_2PO_4 (KDP) is a famous example; the transition temperature of KDP is 123 K while that of the deuterated one is 220 K. The mechanism of the large deuteration effect as well as the mechanism of the transition itself, has been extensively discussed for more than 70 years, but it is still not fully understood yet [4,5].

From the view point of statistical mechanics, partial isotope substitution is an interesting topic in the way that isotopes are distinguishable to each other, even though their properties are greatly alike. Some symmetric systems consisting of the same isotopes can become asymmetric by means of partial substitution of the isotopes. For example, a fully protonated (normal) methyl group has threefold symmetry while the partially deuterated one is not symmetric, which is the main object of interest in this work.

1.2.2 Proton Tunneling and Deuteration Effect

One of the major models explaining the prominent effect of deuteration on KDP introduces the tunneling state of protons in the short hydrogen bonds [6]. Although the tunneling in KDP still remains an open problem because of the poor evidences, many kinds of deuteration effects on phase behaviors for the other tunneling systems have been discovered by Matsuo *et al.* [7]. Proton tunneling is one of the quantum mechanical features of nucleus. In general, there are three aspects of quantum features of atoms, (1) the energy quantization, (2) the symmetry of the states against changes of identical particles, and (3) the delocalization of the wave functions [8]. The first one is popular in physical chemistry, since the quantized energy levels of atomic motions, known as normal modes, are routinely detected as vibrational spectra. The second one is important when the nuclear spin states are considered. The ortho and para hydrogen may be one of the best known examples. The third one is closely related to the tunneling mode.

In spite of the quantized energy levels, the picture of classical motions of particles is usually enough to describe the atomic motion. This is because the probability density in quantum mechanics at large quantum number n is almost identical to that in classical one [9]. Thus when the temperature is high enough to give the occupancy of the higher energy levels, the classical picture is sufficient to describe the state. At low temperature, on the other hand, since only a limited number of levels with small quantum number are occupied, the shape of the quantum wave function has to be considered explicitly. If the potential barrier is high and its thickness is large at the ground level of the atomic motion, the wave functions are localized in the center of the potential wells, which is common in crystals. Then the classical picture of localized particle is again useful. Only when the potential barrier is small enough to let the wave functions spatially delocalized, the quantum mechanical

picture is needed, which is called "tunneling state".

The extent of delocalization depends also on the particle mass which gives the zero point energy levels. The smaller the mass of particle, the higher the level of zero point energy, and the more the extent of delocalization of the wave function. This is why most of the electronic states are described in this picture, although the term of "electron cloud" is more popular than "electron tunneling". For the atomic system, since the mass of nucleus is heavy, more than a thousand times greater than that of electron, only a few numbers of systems shows the tunneling states especially in solid. The proton tunneling in solid is one of such situations. For the other atoms heavier than proton, the classical picture is sufficient to describe the motion, which is true even for deuteron. This is the origin of the dramatic deuteration effect on the proton tunneling system. Once atoms are localized, the concept of "ordering" becomes effective, and sometimes order-disorder phase transitions are induced by the deuterium substitution.

1.2.3 Order-disorder Transition

Order-disorder transition is a major category of solid-solid phase transitions. Suppose a basic unit (an atom or molecule) has two or more possible positions to occupy, and these positions are equivalently occupied by the unit, then the state is called "disordered". If only one of the positions is possible, it is called "ordered". The transformation from the former to the latter state is called "ordering". The ordering is generally followed by lowering the temperature. If the ordering occurs in a cooperative manner, it is called order-disorder transition. The concept of "positions of the units" itself already premises the localization of the wave function, such that an order-disorder model holds only in the classical picture.

If there are N possible positions at high temperature phase and only one of them is possible in the low temperature phase, the transition entropy amounts to $R \ln N$ where R is the gas constant. This quantity is large comparing with the transition entropies of the other kinds such as a displacive transition, which is characteristic for the order-disorder transition.

1.3 Examples of Deuteration-induced Phase Transitions

1.3.1 Hydrogen Bonded System

Matsuo *et al.* have revealed that many hydrogen bond systems show the deuteration-induced order-disorder transitions [8]. 5-Bromo-9-hydroxyphenalenone $C_{13}H_6OOHBr$ (BHP) is a representative example [10]. BHP is a planar aromatic molecule with a short (249 pm)

intramolecular hydrogen bond. Protons in the two oxygen sites show quantum mechanical tunneling, in which the position of the proton is delocalized over the two potential wells. Overlapping of the two wave functions (tunneling state) splits the energy levels due to the orthogonality condition of eigenstates (tunnel splitting). The observation of the split levels is one of the strong evidence of tunneling state. The tunnel splitting for BHP in crystal was observed in the infrared absorption spectra and low temperature heat capacities around 64 – 83 cm^{-1} [11]. For the deuterated BHP (BDP), on the other hand, such a tunneling feature did not detected, but two phase transitions were observed by calorimetry and dielectric measurement at 33.9 K and 21.3 K [12]. Using X-ray scattering, the transitions were characterized as normal to incommesurate phase (33.9 K), and to commesurate phase (21.3 K) of deuteron positions [13]. The total transition entropy (6.8 J K^{-1} mol^{-1}) is close to R ln 2 = 5.76 J K^{-1} mol^{-1}, showing that the transition is an order-disorder type where deuteron can occupy two sites of potential wells in the high temperature phase and only one of them is possible in the low temperature phase.

Deuteration-induced transitions in the hydrogen bond system are also known for tri-alkali hydrogen disulfates and similar diselenates as well as chromous acid [14].

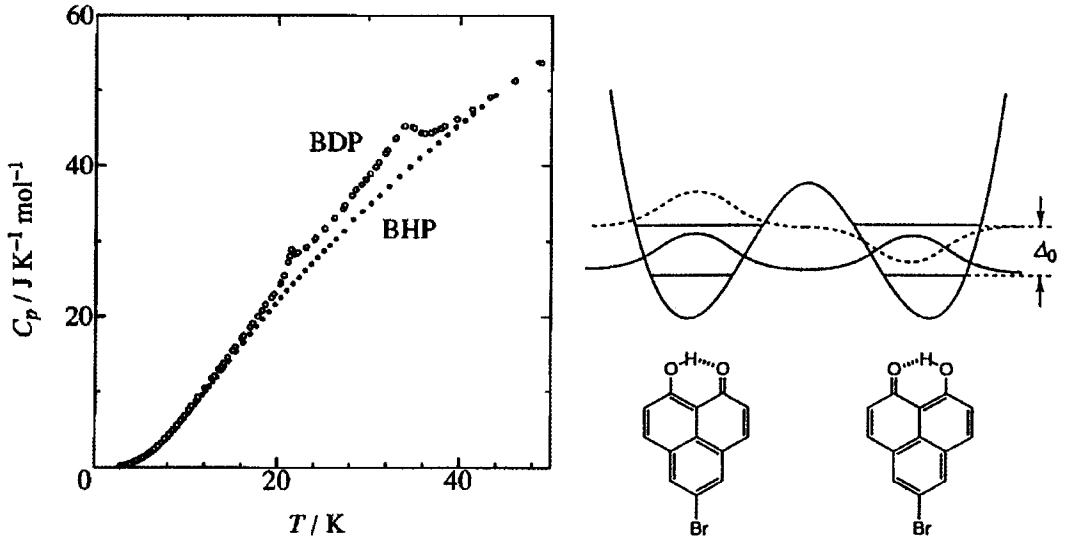

Fig. 1.1 Heat capacities of BHP and BDP (left) [10] and schematic presentation of a double minimum potential for the proton in the intramolecular hydrogen bond of BHP (right) [8]. Wave functions of the ground and excited states are also shown.

1.3.2 Ammonium System

Many compounds with ammonium ions show the rotational tunneling in the solid phase. Those ammonium system also shows dramatic deuteration effect on the phase behavior, which appears in various ways. For example, $(ND_4)_2PtCl_6$ shows an orientational order-disorder transition of ND_4^+, which is absent for $(NH_4)_2PtCl_6$ [15]. Meanwhile, $(ND_4)_2IrCl_6$ does not show a phase transition, and the ND_4^+ ions remain the tunneling state even though the energy spacing between the tunnel levels dramatically decreases [8].

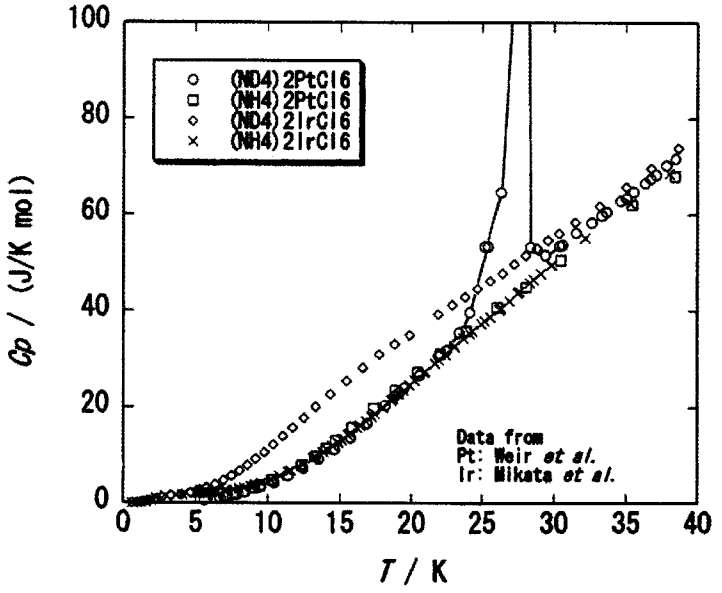

Fig. 1.2 Heat capacities of $(NH_4)_2PtCl_6$, $(ND_4)_2PtCl_6$, $(NH_4)_2IrCl_6$, and $(ND_4)_2IrCl_6$ [8].

1.3.3 Methyl Group System

A number of organic compounds with methyl groups have been investigated on their rotational tunneling states [16]. Lithium acetate dihydrate $LiCH_3COO{\cdot}2H_2O$ (LiAc) is a prototypical system for complex dynamics of methyl rotors showing a tunneling transition at 250 μeV, the second largest value ever known for methyl groups [17]. The symmetry of the fully protonated crystal is *Cmmm* at temperatures between 1 K and 300 K. The methyl groups are arranged in face-to-face coaxial pairs. The distance between carbon atoms in the coupled pair is 3.3 Å, which is shorter than the normal van der Waals distance of about 4 Å. The difference Fourier map obtained from single crystal neutron diffraction data reveals full delocalization of the protons in the rotational plane of the methyl groups, even at the lowest temperatures. The fully deuterated LiAc, on the other hand, has a phase transition

at 17.5 K, changing from *Cmmm* ($T > T_c$) to *Pman* ($T < T_c$) symmetry accompanied by the orientational ordering of coupled -CD_3 groups. The density distribution of the deuterium atoms in the -CD_3 group, obtained by single crystal neutron diffraction measurements, show three maxima at 4 K, while which are six at 40 K, indicating that the methyl groups can occupy two configurations at $T < T_c$, rotated by 60° with respect to each other [18,19]. The transition entropy for the methyl-deuterated LiAc, obtained from heat capacity measurements, is about (1/2) R ln 2 = 2.88 J K^{-1} mol^{-1}, which supports the results of neutron diffraction that the transition is of the order-disorder type for the coupled methyl rotors [20]. Recent heat capacity measurements revealed that LiAc with partially deuterated methyl groups, -CH_2D or -CHD_2, also undergoes a phase transition [21]. The transition entropies are close to (1/2) R ln 18 = (1/2) R ln 2 + R ln 3 for both compounds, indicating that the transitions discovered are also of the order-disorder type. The additional contribution of R ln 3 derives from the breaking of three-fold symmetry of the rotor by the partial deuteration.

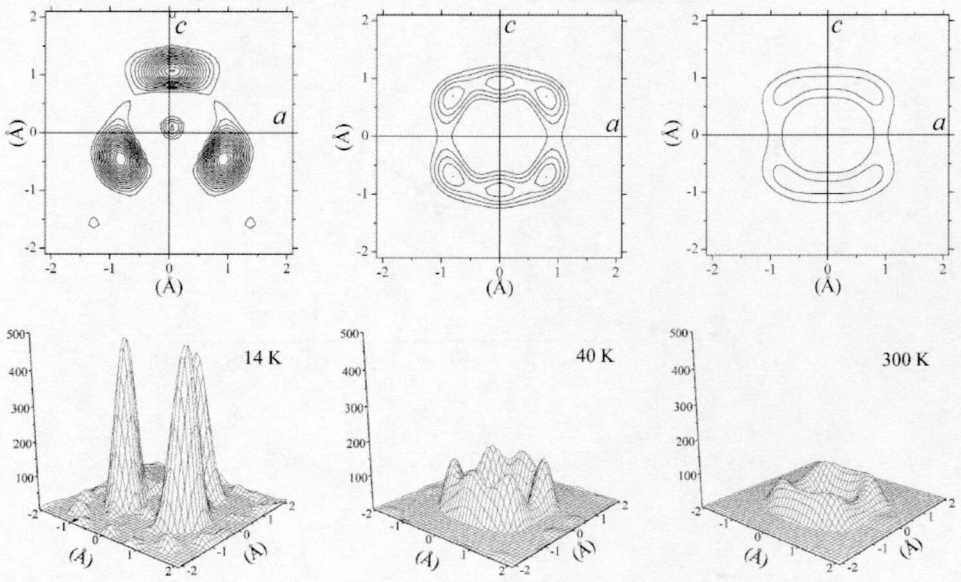

Fig. 1.3 Nuclear densities of the deuterium atoms of the fully deuterated methyl groups for LiAc at 14 K (space group *Pman*), 40 and 300 K (space group *Cmmm*) [18].

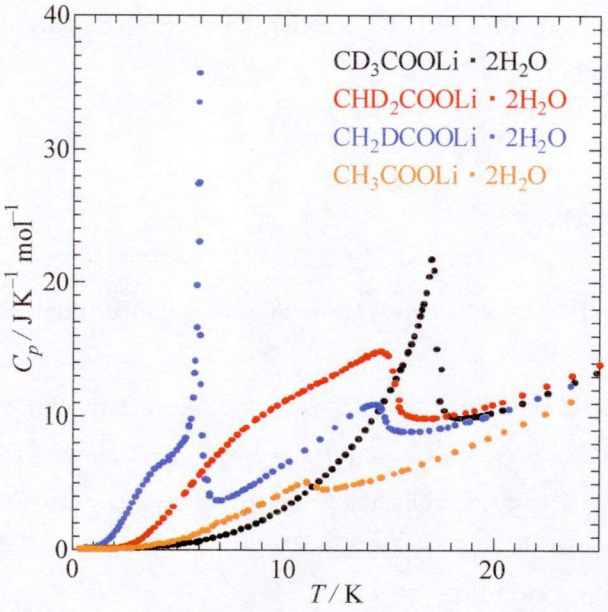

Fig. 1.4 Low temperature heat capacities of LiAc and its methyl deuterated analogs [21].

1.4 Aim of this Study

This work focuses on the behavior of (partially) deuterated methyl groups. The deuteration induced transitions of hydrogen bonded systems are mainly due to the mass effect of deuteration. For methyl group system where three protons are involved, it is possible to partially deuterate the rotor by substituting one or two protons with deuterons. The partial deuteration was expected to have additional effect on the phase behavior originating from the change in configurational symmetry. Indeed the excess entropy of R ln 3 for the partially deuterated LiAc, other than the contribution of (1/2)R ln 2, is the result of this contribution. Such a deuteration effect is not possible for the hydrogen bond system in double wells, such as BHP, where only one atom is associated with the ordering process. The partial deuteration is also possible for ammonium systems as well as hydrogen bond network systems, but the investigations for these systems are rather difficult because the protons (deuterons) in N-H (N-D) or in O-H (O-D) interchange with each other among the molecules. In contrast, protons (deuterons) in C-H (C-D) never interchange with each other unless it undergoes chemical reactions. Methyl group systems are thus ideal for these investigations.

The aim of this study is to reveal the detail of the ordering processes of partial deuterated methyl groups in molecular solids by structural thermodynamic investigations. Calorimetry was mainly used as experimental techniques. This is because (1) the ordering process is not directly observable by spectroscopy, (2) the values of entropy associated with the ordering processes provide the number of possible states at disordered state, and (3) the ordering occurs at low temperatures

where the separation of the modes is more probable. In addition, infrared (IR) absorption measurements were also made to detect the ordering processes indirectly through the vibrational modes of C-H (C-D) stretching.

1.5 References for Chapter 1

[1] T.L. Hill, *An Introduction to Statistical Thermodynamics* (Dover Publications, Inc., New York, 1986).

[2] H.B. Callen, *Thermodynamics* (John Wiley & Sons, Inc., New York, 1960)

[3] *Isotopes in Organic Chemistry, Vol. 2, Isotopes in Hydrogen Transfer Process*, ed. by E. Buncel and C.C. Lee (Elsevier Scientific Publishing Company, Amsterdam, 1976).

[4] T. Matsubara. *Jpn. J. Appl. Phys.* (Suppl. **24**-2), (1985) 1.

[5] T. Matsuo, *Netsu Sokutei* **31** (2004) 133.

[6] R. Blinc and D. Hadzi, *Hydrogen Bonding* (Pergamon Press, London New York, 1959).

[7] *Atom Tunneling Phenomena in Physics, Chemistry and Biology* ed. by T. Miyazaki (Springer-Verlag, Berlin Heidelberg New York, 2003).

[8] T. Matsuo, *Pure Appl. Chem.* **75** (2003) 913.

[9] L.I. Schiff, *Quantum Mechanics* (McGraw-Hill, New York, 1968).

[10] T. Matsuo, K. Kohno, A. Inaba, T. Mochida, A. Izuoka and T. Sugawara, *J. Chem. Phys.* **108** (1998) 9809.

[11] T. Matsuo, K. Kohno, M. Ohama, T. Mochida, A. Izuoka and T. Sugawara, *Europhys. Lett.* **47** (1999) 36.

[12] Y. Moritomo, Y. Tokura, T. Mochida and T. Sugawara, *J. Phys. Soc. Jpn.* **64** (1995) 1892.

[13] I. Tamura, Y. Noda, Y. Koroiwa, T. Mochida and T. Sugawara, *J. Phys.: Condens. Matter* **12** (2000) 8345.

[14] T. Matsuo, T. Maekawa A. Inaba, O. Yamamuro, M. Ohama, M. Ichikawa and T. Tsuchida, J. *Mol. Struct.* **790** (2006) 129.

[15] R. Weir and E.F. Westrum, Jr, *J. Chem. Thermodyn.* **34** (2002) 133.

[16] M. Prager and A. Heidemann, *Chem. Rev.* **97** (1997) 2933.

[17] P. Schiebel, G.J. Kearley and M. R. Johnson, *J. Chem. Phys.* **108**, (1998) 2375.

[18] B. Nicolai, A. Cousson and F. Fillaux, *Chem. Phys.* **290** (2003) 101.

[19] G.J. Kearley, B. Nicolai, P. G. Radaelli and F. Fillaux, *J. Solid State Chem.* **126** (1996) 184.

[20] F. Schroder, B. Winkler, E. Haussuhl, P.T. Cong, B. Wolf, M. Avalos-Borja, M. Quilichini and B. Hennion, *J. Chem. Thermodyn.* **42** (2010) 957.

[21] A. Inaba, unpublished.

Chapter 2

Theories for Molecular Rotation and Torsion

2.1 Single Particle Rotation

The rotational motion of single molecule in its surroundings (crystal field or intramolecular field) is described by the model of "single particle rotation" [1], in which the surroundings are approximated as an angle-dependent potential consisting of a time-independent part, V_{st}, and a fluctuating part, V_{fl}. Single particle rotations can be categorized to classical diffusive rotations at high temperature and quantum-mechanical rotations at low temperature (Table 2.1).

At high temperatures in crystal, the transition between the rotational states and the phonon states occurs frequently, and thus the fluctuation potential, V_{fl}, is strong. If the static potential, V_{st}, is weak, a diffusion of the molecules with respect to their angular degrees of freedom takes place. Plastic crystal phase is one of such states. In the limit of very strong static potential, V_{st}, the molecules are confined to a discrete number of equilibrium orientations which are occupied at random. Transitions across the barriers separating the equilibrium orientations occur by thermally activated jumps. In this limit the classical diffusive motion is called jump diffusion or molecular reorientation.

At low temperatures, only few lattice phonon modes are populated and the system is close to its rotational ground state, therefore the V_{fl} is weak. If V_{st} is large enough to localize the rotational wave functions in the potential wells, the system is orientationally ordered, in the classical regime, where only the excitation of the rotational vibration in the potential wells remains, which is called torsion or libration. This is the most probable case in crystal at low temperature. In the limit of $V_{st} \rightarrow \infty$, the torsional mode approximates to harmonic oscillations about the potential minima. Then the energy states are expressed by the same form of normal harmonic vibrations,

$$E = (n + \frac{1}{2})h\nu \qquad (n = 0, 1, 2, \cdots), \tag{2.1}$$

where n is the quantum number, h is the Plank constant and ν is the torsional frequency.

If V_{st} is smaller than the rotational constant, particles rotate in the framework of quantum mechanics, that is, the localized wave functions in the wells overlap to each other inducing the

splitting of energy levels. This situation is called "rotational tunneling state". The observation of the tunnel excitation is an important evidence of tunneling state, which can be done by high resolution neutron scattering, nuclear magnetic resonance or heat capacity measurement.

The overlap of the wave functions increases with decreasing V_{st}, and the dynamics gets close to the free rotation in the limit of $V_{st} = 0$ where the eigenvalues are expressed as,

$$E = \frac{m_l{}^2 \hbar^2}{2I} \qquad (m_l = 0, \pm 1, \pm 2, \cdots) \tag{2.2}$$

for the one-dimensional rotation, in which m_l is the quantum number, $\hbar$ is the Plank constant divided by 2π and I is the moment of inertia of the rotor. For the three-dimensional rotation, the eigenvalues are expressed as,

$$E = l(l+1)\frac{\hbar^2}{2I} \qquad (l = 0, 1, 2, \cdots). \tag{2.3}$$

Each level with quantum number l is degenerated by $(2l+1)$-fold. The rotational states of simple molecules in the gas phase are usually described by this model.

Table 2.1 Classification of single particle rotations in molecular crystals in terms of the rotational potential by Press [1]. Different characteristic situations may be distinguished depending on the magnitude of the static and fluctuating part of the potential.

		fluctuating potential (V_{fl})	
		strong	weak
static potential (V_{st})	strong	rotational jump	torsion (libration) rotational tunneling
	weak	rotational diffusion	quantum-mechanical free rotation

2.2 Rotational States of Methyl Groups

A methyl group can be regarded as a one-dimensional rotor. The rotational wave function ψ can be calculated by solving the Schrödinger equation,

$$H_R\psi = \left[-\left(\frac{\hbar^2}{2I}\right)\frac{d^2}{d\alpha^2} + V_{st}(\alpha)\right]\psi = E\psi\,, \tag{2.4}$$

where $V_{st}(\alpha)$ is the static potential given as a function of the rotation angle α and I is the moment of

inertia of a methyl group, $I = 5.31\times10^{-47}$ kg m^2. This equation is valid when the temperature is low enough that the fluctuation potential V_{fl} is negligible. If a methyl group is rigid to have a static barrier potential with three-fold symmetry, which is the simplest and most general case, the potential can be written as,

$$V_{st}(\alpha) = \frac{V_3}{2}[1 - \cos(3\alpha)]. \tag{2.5}$$

Then the Schrödinger equation reduces to the Mathieu equation, which can be solved analytically. The lower energy eigenvalues of the equation are shown in Fig. 2.1 [2]. In the limit of weak rotational potential, the eigenstates approach to Eq. (2.1), while in the limit of strong rotational potential, the energy levels are described by Eq. (2.2). In the intermediate regime, the eigenvalues are in between the two limits. Within the framework of pocket states, in which wave functions are centered at the minima of a given rotational potential (potential pocket), the total wave function is expressed by the overlap of wave functions and the tunnel splitting is characterized by the symmetry of the states. In the case of three-fold symmetry of the states, the torsional states split into two levels of A and E symmetry, reflecting the irreducible representation of the symmetry group C_3. The E state is doubly degenerated, having symmetry E_a and E_b. The A state is not degenerated and the energy level is the lowest. This is reversed in the first excited torsional state.

Since proton possesses a half-integer nuclear spin value ($I = 1/2$), their spin functions also have to be accounted. If the rotational potential barrier has a three-fold symmetry as above, nuclear symmetry group is also C_3. The nuclear eigenfunctions can be classified as in Table 2.2, according to the irreducible representations of C_3. The A-type eigenfunctions are four-fold degenerate ($I = 3/2$), while the E-type eigenfunctions are doubly degenerate ($I = 1/2$). The total eigenfunction can be expressed as the product of nuclear and rotational eigenfunctions. A single permutation produces a mirror reflection of the frame of the proton triangle, and this operation is not compatible with pure rotation. Two subsequent proton permutations, on the other hand, leave the frame of proton triangle invariant, and it is compatible with a rotation. Therefore, only an even number of permutation should be considered. According to the Pauli's exclusion principle, even number of proton permutations demand that the total eigenfunction must be symmetric, i.e. its representation must be A. Table 2.3 shows the product group table of $C_3 \times C_3$, and it is obvious from this table that the allowed combinations are $A \times A$, $E_a \times E_b$ and $E_b \times E_a$. As a result, all levels are equally degenerated.

The tunnel excitation from A state to E state coincides with a flipping of a nuclear spin. Since nuclear spins have extremely weak interactions with the vibrational or rotational motions of its surrounding particles as well as the electronic states, the spin conversion takes long time, unless there are any intermediates. In the neutron scattering measurement, neutron spin interacts with the nuclei of proton, so the tunnel excitation is observable. In the calorimetric measurement, on the other hand, since there are no such interactions, the spin conversion takes extremely long time.

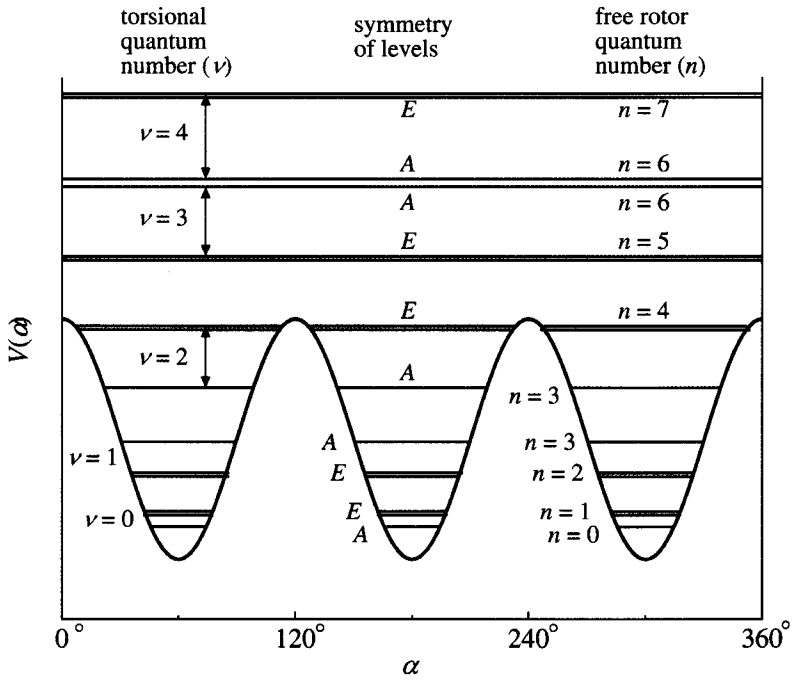

Fig. 2.1 Torsional energy levels for a threefold symmetric rotor in a potential, showing the correlation between the hindered internal rotation quantum number (ν) and the free rotation quantum number (n) [2].

Table 2.2 Spin functions $\chi(\Gamma_s, m_I)$ of methyl groups [1]. I denotes the total nuclear spin of the molecule, m_I is its z component, $\alpha = 1/2$ and $\beta = -1/2$ are the z component of the proton spins, Γ_s labels the symmetry of the wave functions and $\varepsilon = -1/2 + i\sqrt{3}/2$.

	m_I	$\chi(\Gamma_s, m_I)$
type A	3/2	ααα
	1/2	$(1/\sqrt{3})(\alpha\alpha\beta+\alpha\beta\alpha+\beta\alpha\alpha)$
$I = 3/2$	−1/2	$(1/\sqrt{3})(\beta\beta\alpha+\beta\alpha\beta+\alpha\beta\beta)$
	−3/2	βββ
type E	1/2	$(1/\sqrt{3})(\alpha\alpha\beta+\varepsilon\cdot\alpha\beta\alpha+\varepsilon^*\cdot\beta\alpha\alpha)$
	−1/2	$(1/\sqrt{3})(\beta\beta\alpha+\varepsilon\cdot\beta\alpha\beta+\varepsilon^*\cdot\alpha\beta\beta)$
$I = 1/2$	1/2	$(1/\sqrt{3})(\alpha\alpha\beta+\varepsilon^*\cdot\alpha\beta\alpha+\varepsilon\cdot\beta\alpha\alpha)$
	−1/2	$(1/\sqrt{3})(\beta\beta\alpha+\varepsilon^*\cdot\beta\alpha\beta+\varepsilon\cdot\alpha\beta\beta)$

Table 2.3 The product group table of $C_3 \times C_3$.

	A	E_a	E_b
A	A	E_a	E_b
E_a	E_a	E_b	A
E_b	E_b	A	E_a

2.3 Deuteration Effects on the Rotational States of Methyl Groups

There are three kinds of deuteration effects on the methyl groups with rotational tunneling. The first one is the mass effect as observed in the hydrogen bond systems. The torsional ground levels get lower with increasing moment of inertia. The depression of energy levels reduces the overlapping of the wave functions making the atoms more localized in the potential wells.

The second one is the alternation of the nuclear spin states. Since deuteron has three spin states (I = –1, 0, 1), the form of tunnel splitting becomes more complicated. In addition, since deuteron is Boson, the quantum symmetry restriction works in a different way from that of proton. Meanwhile calorimetric observation of the tunnel excitation becomes possible when the rotor is partially deuterated because the spin symmetry differs from the rotational symmetry.

The third effect of the deuteration is the symmetry breaking of methyl groups by partial deuteration, such as -CH_2D or -CHD_2. Classical statistical mechanics tells that the breaking of symmetry brings additional rotational entropy by R ln 3 (Section 2.5). Furthermore since deuteron has twice a mass of proton, the center of rotation for the partially deuterated methyl groups is not at the center of gravity of the rotor, which causes the angle dependence of effective moment of inertia. Here two models are introduced which describes the rotational wave functions for the asymmetric rotors.

2.4 Models for the Rotational States of Partially Deuterated Methyl Groups

2.4.1 Rigid-top-rigid-frame Model

The rigid-top-rigid-frame model [5-11] amenably solves the Schrödinger equation of the total system with simplified molecular structure consisting of a rigid-top and a rigid-frame; both are connected by a chemical bond around which the system may rotate (Fig. 2.2). After separating out the contributions of the translational modes of the whole molecule as well as the internal vibrations,

the molecule has four degrees of freedom, i.e. three modes of over-all rotation and one internal rotation.

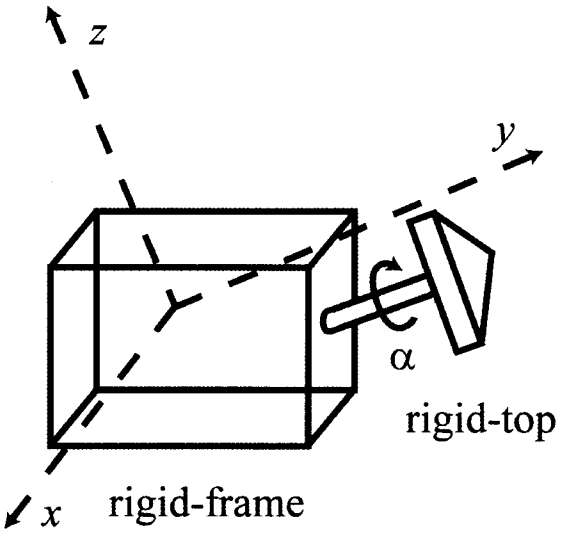

Fig. 2.2 Schematic picture of a molecule used in the rigid-top-rigid-frame model.

In classical mechanics, the kinetic energy of such a system is given by,

$$T = \left(\frac{1}{2}\right)\boldsymbol{\omega}^{+} \cdot \mathbf{I} \cdot \boldsymbol{\omega}, \tag{2.6}$$

where **I** is the inertial tensor and ω is the angular velocity vector. If the top is symmetric, **I** and ω are defined as follows,

$$\boldsymbol{\omega} = \begin{pmatrix} \omega_a \\ \omega_b \\ \omega_c \\ \dot{\alpha} \end{pmatrix}, \tag{2.7}$$

$$\mathbf{I} = \begin{pmatrix} I_a & 0 & 0 & \lambda_a I_\alpha \\ 0 & I_b & 0 & \lambda_b I_\alpha \\ 0 & 0 & I_c & \lambda_c I_\alpha \\ \lambda_a I_\alpha & \lambda_b I_\alpha & \lambda_c I_\alpha & I_\alpha \end{pmatrix}. \tag{2.8}$$

$\dot{\alpha}$ is the angular velocity of the top relative to the frame, ω_i and I_i are the angular velocity and the moment of inertia of the ith principal axis respectively, and λ_i is the directional cosine between internal rotor and the ith principal axis. This formula is convenient since the principal axes are independent of the angle of the internal rotation α. If however the top is asymmetric, the construction of **I** has to be started from the beginning where the principal axes are no longer useful,

$$\mathbf{I} = \begin{pmatrix} I_{xx} & -I_{xy} & -I_{xz} & -I_{x\alpha} \\ -I_{xy} & I_{yy} & -I_{yz} & -I_{y\alpha} \\ -I_{xz} & -I_{yz} & I_{zz} & -I_{z\alpha} \\ -I_{x\alpha} & -I_{y\alpha} & -I_{z\alpha} & I_{\alpha} \end{pmatrix}. \tag{2.9}$$

All the elements of **I** depend on the angle of the internal rotation α. Using this matrix and the Eq. (2.6), the kinetic energy can be expressed in terms of the components of angular momentum as

$$T = \sum_{i,j} \mu_{ij}(P_i - p_i)(P_j - p_j) + \mu p^2, \qquad (i,j = x,y,z) \tag{2.10}$$

where P_x, P_y and P_z are the components of total angular momentum and p_x, p_y, and p_z are the components of the internal angular momentum. p is the internal angular momentum which is conjugate to the coordinate of the internal motion. μ_{ij} is the component of inverse inertia tensor for the over-all rotation and μ is that of internal rotation. The kinetic energy operator for the quantum mechanics has then the form,

$$T = g^{-\frac{1}{4}} \sum_{i,j} (P_i - p_i)\mu_{ij} g^{\frac{1}{2}} (P_j - p_j) g^{-\frac{1}{2}} + g^{-\frac{1}{4}} p\mu g^{\frac{1}{2}} p g^{-\frac{1}{2}}, \tag{2.11}$$

where g is the inverse to the determinant of μ_{ij}. It is notable that μ_{ij}, g and p_i are functions of the angle of internal rotation α. The total Hamiltonian operator is finally obtained by adding the potential energy of the top $V(\alpha)$ to this kinetic energy component, which can be parted into three terms.

$$H = H_{\mathrm{R}} + H_{\mathrm{T}} + H_{\mathrm{TR}}. \tag{2.12}$$

H_{R} is a function independent of the internal coordinate α, and thus depends only on the over-all rotational quantum numbers. H_{T} is a function only of α, and therefore independent of the over-all rotation. H_{TR} represents the coupling between the internal and over-all motion. H_{R} and H_{TR} are dependent on P_i, while H_{T} is independent of P_i. The explicit form of H_{T} is as follows,

$$H_{\mathrm{T}} = g^{-\frac{1}{4}} \sum_{i,j} p_i \mu_{ij} g^{\frac{1}{2}} p_j g^{-\frac{1}{2}} + g^{-\frac{1}{4}} p\mu g^{\frac{1}{2}} p g^{-\frac{1}{2}} + V(\alpha). \tag{2.13}$$

In general, the deuterium substitution in the methyl top is independent of the charge distribution in the molecule, so that the conventional threefold barrier potential can also be assumed for the asymmetric rotor. Taking Eq. (2.4) as the potential $V(\alpha)$, Eq. (2.13) can be simplified to the form,

$$\begin{aligned} H_{\mathrm{T}} &= \mu_{\mathrm{T}}^{(0)} p^2 + \mu_{\mathrm{T}}^{(1)} (\cos\phi \cdot p^2 + p^2 \cdot \cos\phi) \\ &\quad + \mu_{\mathrm{T}}^{(2)} (\sin^2\phi \cdot p^2 + p^2 \cdot \sin^2\phi) + \frac{1}{2} V_3 (1 - \cos 3\phi)' \end{aligned} \tag{2.14}$$

where $\mu_{\mathrm{T}}^{(0)}$, $\mu_{\mathrm{T}}^{(1)}$ and $\mu_{\mathrm{T}}^{(2)}$ are the coefficients. It is crucial here that H_{T} is no longer invariant under a

rotation of 120°, which follows from the fact that the internal rotor is not a symmetric top.

If the angular dependent terms of H_T, the second and the third terms of Eq. (2.14), are negligible, the Hamiltonian converts into a simpler form,

$$H_T = \mu_T^{(0)} p^2 + \frac{1}{2} V_3 (1 - \cos 3\phi) = \mu_T^{(0)} \frac{d^2}{d^2\phi} + \frac{1}{2} V_3 (1 - \cos 3\phi), \qquad (2.15)$$

which is the same to Eq. (2.4). As described above, this gives two types of eigenvalues, a non-degenerated level (*A* type) and a two-fold degenerated level (*E* type). When the angular dependent terms are included in the H_T, the degeneracy is completely removed. For the ground torsional state $n = 0$, there are three substates which are often denoted by 0_0, 0_+ and 0_-.

The details of H_R and H_{TR} are not described here, but it should be noted that the coupling between the rotation and torsion is not necessarily small, which depends on the axes to be taken. H_{TR} is usually calculated as a perturbation.

2.4.2 Application of Rigid-top-rigid-frame Model

The rigid-top-rigid-frame model has been used mainly for the determination of rotational states of simple molecules in the gas phase. The investigation on acetaldehyde is one of the well known examples, which explained the experimental results of microwave spectroscopy [5]. Acetaldehyde has a planar CHO group giving plane symmetric field on the methyl groups. From the theoretical calculation described above, three ground torsional states are obtained, two of which are almost degenerated, 0_+ and 0_-, and one is non-degenerated, 0_0. There are two possible isomeric configurations, one case is that the deuteron opposes the oxygen on the frame, and the other one is that the proton of the top opposes the oxygen (Fig. 2.3). The former is called "symmetrical" configuration, while the latter "asymmetrical" one. The 0_0 state corresponds to the symmetrical configuration and the 0_+ and 0_- states are those of asymmetrical ones. The separation of energy levels between E_{0+} (E_{0-}) and E_{00} is much greater than that between E_{0+} and E_{0-}. The former values $|E_{0\pm} - E_{00}|$ for CH_2DCHO and CHD_2CHO are calculated to be about 50 GHz (~200 μeV) and 35 GHz (~150 μeV) respectively, and the latter values $|E_{0+} - E_{0-}|$ for the same compounds are 444 MHz (~1.8 μeV) and 249 MHz (~1.0 μeV) respectively. Using these calculated values, the microwave spectra for CH_2DCHO and CHD_2CHO are successfully assigned [10]. Similar assignments are also made on ortho-fluorotoluene with partially deuterated methyl groups, in which $|E_{0\pm} - E_{00}|$ is about 11 GHz (~44 μeV) for $C_5H_4F\text{-}CH_2D$ and 6 GHz (~ 24 μeV) for $C_5H_4F\text{-}CHD_2$, respectively [11].

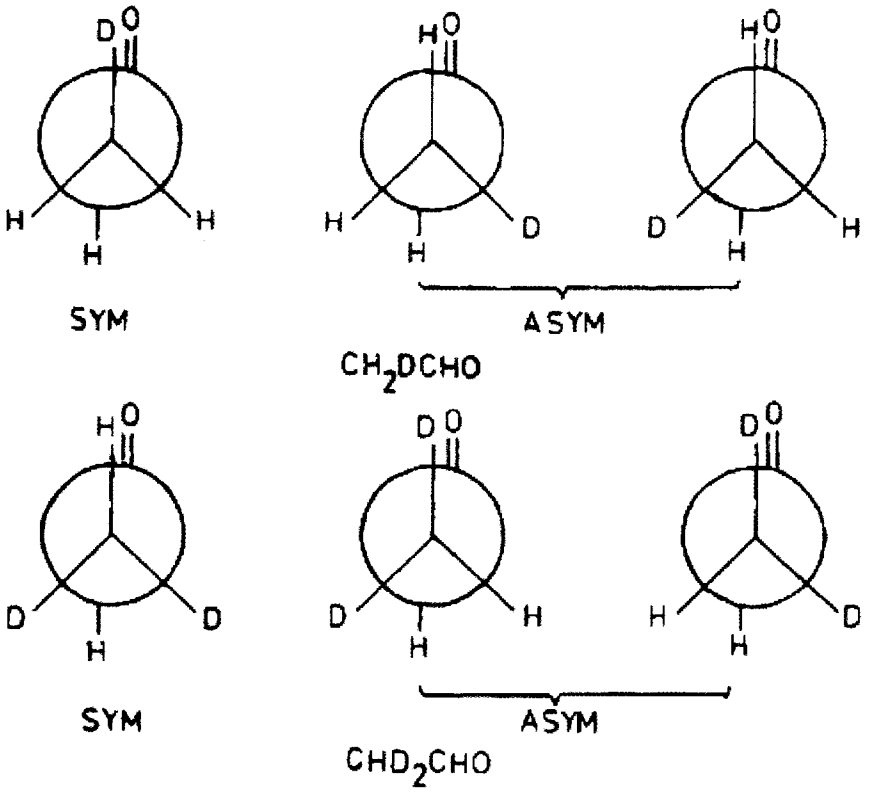

Fig. 2.3 Symmetrical and asymmetrical conformations of CH_2DCHO and CHD_2CHO viewed along C-C bond [10].

2.4.3 Pocket State Theory

As an approximate method for the analysis of ground torsional states for the simple rotors, the pocket states theory [12,13] is useful when the potential barrier of the rotation is extremely high.

In this theory, rotational wave functions are expressed as linear combinations of the localized functions ϕ_i (pocket states) which correspond to the different orientations of the rotor (Fig. 2.4). If the rotational Hamiltonian matrix elements are defined as,

$$\langle \phi_i | H | \phi_j \rangle = H_{ij}, \tag{2.16}$$

then the diagonal elements of H_{ii} describes the pocket state energy, while the H_{ij} $(i \neq j)$ represents the overlap of the pocket state functions which brings the tunnel splitting. In the case of methyl group, there are three pocket states, ϕ_1, ϕ_2 and ϕ_3 corresponding to the three orientations, so the Hamiltonian can be described as,

$$H_T = \begin{pmatrix} H_{11} & H_{12} & H_{13} \\ H_{12} & H_{22} & H_{23} \\ H_{13} & H_{23} & H_{33} \end{pmatrix}. \tag{2.17}$$

If the three orientations are equivalent as in the case of -CH_3,

$$H_{11} = H_{22} = H_{33} (= a) \tag{2.18}$$

$$H_{12} = H_{23} = H_{13} (= h), \tag{2.19}$$

then the matrix is

$$H_T = \begin{pmatrix} a & h & h \\ h & a & h \\ h & h & a \end{pmatrix}. \tag{2.20}$$

This matrix can be diagonalized to give the eigenvalues as well as the eigenstates.

$$\begin{cases} \psi_A = \frac{1}{\sqrt{3}}(\phi_1 + \phi_2 + \phi_3), & E_A = a + 2h, \\ \psi_{E_1} = \frac{1}{\sqrt{3}}(\phi_1 - \phi_2 + \phi_3), & E_{E_1} = a - h, \\ \psi_{E_2} = \frac{1}{\sqrt{3}}(\phi_1 + \phi_2 - \phi_3), & E_{E_2} = a - h, \end{cases} \tag{2.21}$$

which give the same results to those in Section 2.2.

If two of the three orientations are equivalent, e.g. -CH_2D connected to a planar frame,

$$\begin{cases} H_{11} = a, \\ H_{22} = H_{33} = b, \\ H_{12} = H_{23} = h, \\ H_{13} = f, \end{cases} \tag{2.22}$$

then the matrix is

$$H_T = \begin{pmatrix} a & h & h \\ h & b & f \\ h & f & b \end{pmatrix}, \tag{2.23}$$

and the eigenvalues are as follows,

$$\begin{cases} E_1 = b - f \\ E_2 = \dfrac{a+b+f+\sqrt{(a-b-f)^2+8h^2}}{2} \\ E_3 = \dfrac{a+b+f-\sqrt{(a-b-f)^2+8h^2}}{2} \end{cases}. \tag{2.24}$$

When the rotational tunneling is negligibly small, the rotational energy levels approach to the pocket state levels, i.e. E_1 and E_3 tend to b while E_2 tends to a. The former two states correspond to the state of $0_\pm$ and the latter one to the 0_0 in the previous section. Fig. 2.5 shows the energy levels depending on the magnitude of tunneling h and f, in which the values of two elements are assumed to be the same, i.e. $h = f$.

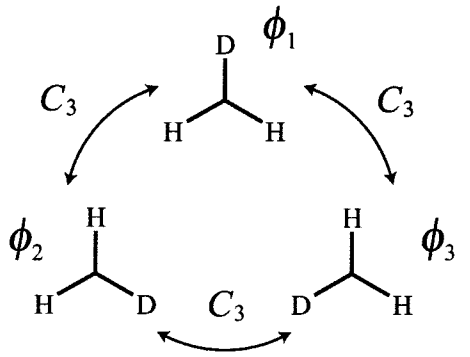

Fig. 2.4 The threefold rotations of -CH_2D.

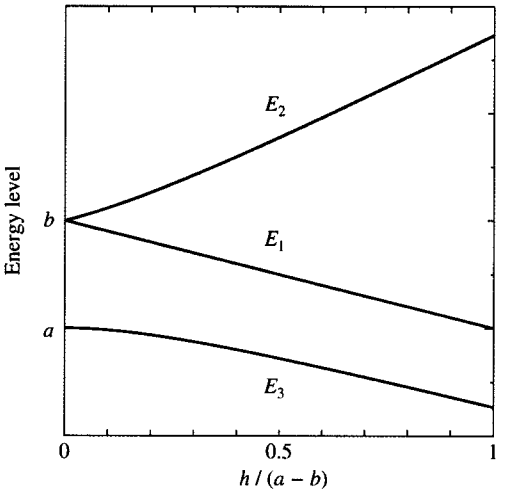

Fig. 2.5 Energy levels of three ground torsional states depending on the magnitude of tunneling (h). a and b denote the energy levels of pocket states when the quantum tunneling is neglected; b is doubly degenerated and a is not degenerated.

2.4.4 Application of the Pocket State Theory

The pocket state theory has been used for the analysis of partially deuterated methane in solid [14,15] as well as in the monolayer system adsorbed on the surface of graphite [16-18]. Since methane is a molecule with tetrahedral symmetry, the rotational motion is three-dimensional. The solution of Schrödinger equation for such a system is very complicated in mathematical formula. In this respect, the simple formula of the pocket state theory is advantageous for such systems.

For the lowest temperature phase of partially deuterated methanes called "phase III", the tunneling states were clearly observed by inelastic neutron scattering (INS) [15] and heat capacity measurements [14]. These two experimental data were correlated to each other by applying the pocket state theory taking into account the differences in energy for different molecular orientations under anisotropic field [15].

For the monolayer system, INS and heat capacity data of CH_3D on graphite were explained by the pocket state model assuming two states with different energies; one with the deuteron pointing away from the surface (D-up) and the other with the deuteron pointing toward the surface (D-down) [16].

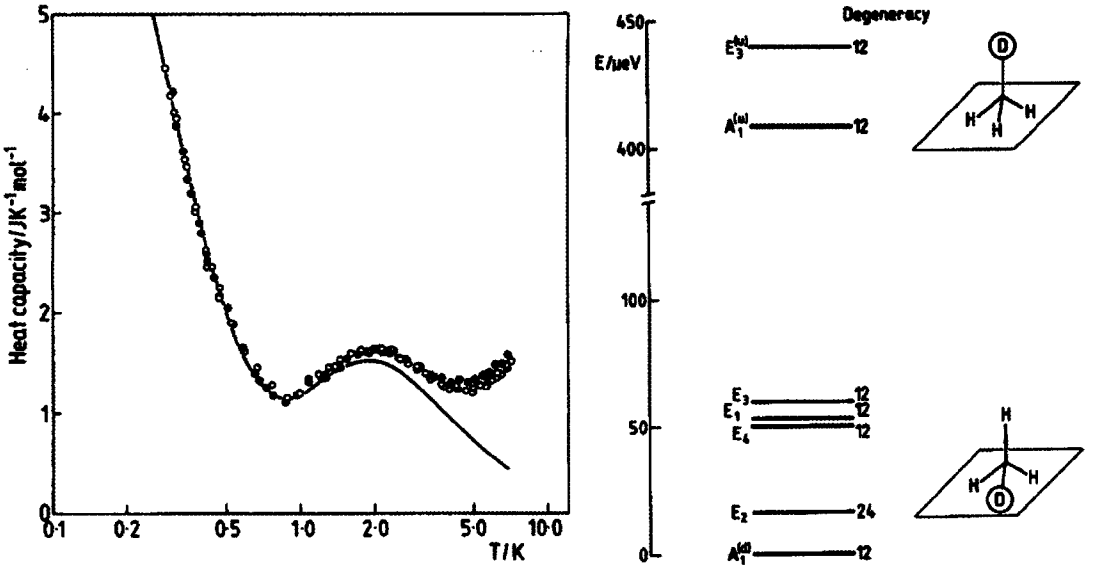

Fig. 2.6 (Left) Heat capacities of CH_3D/graphite at two different coverages. The solid curve is calculated from the energy scheme. The discrepancy between them comes from the 2D lattice vibrations [16]. (Right) Energy scheme for CH_3D/graphite [16].

Although the pocket states model is quite useful for the analyses of the ground torsional states especially in the solid phase, it does not tell anything about the origin of the energy difference between the pocket states, that is, the difference in the torsional zero point energy for different orientations. In order to explain this, some other model is needed.

In the study of solid methane, Lushington *et al.* [15] introduced a coefficient R as a measure of molecular anisotropy to calculate the energy difference between the four orientations. Using the quantity R as an adjustable parameter, they finally obtained a good agreement in the theoretical heat capacity curve with the experimental results for CH_3D in the phase III. In the methane monolayer system, Maki [17] estimated the energy difference of two states for CH_3D, D-up and D-down, from the phonon spectra of CH_4 physisorbed on Papyex, which was however 6 ~ 8 times smaller than that obtained from the heat capacity data.

To the best of my knowledge, no theory adequately predicts those energy differences, which is the main subject later in this thesis.

2.5 Rotational Entropies for the Partially Deuterated Methyl Groups

Since $-CH_3$ and $-CD_3$ are three-fold symmetric, rotation by 120° gives identical state. $-CH_2D$ and $-CHD_2$, on the other hand, are non-symmetric, so the state after 120° rotation is different. This leads to the difference in rotational entropy by R ln 3 between two systems, because $-CH_2D$ and $-CHD_2$ have three time more number of possible states than $-CH_3$ or $-CD_3$.

In the regime of classical statistics, the excess entropy is explained by using the rotational symmetry number σ. The rotational partition function, z_{rot}, in the gas phase is given by

$$z_{rot} = \frac{8\pi^2 IkT}{\sigma h^2}, \tag{2.25}$$

where h is the Plank constant, I is the moment of inertia of the rotor and σ is the rotational symmetry number. Then the rotational entropy is given by

$$S = -\left(\frac{\partial A}{\partial T}\right) = \frac{\partial kT \ln z}{\partial T} = k \ln z . \tag{2.26}$$

The first equation derives from the thermodynamic relation and the second one derives from the relation between z and A, the Helmholtz energy. Then the difference in rotational entropy due to the different symmetry number, say σ_1 and σ_2 for example, can be written as

$$\Delta S_{rot,m} = S_{rot,m}(\sigma_1) - S_{rot,m}(\sigma_2) = R \ln\left(\frac{\sigma_2}{\sigma_1}\right). \tag{2.27}$$

Since the symmetry number of $-CH_2D$ and $-CHD_2$ is $\sigma = 1$, while that of $-CH_3$ and $-CD_3$ is $\sigma = 3$, the

entropy difference amounts to R ln 3. The classical statistics describes the high temperature limit. In the limit of low temperature, according to the third law of thermodynamics, the entropy difference gets close to zero at 0 K, so that the excess entropy of R ln 3 has to be removed from the system with decreasing temperature down to 0 K. It is quite interesting to know when (in which temperature) and how (in which process) the excess contribution is removed.

The symmetry number in the classical statistics corresponds to the symmetry restriction of the wave functions in the quantum statistical mechanics. In the case of methyl groups, the symmetric rotor, $-CH_3$ or $-CD_3$ with $\sigma = 3$, takes only one third of the states of the asymmetric rotor like $-CH_2D$ or $-CHD_2$. This is still true at low temperature in the regime of quantum statistics where the prohibition law works on the rotational excitation. In the energy scheme shown in Fig. 2.1, $A \leftrightarrow A$ and $E \leftrightarrow E$ transitions are allowed while that of $A \leftrightarrow E$ is forbidden by the quantum symmetry restriction, if only the rotational states are accounted. For $-CH_2D$ or $-CHD_2$, the $A \leftrightarrow E$ transition corresponds to the transition between $0_0 \leftrightarrow 0_{\pm}$, which is observable due to the breaking of symmetry. If the nuclear spin states are taken into account, the $A \leftrightarrow E$ transition for $-CH_3$ is possible, although it takes extremely long time due to the nuclear spin conversion as described before.

2.6 References for Chapter 2

[1] W. Press, *Single Particle Rotations in Molecular Solids*, Vol. 92. (Springer, Berlin, 1981)

[2] D.G. Lister, J.N. Macdonald and N.L. Owen, *Internal Rotation and Inversion* (Academic Press Inc., London, 1978).

[3] L.S. Bartell, E.A. Roth, C.D. Hollowell, K. Kuchitsu and J.E. Young Jr., *J. Chem. Phys.* **42** (1965) 2683.

[4] A. Detket, H. Zimmermann, *J. Chem. Phys.* **108** (1998) 5845.

[5] C.R. Quade and C.C. Lin, *J. Chem. Phys.* **38** (1963) 540.

[6] J.D. Lewis, T.B. Malloy Jr., T.H. Chao and J. Laane, *J. Mol. Struct.* **12** (1972) 427.

[7] E.B. Wilson Jr. and J.B. Howard, *J. Chem. Phys.* **4** (1936) 260.

[8] R.W. Kilb, C.C. Lin and E.B. Wison Jr., *J. Chem. Phys.* **26** (1957) 1695.

[9] J.V. Knopp and C.R. Quade, *J. Chem. Phys.* **48** (1968) 3317.

[10] P.H. Turner, A.P. Cox and J.A. Hardy, *J. Chem. Soc. Faraday Trans. 2,* **77** (1981) 1217.

[11] D. Schwoch and H.D. Rudolph, *J. Mol. Spectrosc.* **57** (1975) 47.

[12] A. Huller, *Phys. Rev. B*, **16** (1977) 1844.

[13] A. Huller and J. Raich, *J. Chem. Phys.* **71** (1979) 3851.

[14] J.H. Colwell, *J. Chem. Phys.*, **51** (1969) 3820.

[15] K.J. Lushington, K. Maki, J.A. Morrison, A. Heidemann and W. Press, *J. Chem. Phys.* **75**

(1981) 4010.

[16] P.C. Ball, A. Inaba, J.A. Morrison, M.V. Smalley and R.K. Thomas, *J. Chem. Phys.* **15** (1990) 1372.

[17] K. Maki, *J. Chem. Phys.* **74** (1981) 2049.

[18] A. Inaba, J. Skarbek, J.R. Lu, R.K. Thomas, C.J. Carlile and D.S. Sivia, *J. Chem. Phys.* **103** (1995) 1627.

Chapter 3

Experimental Techniques and Data Analyses

3.1 Heat Capacity Measurement

3.1.1 Principle of Adiabatic Calorimetry

Since a pioneering work by Eucken and Nernst in the early 20th century [1], the adiabatic calorimetry has been considered to be the most appropriate method to obtain accurate data of heat capacity.

The heat capacity at constant pressure C_p of a system is defined by

$$C_p = \left(\frac{\partial H}{\partial T}\right)_p . \tag{3.1}$$

This quantity can be measured experimentally as

$$\left(\frac{\partial H}{\partial T}\right)_p = \frac{\Delta Q}{\Delta T}, \tag{3.2}$$

where ΔQ is the energy supplied and ΔT is the temperature increment.

In adiabatic calorimetry, the system (sample and sample cell) is kept at an adiabatic condition and the heat capacity is obtained directly from ΔQ and ΔT. Good adiabatic condition is achieved by evacuating the space outside the system and keeping the temperature of the surrounding (radiation) shields at the same temperature to that of the system. When ΔQ is supplied electrically, it is calculated with

$$\Delta Q = I \cdot V \cdot \Delta t , \tag{3.3}$$

where I is the current and V is the voltage across the heater and Δt is the heating time. ΔT is determined by measuring the temperature of the system before (T_i) and after (T_f) the heating. Fig. 3.1 schematically shows the temperature variation of the system as well as the procedure to determine the T_i and T_f. Before the heating, the sample temperature slightly varies with time, which is due to the imperfect adiabatic condition. The temperature variation can be approximated by a linear function. The slope of the function is called "drift rate", which is characteristic to the calorimeter and

the temperature range to measure. Immediately after the heating, the sample temperature varies considerably with time, which is due to the thermal equilibration inside the system. After a period of time, the drift rate comes back to normal. T_i and T_f are obtained by extrapolating the temperature drift to the mid-point of the heating period. If some other factor influences the temperature drift, such as exothermic stabilization of the sample, the extrapolation in Fig. 3.1 does not provide the equilibrium heat capacity. In this respect, temperature dependence of the drift rate is very important to detect the non-equilibrium phenomena.

Sample heat capacity is obtained by subtracting the contribution of the sample cell from the total heat capacity of the system. The heat capacity of the cell is measured separately. The dead space of the sample cell is usually filled with one-atmospheric pressure of helium gas to promote equilibration. The contribution of helium to the total heat capacity is estimated by assuming that $C_{V,m} = (3/2)\,R$.

The advantage of adiabatic calorimetry is that it provides quite accurate heat capacity data. It is also beneficial that various types of samples (liquid, powdered sample, single crystals, etc.) can be measured by adiabatic calorimetry. Moreover, this method is useful to measure the long enthalpy relaxation associated with the glass transition. The disadvantage of this technique is that it requires large amount of samples (~ 1 g).

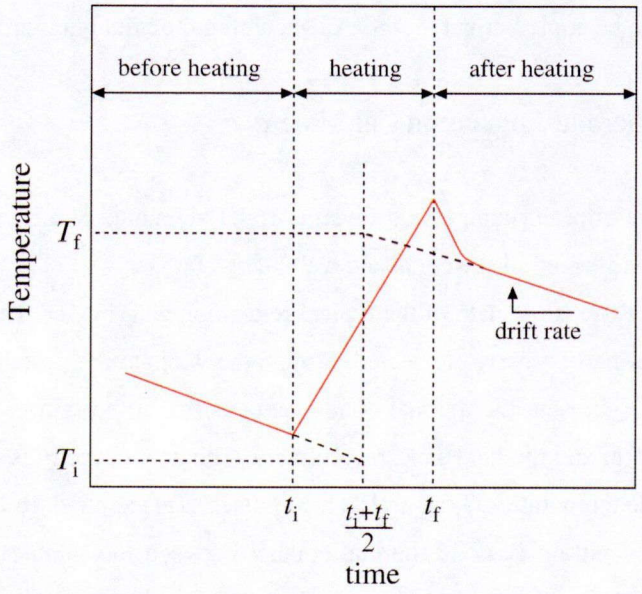

Fig. 3.1 The procedure to determine the temperatures before (T_i) and after (T_f) heating in adiabatic calorimetry

3.1.2 Adiabatic Calorimeter

The adiabatic calorimeter used in this study was designed in the laboratory [2]. The cell is directly suspended by a string from the top of the cryostat, which also works as a mechanical thermal switch. The sample cell is surrounded by two concentric adiabatic shields. The inner shield is suspended from the outer shield and the outer shield is suspended from the cryo-tank. On cooling the sample, these two adiabatic shields are pulled up by the string together with the cell until they attach to the liquid helium cryo-tank. The thermal switch makes it convenient to measure the heat capacity around 5 K.

During the measurements, the sample cell and the adiabatic shields are set back to the original suspended position. The temperature of the inner adiabatic shields is controlled to be the same to that of the sample cell. The temperature of the top part of the inner shield is regulated against the surface temperature of the cell. The bottom part of the inner shield is controlled against the top of the inner shield. Similar temperature controllers regulate the temperature of the thermal anchor as well as the top part of the outer shield against the top of inner shield. The outer shield is kept at temperatures slightly below that of the inner shield.

The cell is made of copper and is gold-plated. The internal volume of the cell is 2.77 cm^3. The temperature of the sample is measured with a rhodium-iron alloy resistance thermometer attached to the top of the sample cell. The working temperature range of this calorimeter is between 5 K and 400 K. If needed, it can be cooled down to 3 K by evacuating the liquid helium in the cryo-tank.

3.1.3 Principle of Thermal Relaxation Calorimetry

The thermal relaxation calorimetry was invented by Bachmann *et al.* in 1972 [3]. Later on, modifications and related techniques were also developed [4-6].

Fig. 3.2 presents the heat-flow path of the typical relaxation calorimeter. The sample is placed on the platform that is thermally weakly connected through the wires to the heat sink at a temperature $T = T_b$. Here, K_g and K_w represent the thermal conductance between the sample and the platform and that between the platform and the heat sink, respectively. The heat capacity is derived from the time evolution of the sample temperature $T_s(t)$, after a heat pulse $P(t)$ is applied. In the simplest analytical model, which premises extremely good thermal contact between the sample and the platform, the platform temperature $T_p(t)$ is always identical with $T_s(t)$. The heat balance equation is thus written as

$$C_{\text{total}} \frac{dT_p}{dt} = -K_w \left[T_p(t) - T_b \right] + P(t), \tag{3.4}$$

where C_{total} is the total heat capacity of the sample and the platform together. If $P(t)$ is constant at P_0 during heating (the dotted line in Fig. 3.3), $T_p(t)$ is given by a simple exponential function (the solid

curve in Fig. 3.3) with a characteristic time constant, τ, which is equal to C_{total}/K_w. The same is true for the cooling curve obtained when $P(t) = 0$. If the platform heat capacity $C_{platform}$ is known, the sample heat capacity C_{sample} is derived simply from τ and K_w.

If, however, the thermal contact between the sample and the platform is not perfect, $T_p(t)$ has to be described by equations involving two different time constants, τ_1 and τ_2. The introduction of the second τ was actually the key to further development of relaxation calorimetry [4-6]. K_g is now directly involved in the following heat balance equations to accommodate the second τ.

$$C_{platform}\frac{dT_p}{dt} = -K_w\left[T_p(t) - T_b\right] + K_g\left[T_s(t) - T_p(t)\right] + P(t), \tag{3.5}$$

$$C_{sample}\frac{dT_s}{dt} = -K_g\left[T_s(t) - T_p(t)\right]. \tag{3.6}$$

The relaxation curve can then be expressed as

$$T_p(t) = T_b + A\exp(-t/\tau_1) + B\exp(-t/\tau_2), \tag{3.7}$$

where A and B are the coefficients. The time constant τ_2, which is supposed to be shorter than τ_1, characterizes the thermal relaxation between the sample and the platform. In this case, if $C_{platform}$ and K_w are given, C_{sample} is calculated from the values of τ_1 and τ_2. It should be noted here that it is not necessary to monitor the sample temperature directly and that we do not need the K_g value explicitly, either.

The advantage of the relaxation method is that it provides relatively accurate C_p data for small amount of sample quantity (~ 1 mg). Since the sample size is small, it is also possible to measure the heat capacity under extreme physical conditions such as in a high magnetic field. One disadvantage of relaxation calorimetry is that the data of molecular solids at high temperatures are not reliable because the thermal conductivity of the sample itself becomes poor at high temperatures. Another disadvantage is that it is difficult to determine accurate C_p values at first-order phase transitions by relaxation calorimetry. Recently we demonstrated scanning method to solve this problem [7], which is not described in this thesis. Another disadvantage of this method is that the liquid sample cannot be directly placed on the platform under high vacuum. This problem was also solved by making a tiny cell for the liquid sample, which will be described in detail in Section 3.1.5.

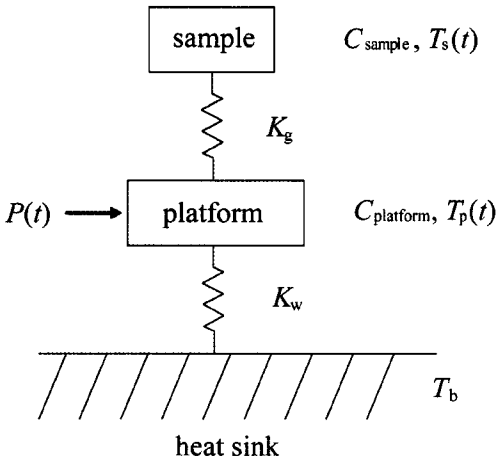

Fig. 3.2 The heat-flow diagram for a standard relaxation calorimeter. C_{sample} and $C_{platform}$ are the heat capacities of the sample and the platform, respectively. $T_s(t)$ and $T_p(t)$ are the temperatures of the sample and the platform, respectively. K_w and K_g are the thermal conductance of the wires and grease including the contribution of the sample itself. T_b is the temperature of the thermal bath and $P(t)$ is the power supplied by the heater.

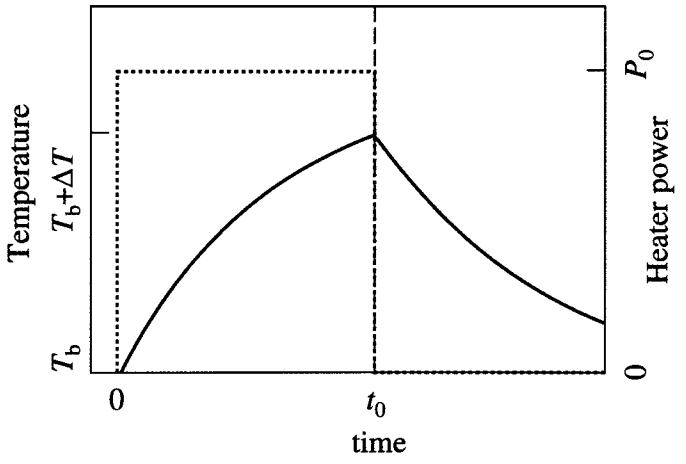

Fig. 3.3 Conventional method in a typical relaxation calorimetry to determine the heat capacity. A heat pulse with a constant power P_0 is applied to the sample system (dotted line), and the sample temperature changes accordingly (solid curve). The resulting relaxation curves can be fitted with a simple exponential function, from which the heat capacity is calculated.

3.1.4 PPMS Relaxation Calorimeter

The relaxation calorimeter used in this study was a fully automated commercial calorimeter named Physical Property Measurement System (PPMS) by Quantum Design [8]. This instrument is now widely used throughout the world, and the data obtained by this system were carefully assessed [9-11]. The construction of the PPMS is as follows.

The sample platform consists of a 3 × 3 mm^2 sapphire plate. At the back, both a thin film RuO heater and a Cernox^{TM} thermometer (Lakeshore Cryotronics) are attached. Their lead wires provide weak thermal link to the heat sink with a conductance of K_w. The thermal contact between the sample and the platform is achieved with grease (normally with Apiezon^{TM} N). The sample chamber is evacuated by a turbo-molecular pump to eliminate other conduction paths. The operational temperature ranges from 1.9 K to 400 K for the standard setup (called "normal system") and it can be extended to lower temperatures with either the helium-3 or the dilution refrigerator options. In this study, the helium-3 system was used to obtain the data down to 0.35 K.

The PPMS software analyzes two successive relaxation curves; the one for heating with a constant power $P(t) = P_0$ followed by the other for cooling with $P(t) = 0$. With the default setting, P_0 is automatically chosen in such a way that the temperature is raised by 2% of the absolute value in a time of $\tau/2$ (or $\tau_1/2$). We can also specify the temperature rise ΔT in much longer time. But, P_0 itself cannot be specified, and the maximum time for collecting data is limited to 1000 s.

Since $C_{platform}$ (often called "addenda" heat capacity) includes the contribution from the grease, it has to be measured beforehand. The PPMS software can apply two models for analysis of the relaxation curve, either *single-tau model* or *two-tau model*. The former, which is normally applied to the "addenda" measurement, uses the differential equation of Eq. (3.4) for both the heating and cooling processes. The analytical solutions are given by

$$T_p(t) = \frac{P_0\tau(1-e^{-t/\tau})}{C_{total}} + T_b \qquad \text{(for heating)} \qquad (3.8a)$$

$$T_p(t) = \frac{P_0\tau(1-e^{-t_0/\tau})}{C_{total}} \times e^{-(t-t_0)/\tau} + T_b \qquad \text{(for cooling)} \qquad (3.8b)$$

where t_0 is the time when the heat pulse is off. As mentioned above, the τ is given by C_{total}/K_w. The PPMS calculates C_{total}, K_w and T_b by a nonlinear least-squared fitting routine. For the sample measurement, the *two-tau model* was applied involving the second time constant τ_2. The analytical solutions of Eqs. (4.4) and (4.5) are

$$T_p(t) = \frac{P_0}{K_w} + \frac{P_0}{2\beta K_w}\left(\frac{e^{-t/\tau_2}}{\tau_1} - \frac{e^{-t/\tau_1}}{\tau_2}\right) + T_b \qquad \text{(for heating)} \qquad (3.9a)$$

$$T_{\mathrm{p}}(t)=\frac{P_0}{4\beta K_{\mathrm{w}}}\left(\frac{\mathrm{e}^{-(t-t_0)/\tau_1}}{\tau_2}-\frac{\mathrm{e}^{-(t-t_0)/\tau_2}}{\tau_1}\right)\left[2-\frac{1}{\beta}\left(\frac{\mathrm{e}^{-t_0/\tau_1}}{\tau_2}-\frac{\mathrm{e}^{-t_0/\tau_2}}{\tau_1}\right)\right]+T_{\mathrm{b}}$$

(for cooling) (3.9b)

where

$$\tau_1=\frac{1}{\alpha-\beta} \quad \text{and} \quad \tau_2=\frac{1}{\alpha+\beta}, \tag{3.10a, 3.10b}$$

$$\alpha=\frac{K_{\mathrm{w}}}{2C_{\mathrm{platform}}}+\frac{K_{\mathrm{g}}}{2C_{\mathrm{platform}}}+\frac{K_{\mathrm{g}}}{2C_{\mathrm{sample}}}, \tag{3.11}$$

$$\beta=\frac{\sqrt{\left(C_{\mathrm{platform}}K_{\mathrm{g}}+C_{\mathrm{sample}}K_{\mathrm{g}}+C_{\mathrm{sample}}K_{\mathrm{w}}\right)^2-4C_{\mathrm{platform}}C_{\mathrm{sample}}K_{\mathrm{w}}K_{\mathrm{g}}}}{2C_{\mathrm{platform}}C_{\mathrm{sample}}}. \tag{3.12}$$

Since C_{platform} is obtained beforehand, there are four parameters to be determined: K_{w}, K_{g}, T_{b} and C_{sample}. They are all calculated again by a non-linear least squared fitting routine. As long as Eq. (3.7) faithfully reproduces the measured relaxation curve, the software can determine the C_{sample} value accurately without knowing any explicit values of K_{w}, K_{g} and T_{b}.

3.1.5 Heat Capacity Measurements of Liquid Samples on PPMS

PPMS is basically designed only for solid samples. For liquid samples, there are two problems; one is that the accurate value of the sample mass cannot be known if the sample is directly placed on the platform, and the other one is that liquid samples can be evaporated before the measurement starts. Several trials were made to solve these problems by developing small containers for liquid samples, and finally three types of containers were used depending on the sample volatility.

Case 1: Low-volatile Sample

When the sample is low volatile, it is not necessary to seal off the container. The sample cell is made of copper tube; 1.0 mm in outer diameter, 3 mm long and 0.1 mm thick. The mass is approximately 9 mg. The sampling procedure is comprised of a few steps; (1) flatten one side face of the tube (to give better thermal conduction to the platform), (2) measure the mass of the cell, (3) put the liquid sample (c.a. 1 μL) into the cell with a syringe, (4) squash the both ends of the cell, and (5) measure the total mass. The heat capacity of the cell is calculated from the mass referring the molar heat capacity of the copper measured beforehand. Copper was chosen as the cell material because: (1) copper is a standard material for the low-temperature heat capacity, (2) a thin tube of copper is

commercially available, and (3) it is easy to deform the copper tube. Fig. 3.4 shows a picture of the copper cell sitting on the sample platform of PPMS puck. Apiezon^{TM} N grease is used as a heat transmitting medium. Since the squashed two ends of the tube is not vacuum tight, the sample has to be cooled down first to crystallize (or vitrify) under ambient pressure of helium gas, in order to avoid the sample evaporation.

Fig. 3.5 shows the low temperature heat capacities of liquid crystalline material 8*OCB [(*S*)-4-(1-methylheptyloxy)-4'-cyanobiphenyl] for three phases [12]. The data obtained by adiabatic calorimetry is also shown. The agreement between the two data sets is excellent. Fig. 3.6 shows the contribution from the sample (glass of liquid for 8*OCB, in this case), the addenda and the cell to the total heat capacity. The sample contribution above 2 K amounts more than 30%, whereas, below 2 K, the contribution decreases dramatically because of the electronic heat capacity of copper of the cell. Actually, this effect is reflected in the heat capacity obtained (Fig. 3.4), where the data scatter significantly at low temperature.

Case 2: Volatile Sample

When the sample is volatile, the cell described above cannot prevent the sample from evaporation even under the ambient pressure during the cooling. In such a case, the ends of the copper tube are pinched off to be sealed by dull-edged nipper. The sealing is tight enough to keep large part of the sample in the cell under one atmospheric pressure, although it is not fully-sealed. Since small amount of evaporation of the sample is unavoidable, the total mass is usually not measured. Alternatively, the background heat capacity is measured every time after the sample measurement. The background is obtained by evaporating the sample under high vacuum at room temperature. Since the amount of sample in the cell can not be measured in this procedure, it has to be determined by referring the sample heat capacity obtained from adiabatic calorimetry.

Case 3: Highly Volatile Sample

When the vapor pressure of the sample is extremely high, the pinched-off ends of the cell cannot keep the sample in the cell even under the ambient pressure. In this case, the aluminum pan is used as a sample container. In this study, the Volatile Aluminum Sample Pan (No. 0219-0062) produced by Perkin Elmer for the differential scanning calorimetry (DSC) was used. The inner volume of the pan is 20 μL and the mass is approximately 24 mg. The pan can be hermetically sealed which withstands the pressure of more than three atmospheres. Since the sealing of the pan is perfect, the mass of the sample can be easily measured. One problem of this container is that aluminum undergoes a superconducting transition at 1.2 K. Since the heat capacity of aluminum in the

superconducting phase (below 1.2 K) easily varies with mechanical deformation, the heat capacity of the empty pan has to be measured every time after the sample measurement. The aluminum pan is emptied out by making a hole in it and then exposing it under high vacuum. As a matter of fact, however, even by this hole, the heat capacity of the aluminum pan can slightly be changed. Another problem of the aluminum pan is that the sample amount is significantly large. In relaxation calorimetry, the time constant of the relaxation is proportional to the sample heat capacity so as to the sample amount. Therefore when the sample heat capacity is very large at low temperature, the measurement time becomes extremely long. It sometimes becomes longer than 1000 seconds which is the maximum limit of the measurement time of PPMS. Considering these problems, the aluminum pan was used as a last option.

In this study, the second option (copper cell with relatively tight sealing) was applied for all the liquid samples except for methyl iodide. Since methyl iodide has extremely high vapor pressure, the third option was applied.

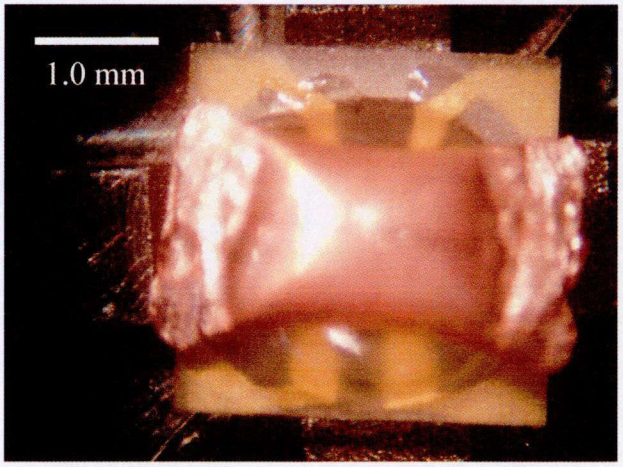

Fig. 3.4 A cell for liquid samples sitting on the sample platform of PPMS puck. Apiezon^{TM}N grease is used as a heat transmitting medium between the cell and the platform. The cell is made of copper with mass of about 9 mg. It contains about 1 μL of liquid sample.

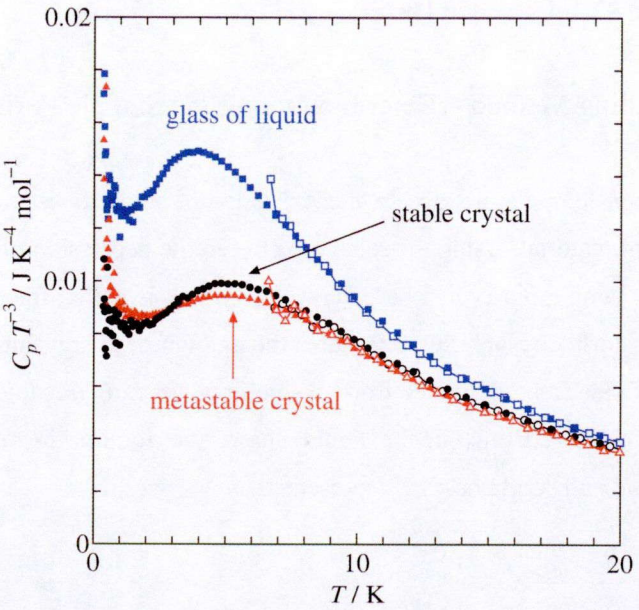

Fig. 3.5 C_p/T^3 plot for the three phases of 8*OCB as an example to show the overall performance of the liquid sample cell [13]. The filled-marks are the data obtained by PPMS, using the liquid sample cell. The open-marks are the data obtained by an adiabatic calorimeter [12]. Both data sets agree very well for each of the phases.

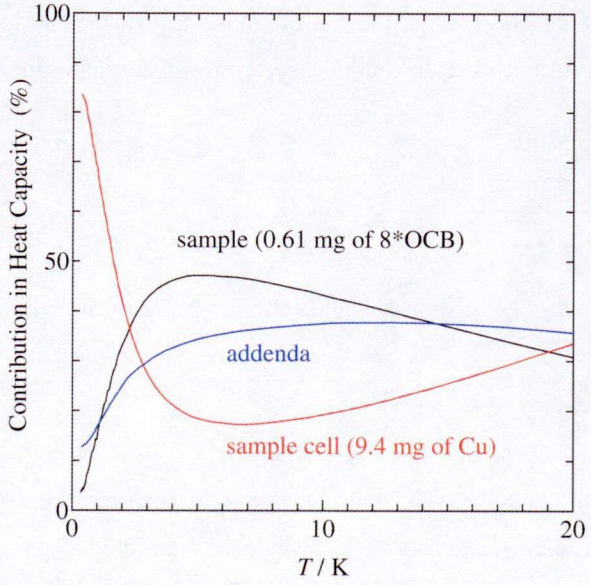

Fig. 3.6 The contribution from the sample (glass of liquid for 8*OCB), the addenda and the liquid sample cell to the total heat capacity. The sample contribution above 2 K is more than 30%. Below 2 K, on the other hand, the contribution of the cell becomes dominant because of the large electronic heat capacity of copper, and the sample contribution falls steeply down to about 5% at the lowest temperature (0.35 K).

3.2 Analysis for the Calorimetric Data

3.2.1 Fractional Melting Method – Determination of the Sample Purity –

Depression of fusion temperature due to the existence of impurity is one of the well known colligative properties of material. Using the relation between the depression of melting point and the fraction of fusion, the sample purity can be determined, which is called fractional melting method [14]. Since adiabatic calorimetry precisely measures the amount of energy supplied into the system, it is possible to quantify the fraction melted from the melting curve of enthalpy.

If the impurity is dissolved only in the liquid phase, the equilibrium temperature T_{eq} in the coexisting state of liquid and solid phases is represented as

$$T_{eq} = T_{fus} - \frac{R \cdot T_{fus}^{\ 2}}{\Delta_{fus} H_m} \cdot x \cdot \frac{1}{f}, \tag{3.13}$$

where T_{fus} is the fusion temperature of the pure material, $\Delta_{fus}H_m$ is the molar enthalpy of fusion, R is the gas constant and x is the mole fraction of the impurity. f is the fraction melted which can be calculated from the energy supplied. From the slope in the plot of T_{eq} against f^{-1} ($1/f$ plot), x can be determined.

If the impurity is partially dissolvable in the solid phase, Eq. (3.1) is no longer applicable. The $1/f$ plot then deviates from a straight line. In such a case, a modified equation may be used to fit the plot [15],

$$T_{eq} = T_{fus} - \frac{R \cdot T_{fus}^{\ 2}}{\Delta_{fus} H_m} \cdot \frac{x}{\alpha + f}, \tag{3.14}$$

where α is defined as $\alpha = K / (1 - K)$ and K is the solubility ratio of the impurities in the two phases.

3.2.2 Lattice Heat Capacity

On analyzing the heat capacity data, it is necessary to separate the contribution of molecular motions of interest. In general, heat capacity of a molecular solid consists of several modes such as the lattice modes, the intramolecular modes or the electronic and magnetic modes. The last two contributions are not considered here, since the compounds studied in this work are neither electric conductive nor magnetic materials. For the first two contributions, two models are useful; Einstein model and Debye model.

The Einstein model assumes that the frequency ω_E of the motion of interest is constant and equal for all molecules. The Einstein heat capacity is given by,

$$C_V = Nk_B\left(\frac{\theta_E}{T}\right)\frac{\exp(\theta_E/T)}{\{\exp(\theta_E/T)-1\}^2}, \tag{3.15}$$

where θ_E is the Einstein temperature defined by

$$\frac{\theta_E}{T} = \frac{\hbar\omega_E}{k_B T}. \tag{3.16}$$

This model can be applied to the intramolecular motions within the harmonic approximation. It can also be applied to the optical modes of lattice vibration, in which the frequency is independent of the wave vector.

For the acoustic modes of lattice vibration, the Einstein model cannot be applied because the frequency has density distribution $G(\omega)$. In the Debye approximation, $G(\omega)$ is assumed to be proportional to ω^2 below the cut off frequency ω_D. The distribution above ω_D is zero; $G(\omega) = 0$. The formula of Debye heat capacity is given by

$$C_V = 9Nk_B\left(\frac{T}{\theta_D}\right)^3\int_0^{\theta_D/T}\frac{x^4e^x}{\left(e^x-1\right)^2}dx, \tag{3.17}$$

where θ_D is Debye temperature, which is related to the cut off frequency ω_D as

$$\frac{\theta_D}{T} = \frac{\hbar\omega_D}{k_B T}. \tag{3.18}$$

ω_D is defined by

$$\omega_D^3 = \frac{6\pi^2\upsilon^3 N}{V}, \tag{3.19}$$

where υ is the sound velocity, V is the volume and N is the total number of acoustic phonon modes. All properties are therefore determined by the sound velocity υ, which comes from the basic assumption of the Debye model that all the dispersion relation of phonons can be replaced by a single linear acoustic branch,

$$\omega = \upsilon K, \tag{3.20}$$

where K is a wave vector.

3.2.3 Deuteration Effect on the Lattice Heat Capacity

Using Einstein and Debye models, it is possible to predict the mass effect on the lattice heat capacities. For the intramolecular vibrations, the harmonic approximation gives the frequency ω as

$$\omega = \frac{1}{2\pi}\sqrt{\frac{f}{m}}, \tag{3.21}$$

where m is the reduced mass of the oscillator and f is the force constant. If f is independent of m, the

mass effect on the Einstein heat capacity can easily be derived through the variation of frequencies ω with the reduced mass m.

For the acoustic vibrations, the variation of atomic or molecular mass is included in the sound velocity υ. In the single-atomic one-dimensional crystal, the dispersion curve of the vibrational modes of long wavelength, i.e. small value of K, can be described as

$$\omega = aK\sqrt{\frac{f}{m}}, \tag{3.22}$$

where f is force constant between atoms, a is lattice constant and m is mass of atoms. If the force constant and the lattice constant does not vary with mass change,

$$m \propto \upsilon^2 \propto \omega_D^2 \propto \theta_D^2 . \tag{3.23}$$

By applying this relation to the lattice dynamics of molecular crystals, the mass effect on the Debye heat capacities can be derived.

Since the deuteration effects on the lattice heat capacity are mainly due to the mass effect, the two models are useful to predict the lattice heat capacities of deuterated materials from those of the non-deuterated analogs. This is because, in these models, the mass contributions in heat capacities can be reduced to the factors of θ_E and θ_D. If θ_E and θ_D vary with mass in a similar way, like Eq. (3.21) and Eq. (3.22), the heat capacity of the deuterated compounds can be derived by scaling the values of non-deuterated compounds against temperature with single reduction factor. This is the simplest case. Usually θ_E and θ_D show different mass dependence, so that the two contributions (the Einstein and Debye heat capacities) have to be treated separately. The Einstein heat capacity of the deuterated material can be calculated using Eq. (3.15), (3.16) and (3.21), when all the frequencies of the intramolecular vibrations are known and when the types of motion do not differ with deuteration. When the type of motion significantly vary with deuteration, the Eq. (3.21) is no longer useful. Then it is necessary to determine the normal modes and their frequencies of the deuterated material, which are usually done either by the quantum mechanical computation or by spectroscopic measurement. The former method is useful when there is no experimental data at hand, while the latter one gives more reliable values of frequency. Once the Einstein heat capacities are derived, the Debye contribution can be obtained by subtracting the Einstein contributions from the total heat capacity. The Debye heat capacity of the deuterated compound is then obtained by scaling the data of non-deuterated compound against temperature.

3.2.4 Schottky Heat Capacity

In the Einstein model, the energy levels to be occupied are assumed to exist up to infinite levels. This is why the Einstein heat capacity approaches to constant value of R at high temperature. If the number of energy levels is finite, heat capacity should approach to zero at high temperature. This

problem was considered by Schottky in 1922 [16]. If the system has an energy scheme of m levels separated from the ground state by energies ε_1, ε_2, ..., ε_m with degeneracy g_1, g_2, ..., g_m, then the probability of a particle occupying the rth level is given by

$$P_r = \frac{g_r \exp(-\varepsilon_r / k_B T)}{\sum_{r=1}^{m} g_r \exp(-\varepsilon_r / k_B T)}, \tag{3.24}$$

where the Boltzmann distribution law is assumed. With N independent particles in the system, the mean energy at temperature T is,

$$U = \frac{N\sum_{r=1}^{m} \varepsilon_r g_r \exp(-\varepsilon_r / k_B T)}{\sum_{r=1}^{m} g_r \exp(-\varepsilon_r / k_B T)}. \tag{3.25}$$

The heat capacity can be obtained by calculating dU/dT, which is called Schottky heat capacity. For a two-level system spaced by ε_1, for example, the Schottky heat capacity is given by,

$$C_{sch} = \frac{N\varepsilon_1^2}{k_B T^2} \frac{g_0}{g_1} \frac{\exp(\varepsilon_1 / k_B T)}{[1 + (g_0 / g_1)\exp(\varepsilon_1 / k_B T)]^2}. \tag{3.26}$$

At high temperature limit ($\varepsilon_1/k_BT << 1$) C_{sch} is proportional to T^{-2}, which is true for the multi-level system.

3.3 Infrared Spectroscopy

3.3.1 Principle of Infrared Absorption

Infrared (IR) absorption spectroscopy is one of the most common spectroscopic techniques used in chemistry. It measures the absorption of the IR beam by a sample, which is characteristic to the molecular motions.

When absorption occurs from the sample state m to n, the rate of population (N_n) change is given by

$$\frac{dN_n}{dt} = N_m B_{mn} \rho(\nu), \tag{3.27}$$

where B_{mn} is the Einstein coefficient for the photo absorption and $\rho(\nu)$ is the radiation density given by

$$\rho(\nu) = \frac{8\pi h \nu^3}{c^3 \left(e^{h\nu / k_B T} - 1\right)}, \tag{3.28}$$

where ν is the frequency of the radiation and c is the velocity of light. The Einstein coefficient is related to the transition probability $|\mathbf{R}^{nm}|^2$ by

$$B_{mn} = \frac{8\pi^3}{(4\pi\varepsilon_0)3h^2}\left|\mathbf{R}^{nm}\right|^2, \tag{3.29}$$

where ε_0 is the vacuum permittivity. $\mathbf{R}^{nm}$ is the transition moment which is given by

$$\mathbf{R}^{nm} = \int \psi_n^* \boldsymbol{\mu} \psi_m d\tau, \tag{3.30}$$

for interaction with the electric component of the radiation. The quantity $\boldsymbol{\mu}$ is the dielectric dipole moment operator

$$\boldsymbol{\mu} = \sum_i q_i \mathbf{r}_i, \tag{3.31}$$

where q_i and $\mathbf{r}_i$ are the charge and position vector of the ith particle, respectively. The transition moment $\mathbf{R}^{nm}$ is thus thought as the oscillating electric dipole moment due to the transition. In case of excitation from the ground state to the first excited state, B_{nm} is related to the molar absorption coefficient $\varepsilon(\nu)$ by

$$\int_{\nu_1}^{\nu_2} \varepsilon(\nu) \mathrm{d}\nu = \frac{N_A h \nu B_{nm}}{c \ln 10}. \tag{3.32}$$

$\varepsilon(\nu)$ is experimentally obtained through the absorbance A, which is defined by the common logarithm of the ratio of incident radiation power I_0 to the one transmitted by the sample I.

When the sample is a solid film, absorption coefficient α and the thickness of the film d are usually used instead of $\varepsilon(\nu)$, C and l, so that A is given by

$$A = \alpha(\nu) d. \tag{3.33}$$

For IR absorption measurement, the transition moment in Eq. (3.31) can be rewritten as,

$$\mathbf{R}_v = \int \psi'^*_v \boldsymbol{\mu} \psi''_v \, \mathrm{d}x, \tag{3.34}$$

where ψ'_v and ψ''_v are the vibrational wave functions of lower and upper states respectively, and x is the displacement of the internuclear distance from the equilibrium position. If the dipole moment $\boldsymbol{\mu}$ is zero, then $\mathbf{R}_v = 0$ and all vibrational transition are forbidden. If $\boldsymbol{\mu}$ is non zero, it can be expanded to a Taylor series

$$\boldsymbol{\mu} = \boldsymbol{\mu}_e + \left(\frac{\mathrm{d}\boldsymbol{\mu}}{\mathrm{d}x}\right)_e x + \frac{1}{2!}\left(\frac{\mathrm{d}^2\boldsymbol{\mu}}{\mathrm{d}x^2}\right)_e x^2 + \ldots, \tag{3.35}$$

where the subscript "e" refers to the equilibrium configuration. From Eq. (3.34), the $\mathbf{R}_v$ then becomes

$$\mathbf{R}_v = \boldsymbol{\mu}_e \int \psi'^*_v \psi''_v \, \mathrm{d}x + \left(\frac{\mathrm{d}\boldsymbol{\mu}}{\mathrm{d}x}\right)_e \int \psi'^*_v x \psi''_v \, \mathrm{d}x + \ldots. \tag{3.36}$$

The first term is zero because the two eigenfunctions are orthogonal to each other, and the second term is non-zero only if $\Delta v = \pm 1$. In the harmonic oscillator, since the spacing between the levels are equal, all transitions obey this selection rule being coincident at a wavenumber ω.

3.3.2 Experimental Setup

The infrared absorption spectra were recorded on FTIR 6100 spectrometer (JASCO Corp.) equipped with a Optistat®CF cryostat (Oxford Instrument) [17]. The temperature range explored was from 6 K to 100 K and the wavenumber range was from 400 to 4000 cm^{-1}.

Spectrometer

FTIR 6100 spectrometer is a standard Fourier transform infrared spectrometer. It consists of high-intensity ceramic IR source, 28° Michelson interferometer with Ge/KBr beam splitter, and DLATGS detector. The accuracy of wavenumber is within ±0.01 cm^{-1} (theoretical value), and the maximum resolution is 0.5 cm^{-1}. In order to diminish the undesirable peaks of water vapor, the instrument's chamber, where the cryostat was placed, was continuously purged with dried air during the measurement.

Cryostat

The cryostat works on the continuous flow principle, i.e. liquid helium is transferred from a separate Dewar and circulated through a transfer tube to the heat exchanger of the cryostat (Fig. 3.7). The cryostat consists of two cylindrical cans (Fig. 3.8), one inside the other. Sample is put inside the inner can which is filled with heat exchange gas (helium). The space between the two cans is evacuated to insulate the thermal conduction. Both cans have windows of KRS-5 crystal to let the IR beam transmit.

On cooling the sample room, the cold helium gas passes through the heat exchanger. Temperature is controlled by using the heater located near the sample holder and regulating the amount of gas flow. A thermometer attached at the heat exchanger is referred for the temperature control.

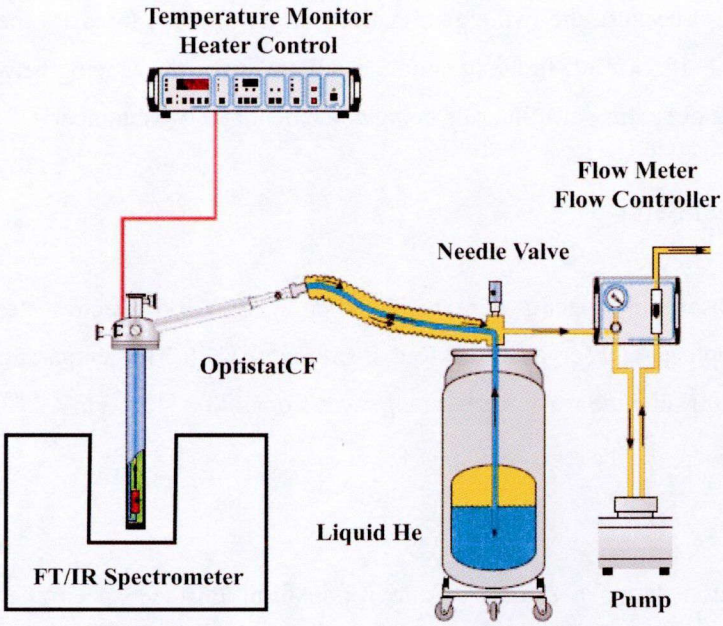

Fig. 3.7 Schematic view of the cryo-system for the infrared absorption measurement [17].

Sample Holder

Sample is loaded from the top of the cryostat using a rod on which the sample holders are attached. The length of the rod is adjustable from the outside so that the sample can be positioned on the beam line to obtain the maximum absorption signal. The sample holder consists of two pieces of KBr (or KRS-5) single crystal plates, between which a drop of sample is sandwiched. All the samples measured in this study were liquid at room temperature. In order to prevent the sample from evaporation, it was installed into the cryostat, which had already been cooled down to ~ 100 K, immediately after the sampling. Two or three sample holders were attached on the rod in line, one of which was kept empty to be used as reference background and the other holders were used for the sample measurement. The sample temperature was measured by a chromel-gold/iron thermocouple attached to the reference holder. The ice point was taken as a reference temperature. The thermocouple was calibrated at 77.3 K (liquid nitrogen), 20.4 K (liquid hydrogen) and 4.2 K (liquid helium) referring 273.15 K (ice point). The precision of the reading of the digital voltmeter was ±1 μV, corresponding to about 0.06 K below 100 K. The actual temperature precision was determined by the temperature fluctuations as well as the temperature difference between the reference plate and the sample plate, which was at largest about ±4 μV corresponding to ±0.24 K.

In most cases, the background measurement was made before the sample measurement in order to minimize the undesirable signal from carbon dioxide in the dried air.

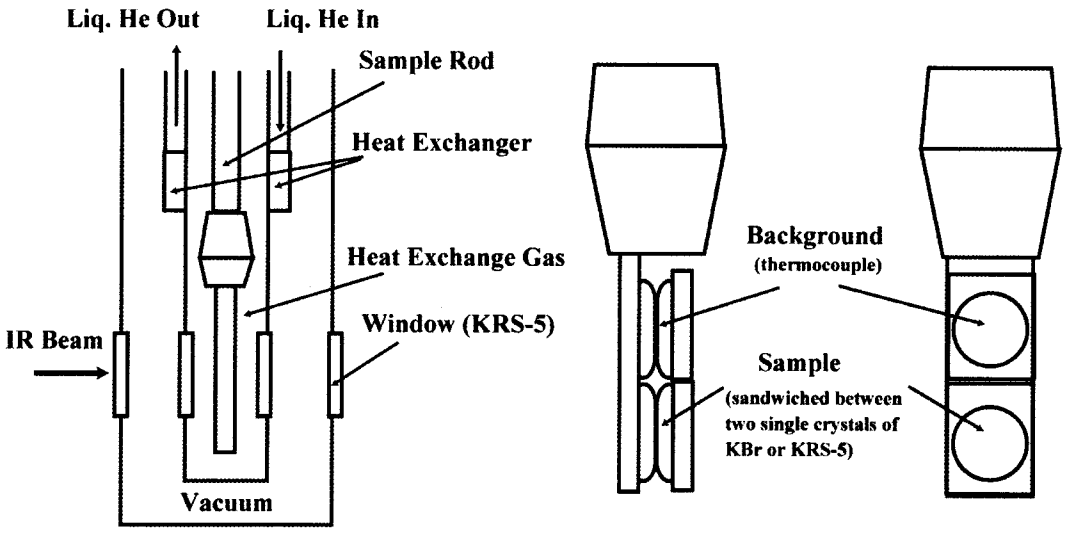

Fig. 3.8 Sketch of the cryostat (left) and the sample holder (right).

3.4 Data Analysis of IR Spectra

3.4.1 Assignment of Vibrational Modes

As the first step of data analysis, the absorption bands observed were assigned. The assignments were undertaken referring to the results of analogous molecules (mostly of the non-deuterated compounds), which had been assigned before. In addition, quantum mechanical computation was carried out to obtain the IR spectra. The computation was made with Gaussian 09 [18] using density functional theory (DFT) with the B3LYP method and utilizing the 6-31G(d) basis set for all atoms. All calculations refer to an isolated molecule (e.g. gas phase), and the influences from intermolecular interactions were not considered. The vibrational modes contributing to IR absorptions were analyzed using the animation mode of GaussView 5 [19] and assignments were made on the basis of these visualizations.

3.4.2 Absorbance Intensity

On the analysis of the IR absorption spectra in this study, the temperature dependence of the peak intensities were investigated. Absorption intensities are obtained by integrating the peak area. When a peak consists of several components (a double peak or a peak with shoulders), it has to be decomposed by curve fitting. In this study, the spectra were fitted by Voigt functions which is the

convoluted functions of Gaussian and Lorentzian functions.

It should be noted that the spectra obtained in this work were the absorbance A and not absorption coefficient α (Eq. (3.33)), so the peak intensity depends on the sample thickness d. Since the sample thickness vary from measurement to measurement, the intensities between different measurement sets are not comparable, which is possible only for the data in the same measurement run.

3.5 NMR Measurements

Nuclear magnetic resonance (NMR) measurements were made to obtain the deuteration degree of the methyl groups. NMR spectra, including ^1H, were recorded on a JOEL JNM-ECA500 spectrometer. $CDCl_3$ was used as solvent. The deuteration degrees were estimated by taking the ratio of the peak integrals assigned to the protons in the methyl groups and in the molecular frame. Chemical shifts are reported in ppm from tetramethylsilane with reference to internal residual solvent, $CHCl_3$ (δ 7.24).

3.6 References for Chapter 3

[1] S. R. Gopal, *Specific Heats at Low Temperatures* (Plenum Press, New York, 1966).

[2] T. Matsuo, K. Kohno, A. Inaba, T. Mochida, A. Izuoka and T. Sugawara, *J. Chem. Phys.* **108** (1998) 9809.

[3] R. Bachmann, F. J. Di Salvo, T. H. Geballe, R. L. Greene, R. E. Howard, C. N. King, H. C. Kirsch, K. N. Lee, R. E. Schwall, H. U. Thomas and R. B. Zubeck, *Rev. Sci. Instrum.* **43** (1972) 205.

[4] R. E. Schwall, R. E. Howard and G. R. Stewart, *Rev. Sci. Instrum.* **46** (1975) 1054.

[5] G. R.Stewart, *Rev. Sci. Instrum.* **54** (1983) 1.

[6] J. S. Hwang, K. J. Lin and C. Tien, *Rev. Sci. Instrum.* **68** (1997) 94.

[7] H. Suzuki, A. Inaba and C. Meingast, *Cryogenics* **50** (2010) 693.

[8] Quantum Design, 11578 Sorrento Valley Road, San Diego, CA 92121. http://www.qdusa.com.

[9] J. C. Lashley, M. F. Hundley, A. Migliori, J. L. Sarrao, P. G. Pagliuso, T. W. Darling, M. Jaime, J. C. Cooley, W. L. Hults, L. Morales, D. J. Thoma, J. L. Smith, J. Boerio-Goates, B. F. Woodfield, G. R. Stewart, R. A. Fisher and N. E. Phillips, *Cryogenics* **43** (2003) 369.

[10] E. Dachs and C. Bertoldi, Eur. *J. Mineral* **17** (2005) 251.

[11] C. A. Kennedy, M. Stancescu, R. A. Marriott and M. A. White, *Cryogenics* **47** (2007) 107.

[12] K. Saito, M. Massalska-Arodź, S. Ikeuchi, M. Maekawa, J. Ściesiński, E. Ściesińska, J. Mayer, T. Wasiutynski and M. Sorai, *J. Phys. Chem. B* **108** (2004) 5785.

[13] A. Inaba, H. Suzuki, J. Krawczyk, and M. Massalska-Arodz, *Chem. Phys. Lett.* **463** (2008) 90.

[14] H. Kawaji in *Comprehensive Handbook of Calorimetry and Thermal Analysis,* ed. by The Japan Society of Calorimetry and Thermal Analysis (John Wiley & Sons, Ltd, 2004), p.189-190.

[15] S.V.R. Mastrngelo and R.W. Dornte, *J. Am. Chem. Soc.*, **77** (1955) 6200.

[16] W. Schottky, *Hysikalischez Eitschrift* **23** (1922) 448.

[17] Oxford Instruments, Tubney Woods, Abingdon, Oxfordshire, OX13 5QX, UK. http://www.oxinst.com/Pages/home.aspx

[18] M.J. Frisch, G.W. Trucks, H.B. Schlegel, G.E. Scuseria, M.A. Robb, J.R. Cheeseman, G. Scalmani, V. Barone, B. Mennucci, G.A. Petersson, H. Nakatsuji, M. Caricato, X. Li, H.P. Hratchian, A.F. Izmaylov, J. Bloino, G. Zheng, J.L. Sonnenberg, M. Hada, M. Ehara, K. Toyota, R. Fukuda, J. Hasegawa, M. Ishida, T. Nakajima, Y. Honda, O. Kitao, H. Nakai, T. Vreven, J.A. Montgomery Jr., J.E. Peralta, F. Ogliaro, M. Bearpark, J.J. Heyd, E. Brothers, K.N. Kudin, V.N. Staroverov, R. Kobayashi, J. Normand, K. Raghavachari, A. Rendell, J.C. Burant, S.S. Iyengar, J. Tomasi, M. Cossi, N. Rega, J.M. Millam, M. Klene, J.E. Knox, J.B. Cross, V. Bakken, C. Adamo, J. Jaramillo, R. Gomperts, R.E. Stratmann, O. Yazyev, A.J. Austin, R. Cammi, C. Pomelli, J.W. Ochterski, R.L. Martin, K. Morokuma, V.G. Zakrzewski, G.A. Voth, P. Salvador, J.J. Dannenberg, S. Dapprich, A.D. Daniels, O. Farkas, J.B. Foresman, J.V. Ortiz, J. Cioslowski and D.J. Fox, *Gaussian 09, Revision A.02* Gaussian Inc., Wallingford, CT, 2009.

[19] A. Frisch, H.P. Hratchian, R.D. Dennington II, T.A. Keith, John Millam, A.B. Nielsen, A.J. Holder and J. Hiscocks. *GaussView Version 5.0.*, Gaussian, Inc., June 2009.

Chapter 4

Orientational Ordering of Partially Deuterated Methyl Groups in Solid 4-Methylpyridine

4.1 Introduction

From the preceding works on hydrogen bond system as well as the ammonium ion system, it was expected that the compounds showing a significant proton tunneling are more likely to show a dramatic deuteration effect on the phase behavior. From the view point of the mass effect on the delocalized wave functions, this prediction seemed reasonable and also true for the methyl group systems. For this reason, the series of investigations was started with 4-methylpyridine (4MP) whose methyl groups rotate almost freely in crystal. The rotational tunnel excitations of 4MP have been observed at 519 μeV by high resolution INS measurements [1]. To the best of my knowledge, this is the largest value obtained for the methyl group system in solid.

The crystal structure of 4MP is already established by neutron diffraction measurements [2,3]. The structure is tetragonal ($I4_1/a$) at 4 K with four molecules in a primitive cell (Fig. 4.1). The dominant dipole-dipole interaction leads to an anti-parallel ordering of the molecules with respect to the c axis. The shortest intermolecular C-C distance is reported to be 3.430(2) Å [2] or 3.462 Å [4] occurring between face-to-face methyl groups, which is significantly shorter than the van der Waals distance (4 Å) of methyl groups. In order to explain this, Ohms *et al.* [5] proposed that the methyl groups are twisted by ±60° with respect to each other. The next shortest intermolecular C-C distances of 3.956(1) Å occur parallel to a and b axes, forming two equivalent sets of orthogonal infinite chains of methyl groups (Fig. 4.1). The carbon site of the methyl group is fixed on a point having twofold symmetry, while the proton sites of the rotor are indistinguishable in the probability density, which is revealed by the map of isodensity contours of the proton distribution (Fig. 4.2) [2]. 4MP undergoes a phase transition at 254 K with symmetry change to $I4_1/amd$ above this temperature.

There have been a lot of discussions about the rotational dynamics of the methyl groups in 4MP at low temperature. In particular, the difference between lithium acetate dihydrate (LiAc) and 4MP has been extensively discussed, since they are similar in crystal structure, both having pairs of

face-to-face methyl groups with rather short distance, ~ 3.5 Å (4MP) and ~ 3.3 Å (LiAc), and also short distances between the neighboring pairs, 3.95 Å (4MP) and 3.4 Å (LiAc). For LiAc, the rotational states were described in the framework of coupled pair rotation, in which the coupling in the facing pairs is more important than the coupling between the neighboring pairs [6-9]. For 4MP, on the other hand, the INS spectra indicated some additional features in the rotational states. In order to explain the somewhat complicated structure of tunneling spectrum, Clough *et al.* [1] have introduced a dynamic coupling model between the facing two methyl groups, resulting from mutual gauge or vector potential. Fillaux *et al.* [10-12] introduced the quantum sine-Gordon equation, taking into account the quantum interaction between the methyl groups on the one-dimensional infinite chain along *a* and *b* axes. The resultant rotational states were categorized into several kinds, the collective in-phase and out-of-phase excitations and the spatially localized kink (soliton) and breather (doublet) modes. The strong inelastic peak at 519 μeV was assigned to the breather modes. Neumann *et al.* opposed to this sine-Gordon model and proposed the rotational-libration and rotor-rotor coupling model [13], which is based on on the same framework of the coupled pair model, but additional contributions of the coupling between the rotation of the methyl group and the libration of the whole molecule is also taken into account. In spite of these active discussions, the universal agreement has not been obtained yet.

Some investigations of the deuteration effects on 4MP have also been made. Adel *et al.* [14] found a second-order phase transition at 5.27 K for C_5H_4N-CH_2D by adiabatic calorimetry which is absent for the non-deuterated 4MP. Fillaux *et al.* [12] found inelastic peaks in INS spectra for C_5H_4N-CH_2D at 388 μeV and 436 μeV at 2 K, in which the lower frequency band (388 μeV) merges progressively into the band at 436 μeV at 5 K. They again applied the sine-Gordon theory to explain these results. Neumann *et al.* [13] explained the same results using their rotational-libration and rotor-rotor coupling model.

In this study, heat capacity measurements were made for four isotopic species of 4MP, that is, C_5H_4N-CH_3, C_5H_4N-CH_2D, C_5H_4N-CHD_2 and C_5H_4N-CD_3 between 0.35 K and 300 K. The main purposes were (1) to investigate the phase behavior of all four compounds, (2) to establish their thermodynamic quantities, and (3) to compare the results with those of LiAc.

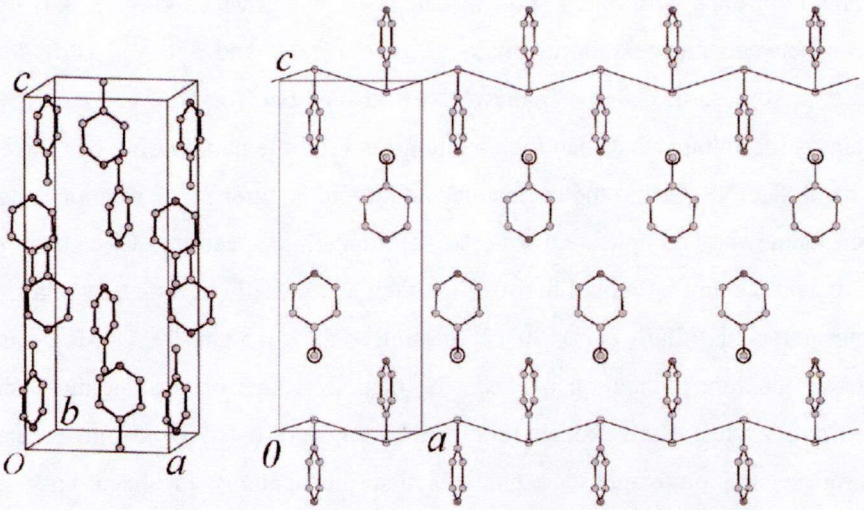

Fig. 4.1 Schematic view of the structure of the 4MP crystal at 10 K [2]. (Left) The unit cell. (Right) The projection onto the (*a*, *c*) plane showing the infinite chains parallel to *a* (along the zigzag line) or parallel to *b* (circles). The positions of proton are not shown.

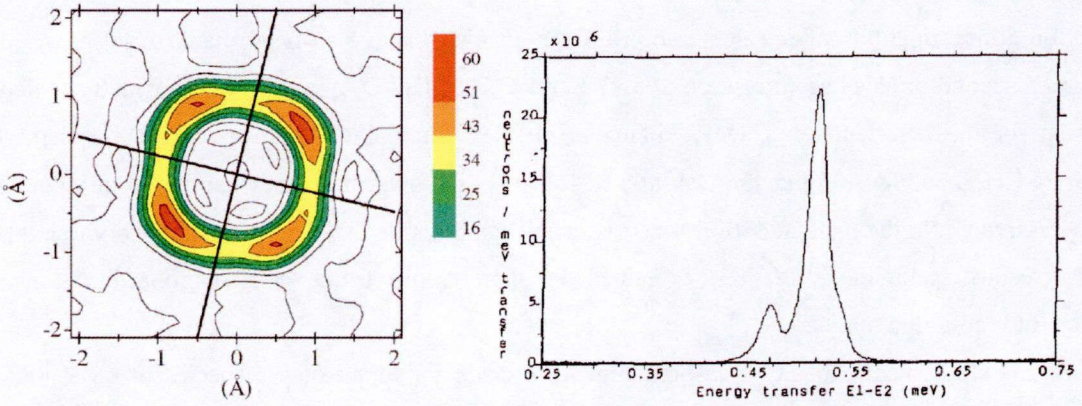

Fig. 4.2 (Left) Map of isodensity contours of the proton distribution in the rotational plane of the methyl groups in 4MP at 10 K, obtained with the Fourier difference method. The solid lines represent the orientations of the molecular planes [2]. (Right) INS spectrum of 4MP at 2.3 K showing a strong inelastic peak at 519 μeV together with two small peaks [1].

4.2 Experimental

C_5H_4N-CH_3 (99%) and C_5H_4N-CD_3 (98%D) were purchased from Sigma Aldrich. C_5H_4N-CH_2D and C_5H_4N-CHD_2 were synthesized at LADIR-CNRS, France.

The heat capacity measurements were carried out between 3 K and 300 K by adiabatic calorimetry, and between 0.35 K and 20 K by relaxation calorimetry. The amounts of the sample used in the adiabatic calorimetry were 1.9289 g (0.02071 mol) for C_5H_4N-CH_3, 1.8445 g (0.01960 mol) for C_5H_4N-CH_2D, 2.0143 g (0.02117 mol) for C_5H_4N-CHD_2 and 1.9865 g (0.02066 mol) for C_5H_4N-CD_3, respectively.

The amounts of the sample used for the relaxation calorimetry were 0.29 mg (3.1×10^{-6} mol) for C_5H_4N-CH_3, 0.64 mg (6.8×10^{-6} mol) for C_5H_4N-CH_2D, 0.77 mg (8.1×10^{-6} mol) for C_5H_4N-CHD_2, and 0.37 mg (3.8×10^{-6} mol) for C_5H_4N-CD_3, respectively. Since 4MP is liquid at room temperature, the liquid sample cell (see Section 3.1.5 Case 2) was used. The sample amounts on the relaxation calorimetry were determined referring the heat capacities of adiabatic calorimetry.

4.3 Results and Discussion

4.3.1 Overview of the Heat Capacity Results

Fig. 4.3 shows the heat capacities of 4MP and its deuterated analogs over the whole temperature range. All the compounds showed a solid-solid phase transition around 254 K. The deuterated compounds (C_5H_4N-CH_2D, C_5H_4N-CHD_2 and C_5H_4N-CD_3) have a phase transition below 10 K. Several small bumps were also observed in heat capacity between 150 K and 250 K for all samples. These anomalies were not reported in the previous measurements for C_5H_4N-CH_3 by Messerly *et al.* [15] or Chirico *et al.* [16]. This may be due to the water impurity of the sample, because the compounds are highly hygroscopic. Indeed, the sample purities calculated by the fractional melting method (see Section 3.2.1) were about 98.1% on average, which is significantly lower than those in the previous two reports (99.97% [15] and 99.925% [16]). The purity and the thermodynamic quantities associated with fusion are tabulated in Table 4.1. Among the compounds measured, the enthalpies and entropies of fusion are similar, except for C_5H_4N-CH_2D which has slightly smaller values than the others.

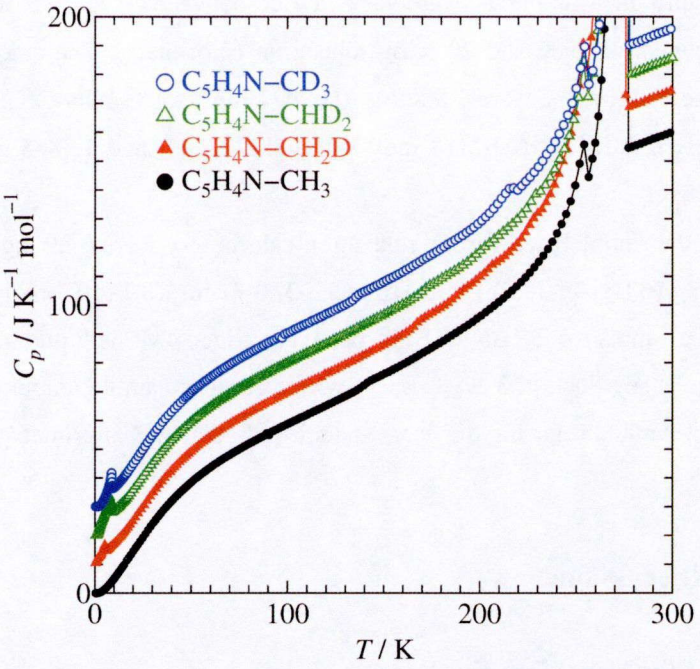

Fig. 4.3 Molar heat capacities of C_5H_4N-CH_3, C_5H_4N-CH_2D, C_5H_4N-CHD_2 and C_5H_4N-CD_3 between 0.35 K and 300 K. The ordinate is for C_5H_4N-CH_3. The results for the other three compounds are successively shifted upward by 10 J K^{-1} mol^{-1}.

Table 4.1 Thermodynamic quantities associated with the phase transition and fusion together with the purity of the samples measured. The values obtained by Messerly *et al.* [15] and Chirico *et al.* [16] are also shown.

	T_{tr} [cr(I)→cr(II)]	T_{fus}	$\Delta_{fus}H$	$\Delta_{fus}S$	purity(%)	T_{tp}
	K	K	kJ mol^{-1}	J K^{-1} mol^{-1}		K
C_5H_4N-CH_3	253.9	275.7	11.99	43.84	98.12	276.6
C_5H_4N-CH_2D	254.3	274.6	11.49	42.34	98.19	276.1
C_5H_4N-CHD_2	254.4	275.5	11.94	43.7	98.12	276.6
C_5H_4N-CD_3	254.2	276.1	12.09	44.12	98.11	277.1
C_5H_4N-CH_3 (ref.)						
Messerly *et al.*	255.00	276.8	12.5823		99.97	276.817
Chirico *et al.*					99.925	276.826

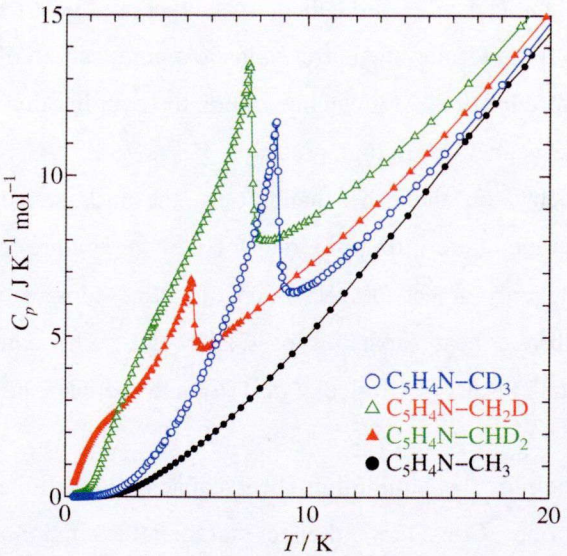

Fig. 4.4 Molar heat capacities of C_5H_4N-CH_3, C_5H_4N-CH_2D, C_5H_4N-CHD_2 and C_5H_4N-CD_3 below 20 K. C_5H_4N-CD_3 has a λ-shaped phase transition at 8.6 K. C_5H_4N-CH_2D and C_5H_4N-CHD_2 show a phase transition at 5.2 K and 7.5 K, respectively, with a broad hump in heat capacity.

4.3.2 Low Temperature Heat Capacities

Fig. 4.4 shows the heat capacities of 4MP and its deuterated analogs below 20 K. C_5H_4N-CD_3 undergoes a λ-shaped phase transition at 8.6 K. C_5H_4N-CH_2D and C_5H_4N-CHD_2 show a phase transition at 5.2 K and 7.5 K respectively, with a broad hump in heat capacity. C_5H_4N-CH_3 does not undergo such phase transition, but it shows a long thermal relaxation around 10 K.

C_5H_4N-CH_3

The thermal relaxation with a long time constant for C_5H_4N-CH_3 may be due to the nuclear spin conversion of the protons associated with the tunnel excitation of methyl groups (see Section 2.2). In adiabatic calorimetry, as mentioned in the experimental section (Section 3.1.1), the temperature before and after the heating is obtained by extrapolating the temperature drift to the mid-point of the heating period. With the slow relaxation, the temperature monitoring takes long time to reach to the equilibrium state. Fig. 4.5 demonstrates the temperature variation after the heating at 10 K. Comparing to the normal equilibration time at this temperature, which is about one minute, the relaxation time observed is significantly longer (about 40 minutes). Two types of heat capacities, therefore, can be derived using different final temperatures (T_f); one is obtained by extrapolating the data soon after the heating, and the other one is obtained by extrapolation the data after the long

relaxation. The resultant heat capacities are called "instantaneous" heat capacity and "equilibrium" heat capacity, respectively. The former one corresponds to a composition of spin species frozen-in at the initial temperature before heating. At low temperature, the equilibration time becomes too long to obtain the equilibrium heat capacity with high precision.

In relaxation calorimetry, on the other hand, only the instantaneous heat capacities were measured. This is because the curve fitting program for the temperature relaxation equipped on the calorimeter (PPMS) could only detect the relaxation of lattice composition. Fig. 4.6 shows both instantaneous and equilibrium heat capacities of $C_5H_4N\text{-}CH_3$. The equilibrium one is in good agreement with the previous results of Chirico *et al.* [16], and the instantaneous one with the results of Messerly *et al.* [15].

The excess contribution in the equilibrium heat capacity is definitely due to the rotational tunneling of the methyl groups. Considering the fact that tunnel excitation peaks have been observed around 519 μeV by INS measurement, Schottky heat capacity (Section 3.2.3) of two energy levels spaced by 519 μeV with equivalent degeneracy $g_1/g_0 = 1$ was calculated. The result of the calculation reproduces well the equilibrium heat capacity (the solid curve in Fig. 4.6). Unfortunately, this result itself does not exclusively support any models of the rotational states. For example, in the single rotor model with three-fold symmetric potential, which is the simplest but less realistic for 4MP, the tunneling states are expected to be A and E states. As mentioned in Section 2.2, if the nuclear spin states of protons are taken into account, both levels are fourfold degenerated, so that the ratio of degeneracy is $g_1/g_0 = 1$. If one accepts the excitation observed at 519 μeV as the $A \leftrightarrow E$ transition, the equilibrium heat capacity follows the solid curve in Fig. 4.6. For the coupled rotor models, although the energy scheme becomes slightly more complicated, the resultant excess heat capacity is almost the same. The excess heat capacity based on the sine-Gordon model is also similar. This is because the framework of both the coupled rotor model and the sine-Gordon model is the same to the single rotor model. These models were proposed to explain the detailed structure of the INS spectra. Generally, heat capacity measurement at low temperature is advantageous to examine the basic structure of the energy scheme, but it is unsuitable for the investigations of their detailed structure. INS measurement, on the other hand, provides the information about the detailed structure of the energy scheme, but it is not suited for the investigation of the whole structure of the scheme. This is because INS only detects the excitation between two levels. In this respect, the results of the present calorimetric study for 4MP are valuable in confirming the basic structure of the energy scheme used in the various models proposed in the past.

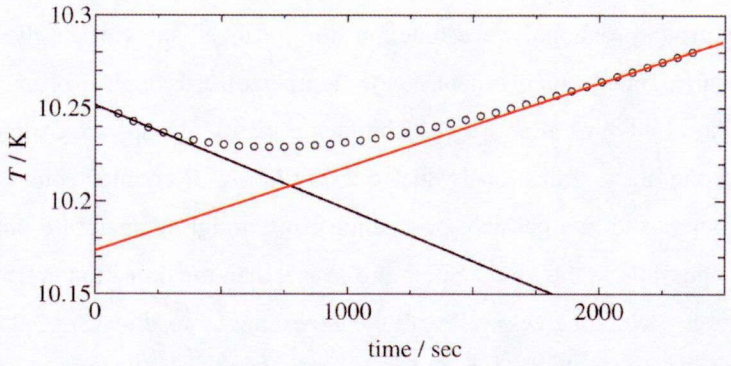

Fig. 4.5 Temperature drift after heating was off in the adiabatic calorimetric measurement, showing a long thermal relaxation due to the nuclear spin conversion of C_5H_4N-CH_3. The limiting slope mainly came from the heating effect of the measuring current applied to the thermometer. The lines show the examples of two types of data extrapolation to obtain the final temperature (T_f).

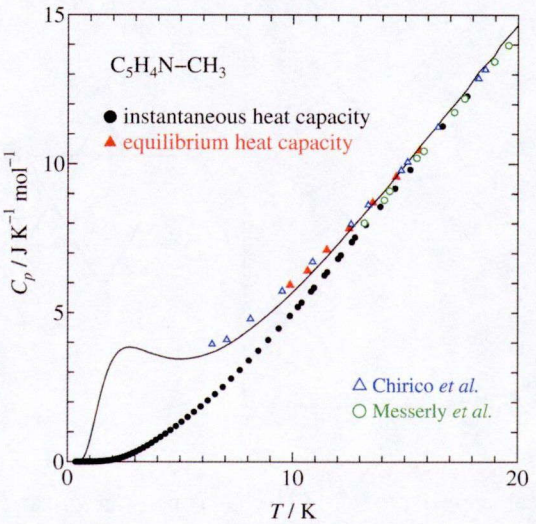

Fig. 4.6 Equilibrium and instantaneous heat capacities of C_5H_4N-CH_3. The heat capacities obtained previously by Chirico *et al.* [16], and Messerly *et al.* [15] are also shown. The solid curve shows a Schottky type heat capacity (g_1/g_0=1) added to the instantaneous heat capacity.

C_5H_4N-CD_3

C_5H_4N-CD_3 undergoes a λ-shaped phase transition at 8.6 K. In order to extract the contribution from the transition, the lattice heat capacity was estimated using the heat capacity of C_5H_4N-CH_3, taking into account the mass increment (Section 3.2.3). The calculated base line represents well the heat capacities for C_5H_4N-CD_3 between 17 K and 24 K (Fig. 4.7). From the excess heat capacity, the transition entropy was calculated to be ΔS = 3.0 J K^{-1} mol^{-1} (Fig. 4.8). Like the deuteretion-induced

phase transitions in hydrogen bonded system, this transition is due to the mass effect on the quantum motion, that is, the ground torsional wave functions are localized showing up the orientation of the rotor in the classical regime, which orders at low temperature through a phase transition. If one accepts the suggestion by Ohms *et al.* [5] that the facing methyl groups are coupled and twisted by ±60° to each other, the phase transition is due to the ordering of coupled rotors. Suppose that the coupled methyl groups have two possible orientations in the high temperature phase (Fig. 4.7) and only one of them is possible in the low temperature phase, then the transition entropy is $\Delta S = (1/2)\, R \ln 2 = 2.88$ J K^{-1} mol^{-1}, which agrees well with the experimental result ($\Delta S = 3.0$ J K^{-1} mol^{-1}). This result is analogous to that of fully deuterated LiAc [9], indicating that the coupling between the two facing methyl groups is stronger than the other intermolecular interactions. The sine-Gordon theory seems therefore inappropriate to explain the rotational state at least of C_5H_4N-CD_3. The interaction through the chains of methyl groups seems to be the second most important factor serving the correlation paths of the cooperative ordering.

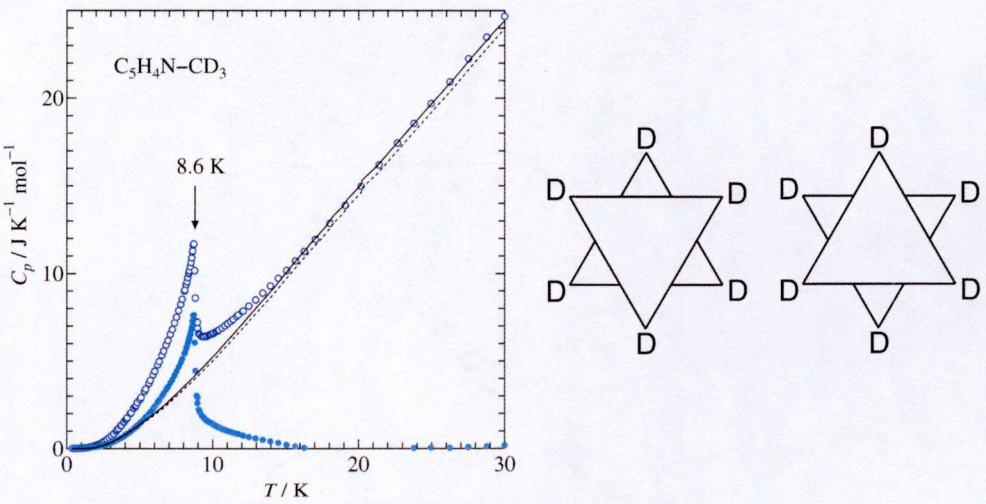

Fig. 4.7 (Left) Molar heat capacity of C_5H_4N-CD_3 (open-marks) and the excess heat capacity (filled-marks). The solid curve shows the normal heat capacity and the dot curve shows the heat capacity of C_5H_4N-CH_3. (Right) Two possible orientations of the coupled methyl groups for C_5H_4N-CD_3 in the high temperature phase.

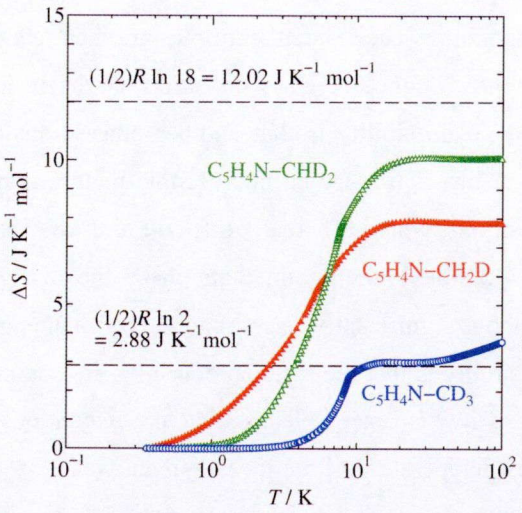

Fig. 4.8 Entropy gain due to the phase transition for the methyl deuterated 4MPs. The transition entropy of C_5H_4N-CD_3 agrees well with the expected value of (1/2) R ln 2, while those of C_5H_4N-CH_2D and C_5H_4N-CHD_2 are smaller than that expected (1/2) R ln 18.

C_5H_4N-CH_2D and C_5H_4N-CHD_2

C_5H_4N-CH_2D and C_5H_4N-CHD_2 also showed a phase transition at 5.2 K and 7.5 K respectively, with a broad hump in heat capacity. The lattice heat capacity of C_5H_4N-CH_2D and C_5H_4N-CHD_2 were estimated by scaling the instantaneous heat capacity of C_5H_4N-CH_3 against temperature (Fig. 4.9). The scaling factor was 0.975 for C_5H_4N-CH_2D and 0.963 for C_5H_4N-CHD_2, respectively. The transition entropies were ΔS = 7.9 J K^{-1} mol^{-1} for C_5H_4N-CH_2D and ΔS = 10.1 J K^{-1} mol^{-1} for C_5H_4N-CHD_2, respectively (Fig. 4.8).

If the order-disorder model of the coupled rotors, which successfully explained the phase transition of C_5H_4N-CD_3, is applied to C_5H_4N-CH_2D and C_5H_4N-CHD_2, 18 (=3×3×2) orientations are possible for the coupled rotor in the higher temperature phase (Fig. 4.10). If only one of them is possible in the low temperature phase, the transition entropy is ΔS = (1/2) R ln 18 = 12.02 J K^{-1} mol^{-1}. The experimental values are significantly smaller than this quantity. As far as the equilibrium heat capacities are obtained, the deficient entropies should be compensated somewhere. Since the methyl groups are likely to rotate freely in the liquid phase, the rotational entropies seem to be the same for all the compounds except for the difference of R ln 3 originating from the different rotational symmetry. Since the entropies of fusion (Table 4.1) as well as the entropies of the transition at T = 254 K (not shown in Table 4.1) are similar and since there is no other thermal anomaly in the high temperature phase, the deficient entropies must be hidden in the low temperature phase.

There are three possible answers to explain the deficient entropies. One is the freezing of ordering process at low temperature. The residual entropies are then retained as frozen-in disorder in the glassy phase. However, no evidence of glass transition has been detected yet, such as a long thermal relaxation. The second possibility is that another phase transition is hidden at very low temperature below 0.35 K. If this is true, some microscopic picture is needed for the intermediate phase between the two transitions, which is actually difficult to draw. For example, even if only two orientations in Fig. 4.10 are possible in the intermediate phase, the configurational entropy is (1/2) R ln 2 = 2.88 J K^{-1} mol^{-1}, which is significantly larger than the residual entropy of C_5H_4N-CHD_2 (1.92 J K^{-1} mol^{-1}). The third possibility is that the residual entropies are compensated by some additional quantum states which are so low in energy levels that the excitations were not detected in this experiment. Since the lowest temperature of the measurement was 0.35 K, the energy levels should be spaced by less than 30 μeV. The high resolution ($\Delta E \sim 15$ μeV) INS measurements for C_5H_4N-CH_2D have revealed the tunnel excitations at 79 μeV, 388 μeV and 426 μeV at 2 K, which are much larger than 30 μeV. Incidentally, these contributions correspond to the heat capacity hump below 5 K. Investigations for much lower energy range could provide some evidences of such levels.

These results for the partially deuterated 4MPs show remarkable contrast to those of LiAc. In LiAc, the transition entropies of both -CH_2D and -CHD_2 compounds are almost equal to (1/2) R ln 18, showing that the orientational ordering is completed at the lowest temperatures of the measurement [9]. It can be thus concluded that the rotational states of the methyl groups are different between LiAc and 4MP not only for -CH_3 compounds but also for the -CH_2D and -CHD_2 compounds, and only the behaviors of -CD_3 compound are similar, in which the classical order-disorder model explains well the phase transition.

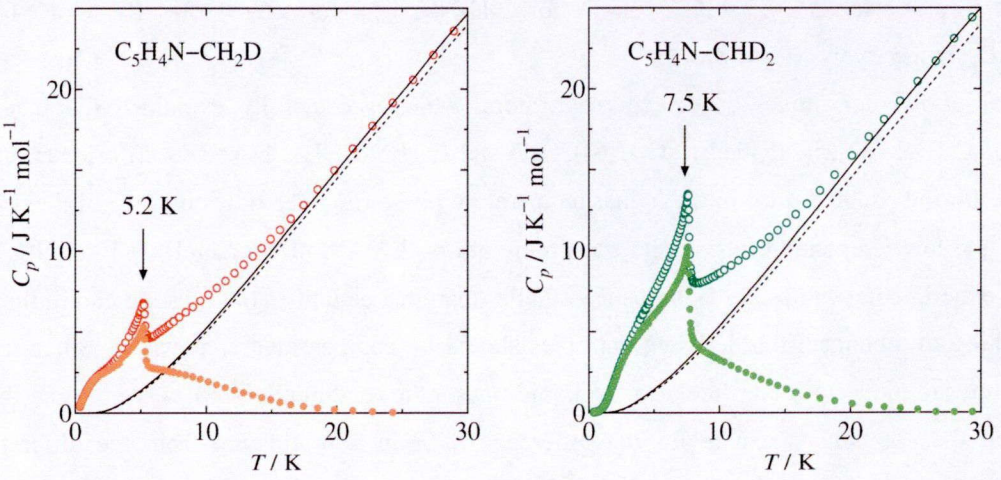

Fig. 4.9 Molar heat capacity (open-marks) and excess heat capacity (filled-marks) of C_5H_4N-CH_2D (left) and C_5H_4N-CHD_2 (right). The solid curves show the normal heat capacities and the dot curves show the heat capacity of C_5H_4N-CH_3.

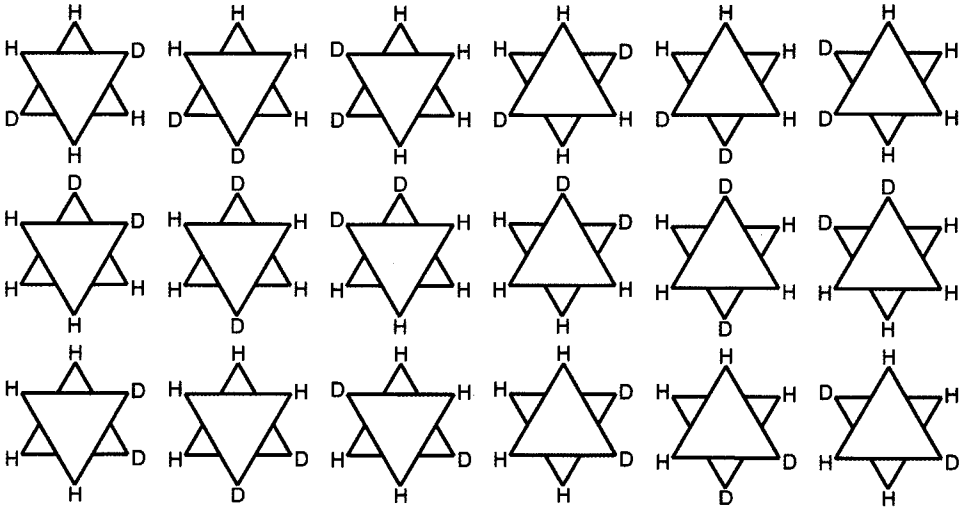

Fig. 4.10 Eighteen possible orientations of the coupled methyl group for C_5H_4N-CH_2D in the high temperature phase. If one of the orientations is possible in the low temperature phase, the transition entropy will be $\Delta S = (1/2)\, R \ln 18 = 12.02$ J K^{-1} mol^{-1}, which is significantly larger than the experimental value.

4.4 Summary

Heat capacity measurements were made for 4-methylprydine and its deuterated analogs (C_5H_4N-CH_3, C_5H_4N-CH_2D, C_5H_4N-CHD_2 and C_5H_4N-CD_3). C_5H_4N-CD_3 exhibits a λ-type phase transition at 8.6 K. C_5H_4N-CH_2D and C_5H_4N-CHD_2 show a phase transition at 5.2 K and 7.5 K respectively, with a broad hump in heat capacity. C_5H_4N-CH_3 does not undergo such phase transition, but it shows a long thermal relaxation around 10 K, which is attributed to the nuclear spin conversion of the protons in the methyl groups. The transition entropy is $\Delta S = 3.0$ J K^{-1} mol^{-1} for C_5H_4N-CD_3, $\Delta S = 7.9$ J K^{-1} mol^{-1} for C_5H_4N-CH_2D, and $\Delta S = 10.1$ J K^{-1} mol^{-1} for C_5H_4N-CHD_2. The orientational order-disorder model of the coupled methyl groups explains well the transition entropy of C_5H_4N-CD_3. For C_5H_4N-CH_2D and C_5H_4N-CHD_2, however, the experimental values are significantly smaller than that expected from the same model, indicating that the orientations of the methyl groups are not completed even at the lowest temperature of the measurement. These results show remarkable contrast to those of lithium acetate dehydrate, in which the transition entropy is explained by the classical order-disorder model of the coupled rotors.

4.5 References for Chapter 4

[1] C. J. Carlile, S. Clough, A. J. Horsewill and A. Smith, *Chem. Phys.* **134** (1989) 437.

[2] F. Fillaux, B. Nicolaï, W. Paulus, E. K. Morris and A. Cousson, *Phys. Rev. B* **68** (2003) 224301.

[3] C. J. Carlile, R. M. Ibberson, F. Fillaux and B. T. M. Willis, *Z. Kristallogr.* **193** (1990) 243.

[4] F. Fillaux, C. J. Carlile, *Phys. Rev. B* **42** (1990) 5990.

[5] U. Ohms, H. Guth, W. Treutmann, H. Dannohl, A. Schweig and G. Heger, *J. Chem. Phys.* **83** (1985) 273.

[6] B. Nicolai, A. Cousson and F. Fillaux, *Chem. Phys.* **290** (2003) 101.

[7] G.J. Kearley, B. Nicolai, P. G. Radaelli and F. Fillaux, *J. Solid State Chem.* **126** (1996) 184.

[8] F. Schroder, B. Winkler, E. Haussuhl, P.T. Cong, B. Wolf, M. Avalos-Borja, M. Quilichini and B. Hennion, *J. Chem. Thermodyn.* **42** (2010) 957.

[9] A. Inaba, unpublished.

[10] F. Fillaux and C. J. Carlile, *Chem. Phys. Lett.* **162** (1989) 188.

[11] F. Fillaux, C. J. Carlile and G. J. Kearley, *Phys. Rev. B* **58** (1998) 11416.

[12] F. Fillaux, C. J. Carlile and G. J. Kearley, *Phys. Rev. B* **44** (1991) 12280.

[13] M. A. Neumann, M. Plazanet, M. R. Johnson and H. P. Trommsdoff, *J. Chem. Phys.* **120** (2004) 2.

[14] H. den Adel, H. B. Brom, Z. Dokoupil and W. J. Huiskamp, *Phyica B* **111** (1981) 160.

[15] J. F. Messerly, S. S. Todd, H. L. Finke, W. D. Good, B. E. Gammon, *J. Chem. Thermodyn.* **20** (1988) 209.

[16] R. D. Chirico, S. E. Knipmeyer, W. V. Steele, *J. Chem. Thermodyn.* **31** (1999) 323.

Chapter 5

Orientational Ordering of Partially Deuterated Methyl Groups in Solid 2,6-Dichlorotoluene

5.1 Introduction

As another methyl group system showing rotational tunneling in solid, trihalogenomesitylenes (THMs) are also known. The rotational dynamics as well as the crystal structure of THMs have been extensively investigated by Meinnel *et al.* [1-3]. THM molecules have three methyl groups, each of which is surrounded by two halogen atoms (Fig. 5.1). The three methyl groups are not equivalent in the crystal, giving three sets of different rotational tunnel excitations observed by inelastic neutron scattering (INS) experiments (Fig. 5.2) [1]. With increasing the size of halogens, the spacing of the tunnel levels increases, which indicates that the methyl groups are less hindered (Fig. 5.2). Neutron diffraction measurements as well as the quantum mechanical calculation showed that the enlargement of the halogen size extends the intermolecular distances, which changes the hindering potential of the methyl groups [2]. Accordingly the rotational dynamics of the methyl groups of THMs can be controlled by changing the size of neighboring halogens.

In this context, it seems interesting to investigate the deuteration effects on the methyl groups surrounded by various sizes of halogens. In this study, for the sake of simplicity, deuteration effects on 2,6-dihalogenotoluenes (26DHTs) were investigated instead of THMs, because 26DHTs have only one methyl group in a molecule (Fig. 5.1). In this chapter, the results of the heat capacity measurements as well as IR absorption measurements for 2,6-dichlorotoluene (26DCT) and its methyl deuterated analogs are described. The crystal structure of 26DCT has not been clarified yet, while the tunnel splitting has been reported to be 1.56 μeV [4] which is actually signficantly smaller than that of THMs.

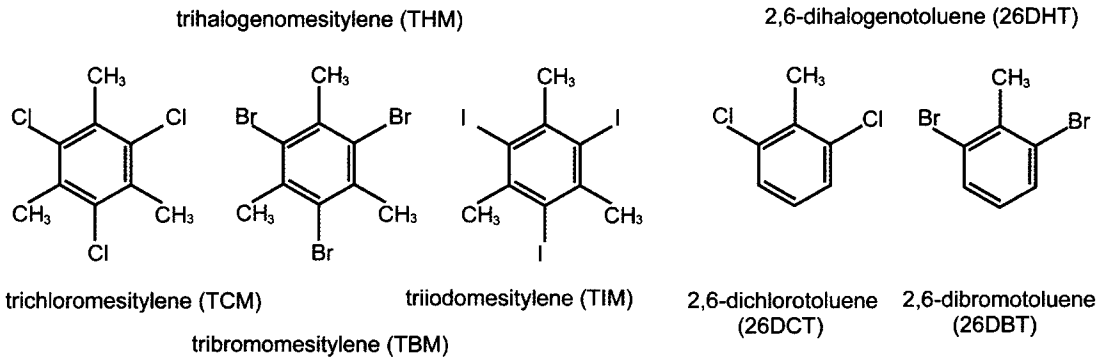

Fig. 5.1 Molecular structures of trihalogenomesitylenes (THMs) and 2,6-dihalogenotoluenes (26DHTs).

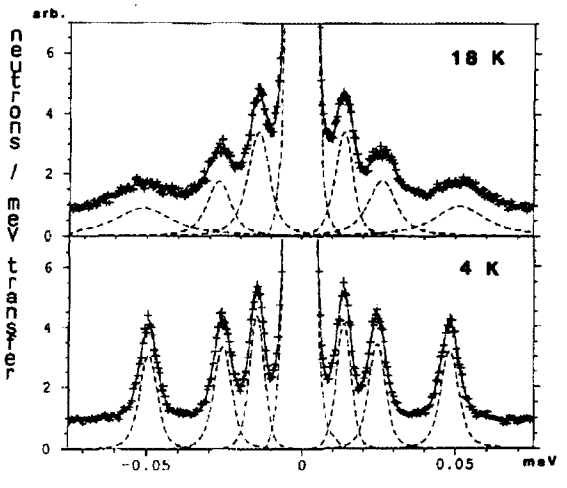

TCM:	4.3	9.2	13.1 μeV	at 1.5 K
TBM:	14.1	25.1	48.8 μeV	at 4.0 K
TIM:	14.4	26.7	87.4 μeV	at 1.5 K

Fig. 5.2 (Left) Inelastic peaks of tunnel excitations observed by INS measurements for tribromomesitylene (TBM) at 4 K and 18 K. (Right) Tunnel frequencies of three methyl groups for trichloromesitylene (TCM), TBM and triiodomesitylene (TIM) [1].

5.2 Experimental

5.2.1 Samples

The 26DCT ($C_6H_3Cl_2$-CH_3) (> 99%) was purchased from Tokyo Chemical Industry and distilled before the measurements. The three methyl-deuterated compounds were synthesized at Laboratory for Biomolecular Chemistry in Osaka University. The chemical purities of the four samples were determined using the fractional melting method (Section 3.2.1), which were 99.48% for $C_6H_3Cl_2$-CH_3, 99.71% for $C_6H_3Cl_2$-CH_2D, 98.70% for $C_6H_3Cl_2$-CHD_2 and 99.12% for $C_6H_3Cl_2$-CD_3, respectively. The deuteration degrees were determined by ^{1}H NMR measurement, which were 96%D

for $C_6H_3Cl_2$-CH_2D, 104%D for $C_6H_3Cl_2$-CHD_2 and 98%D for $C_6H_3Cl_2$-CD_3, respectively. ^1H NMR (500 HMz, $CDCl_3$) δ 7.25 (2H at the *meta* positions of 2,6-dichlorobenzene), 7.03 (1H at the *para* position of 2,6-dichlorobenzene), 2.43 (protons of the methyl groups). The deuteration degrees were estimated by taking the ratio of the peak integrals at δ 7.03 and δ 2.43.

5.2.2 Heat Capacity Measurement

The heat capacity measurements were made between 5 K and 300 K by adiabatic calorimetry, and between 0.35 K and 20 K by relaxation calorimetry. The amounts of samples used for the adiabatic calorimetry were 0.70917 g (4.4040 mmol), 0.74630 g (4.6058 mmol), 0.90024 g (5.5216 mmol) and 0.35358 g (2.1554 mmol) for $C_6H_3Cl_2$-CH_3, $C_6H_3Cl_2$-CH_2D, $C_6H_3Cl_2$-CHD_2 and $C_6H_3Cl_2$-CD_3, respectively, after buoyancy correction.

The amounts of the sample used for the relaxation calorimetry were 0.999 mg (6.20 μmol), 0.991 mg (6.11 μmol), 0.745 mg (4.57 μmol) and 1.036 mg (6.31 μmol) for $C_6H_3Cl_2$-CH_3, $C_6H_3Cl_2$-CH_2D, $C_6H_3Cl_2$-CHD_2 and $C_6H_3Cl_2$-CD_3, respectively. The copper liquid sample cells (Section 3.1.5 Case 2) were used. The sample amounts used for the relaxation calorimetry were determined referring the heat capacities of adiabatic calorimetry.

5.2.3 IR Measurement

Infrared absorption measurements were made for four 26DCTs ($C_6H_3Cl_2$-CH_3, $C_6H_3Cl_2$-CH_2D, $C_6H_3Cl_2$-CHD_2 and $C_6H_3Cl_2$-CD_3) between 6 K and 100 K in the spectral range from 400 cm^{-1} to 4000 cm^{-1}. Two pieces of KBr single crystals were used as a sample holder, between which a drop of sample was sandwiched. After loading the sample into the cryostat, it was first cooled rapidly (~ – 100 K min^{-1}) down to 200 K and then held at 250 K for 40 min to obtain the homogeneous crystalline phase.

5.2.4 DFT Calculation

In order to analyze the results of IR absorption measurements, quantum mechanical DFT computations were also made using the B3LYP method with 6-31G(d) basis set for all atoms. The calculations were carried out on single molecule of four 26DCTs ($C_6H_3Cl_2$-CH_3, $C_6H_3Cl_2$-CH_2D, $C_6H_3Cl_2$-CHD_2 and $C_6H_3Cl_2$-CD_3). At first the molecular geometries were optimized and then the vibrational frequencies as well as their relative intensities in IR absorptions spectra were calculated.

5.3 Results and Discussion

5.3.1 Heat Capacities

Fig. 5.3 shows the heat capacities of four 26DCTs ($C_6H_3Cl_2$-CH_3, $C_6H_3Cl_2$-CH_2D, $C_6H_3Cl_2$-CHD_2 and $C_6H_3Cl_2$-CD_3) over the whole temperature range. All the four compounds do not show any phase transitions. The small peak for $C_6H_3Cl_2$-CH_3, just below the fusion temperature, may be due to the eutectic mixtures. The fusion enthalpies and entropies determined are listed in Table 5.1.

At lower temperatures a broad anomaly was found for $C_6H_3Cl_2$-CH_2D and $C_6H_3Cl_2$-CHD_2 (Fig. 5.4). The excess contributions were calculated by subtracting the base heat capacities which were estimated by scaling the heat capacity of $C_6H_3Cl_2$-CH_3 against the temperature (Fig. 5.5). The excess heat capacities are fitted well by Schottky type functions (Section 3.2.3) with an energy scheme involving three levels with equivalent degeneracy, i.e. $g_1/g_0 = g_2/g_0 = 1$,

$$C_{\mathrm{Sch,m}}(\varepsilon_1, \varepsilon_2) = N \frac{\mathrm{d}}{\mathrm{d}T} \left(\frac{\varepsilon_1 \exp(-\varepsilon_1 / k_\mathrm{B}T) + \varepsilon_2 \exp(-\varepsilon_2 / k_\mathrm{B}T)}{\exp(-\varepsilon_1 / k_\mathrm{B}T) + \exp(-\varepsilon_2 / k_\mathrm{B}T)} \right), \qquad (5.1)$$

where N is the Avogadro number, k_B is the Boltzmann constant, ε_1 is the spacing between the ground and first excited level, ε_2 is that between ground and second excited level. The fitted functions are shown in Fig. 5.5 by solid curves, where ε_1 = 267 μeV and ε_2 = 2950 μeV for $C_6H_3Cl_2$-CH_2D and ε_1 = 2400 μeV and ε_2 = 2700 μeV for $C_6H_3Cl_2$-CHD_2, respectively. The excess entropies were calculated from the excess heat capacities, which are close to R ln 3 = 9.13 J K^{-1} mol^{-1} (Fig. 5.6). This is the quantity expected from the classical statistics, which derives from the different rotational symmetry number of the methyl groups; σ = 3 for -CH_3 and -CD_3, and σ = 1 for -CH_2D and -CHD_2 (Section 2.5).

As mentioned in Section 2.5, the symmetry number in the classical statistics corresponds to the symmetry restriction of the wave functions in the quantum mechanics. In the case of the rotational state of non-deuterated methyl groups, the symmetry number of σ = 3 corresponds to the transition between A and E states, which is allowed only when the nuclear spins convert. As a matter of course, the nuclear spin conversion is not considered in the classical statistics, so that the $A \leftrightarrow E$ transitions are "forbidden". In the case of partially deuterated methyl groups, the $A \leftrightarrow E$ transitions occur without changing the nuclear spin states. In other words, the $A \leftrightarrow E$ transitions become "allowed" by the partial deuteration, which corresponds to the symmetry number of σ = 1. The "allowed" $A \leftrightarrow E$ transitions may correspond to the excitations among the three levels observed in heat capacity for $C_6H_3Cl_2$-CH_2D or $C_6H_3Cl_2$-CHD_2. It is interesting that the spacing between the levels of -CH_2D or -CHD_2 (of the order of several meV) are much greater than that of the tunnel splitting of -CH_3 (1.56

μeV). Since the extent of overlapping of the wave functions never increases with mass, the large energy difference among the levels for $-CH_2D$ or $-CHD_2$ cannot be attributed to the tunnel splitting. Usually deuterium substitution dramatically decreases the extent of proton tunneling, so the ground torsional states of deuterated methyl groups can be regarded as localized wave functions, i.e. the pocket states. As mentioned in the theoretical chapter, the localization of the wave function is accompanied by the appearance of "orientation" in the classical regime. The three energy levels, obtained from the heat capacity measurement, are thus most likely to be the ground torsional levels of the methyl groups at the three different orientations. In this sense, the excess heat capacities are due to the orientational ordering of the methyl groups, which is the ordering of non-cooperative type showing a remarkable contrast to that of lithium acetate dihydrate (LiAc) and 4-methylpyridine (4MP). There still remains an important question to answer what kind of factor provides such a huge energy difference among the methyl groups with different orientations, which is the main subject of this thesis hereafter.

Incidentally the excess heat capacity of $C_6H_3Cl_2$-CHD_2 deviates from the Schottky function below c.a. 2 K (Fig. 5.5 inset), which seems proportional to temperature. This indicates that $C_6H_3Cl_2$-CHD_2 has additional low frequency modes distributing continuously. The microscopic origin of these excitations is not clarified yet.

Table 5.1 Thermodynamic quantities associated with fusion of 2,6-dichlorotoluene and its methyl-deuterated analogs. The last column shows the purity of the samples determined by fractional melting method.

Compound	T_{fus}	$\Delta_{fus}H$	$\Delta_{fus}S$	purity
	K	kJ mol^{-1}	J K^{-1} mol^{-1}	%
$C_6H_3Cl_2$-CH_3	275.82	13.06	47.81	99.48
$C_6H_3Cl_2$-CH_2D	275.48	12.94	47.32	99.71
$C_6H_3Cl_2$-CHD_2	275.22	12.76	47.03	98.70
$C_6H_3Cl_2$-CD_3	275.08	12.98	47.78	99.12

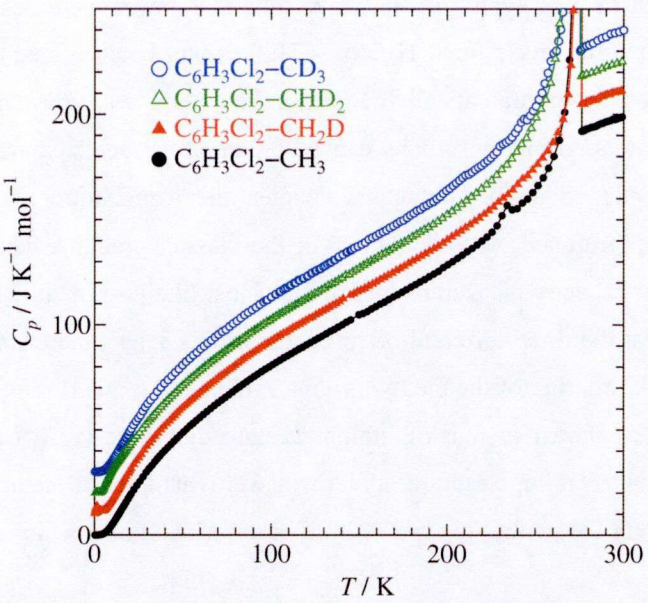

Fig. 5.3 Molar heat capacity of 2,6-dichlorotoluene and its methyl-deuterated analogs. The ordinate is for $C_6H_3Cl_2$-CH_3. The results for other three compounds are successively shifted upward by 10 J K^{-1} mol^{-1}.

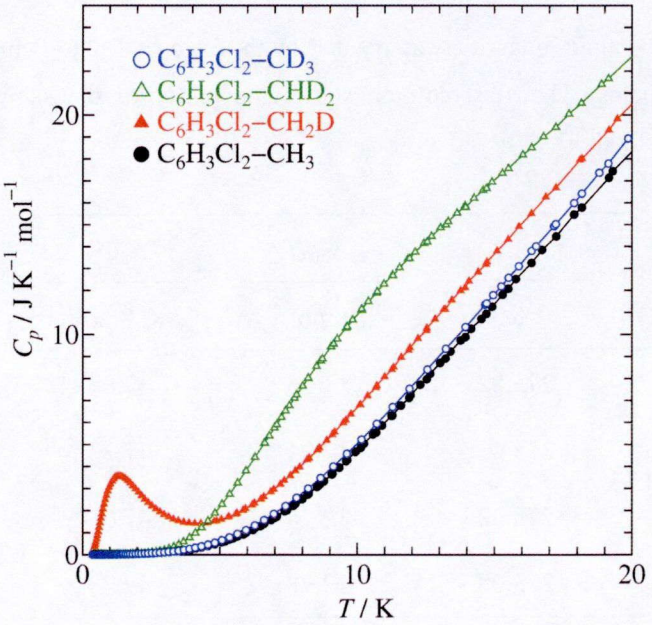

Fig. 5.4 Molar heat capacity of 2,6-dichlorotoluene and its methyl-deuterated analogs below 20 K.

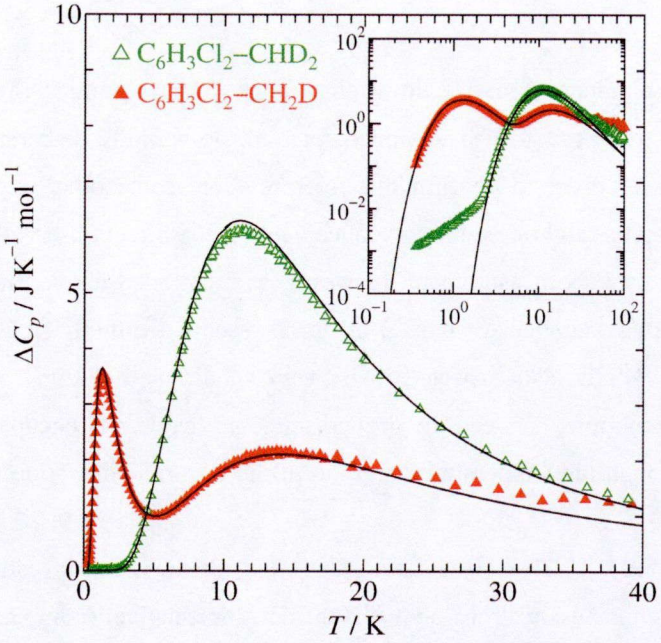

Fig. 5.5 Excess heat capacity of $C_6H_3Cl_2$-CH_2D and $C_6H_3Cl_2$-CHD_2. The inset shows the double logarithmic plot. The solid curves show the Schottky functions with three levels spaced from the ground level by 267 μeV and 2950 μeV for $C_6H_3Cl_2$-CH_2D and 2400 μeV and 2700 μeV for $C_6H_3Cl_2$-CHD_2.

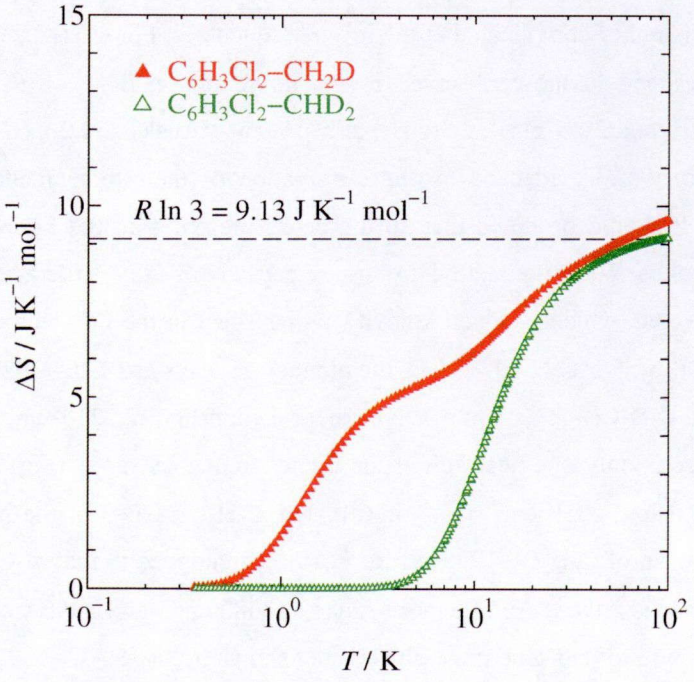

Fig. 5.6 Excess entropy of $C_6H_3Cl_2$-CH_2D and $C_6H_3Cl_2$-CHD_2.

5.3.2 IR Spectra

The three levels obtained from the low temperature heat capacities of $C_6H_3Cl_2$-CH_2D and $C_6H_3Cl_2$-CHD_2 seem to be the ground torsional states of the partially deuterated methyl groups in different orientations. In order to confirm this interpretation, some other experimental evidences were required. The most straightforward way conceivable is the direct observation of the excitations between those levels by INS measurement. However, as mentioned above, the overlapping of the wave functions in the pocket states of -CH_2D or -CHD_2 seems negligibly small for 26DCT, so that the cross section of INS is also expected to be very small. In this study, instead of the direct observation of the excitations between the ground torsional levels, the occupancies of these levels were investigated through the temperature variation of the infrared absorption peaks for C-H (C-D) stretching modes.

The IR spectrum for $C_6H_3Cl_2$-CH_3 in liquid phase has already been investigated by Green *et al* [5]. According to them, the spectrum above 2000 cm^{-1} is relatively simple; there are two C-H stretching modes of benzene ring at 3075 cm^{-1} and 3063 cm^{-1}, three C-H stretching modes of methyl groups ($\nu_s(CH_3)$ at 2927 cm^{-1} (non-degenerated) and $\nu_{as}(CH_3)$ at 2950 cm^{-1} (doubly degenerated)), and weak overtones of bending modes of methyl groups ($2\delta_s(CH_3)$ and $2\delta_{as}(CH_3)$ at 2859 cm^{-1} and 2740 cm^{-1}, respectively).

Fig. 5.7 shows the IR spectra of four compounds in two ranges of frequency ((a) 2100 – 2280 cm^{-1} and (b) 2830 – 3020 cm^{-1}) at 6 K. The discussion here is limited to above 2100 cm^{-1} since the structure of spectra is rather complicated at the lower frequencies. For $C_6H_3Cl_2$-CH_3, the four peaks in Fig. 5.7(b) correspond to those observed in the liquid phase, that is $\nu_s(CH_3)$ at 2957 cm^{-1}, $\nu_{as}(CH_3)$ at 3001 cm^{-1} and 2971 cm^{-1}, $2\delta_s(CH_3)$ at 2915 cm^{-1} (weak) and $2\delta_{as}(CH_3)$ and 2894 cm^{-1}. The last two overtones are evidenced by the observation of their fundamental tones of $\delta(CH_3)$ around 1450 cm^{-1}. It should be noted that all the peaks presented in the figure are related to the motion of methyl groups. When the methyl groups are partially or fully deuterated, those frequencies are significantly lowered, which is a well known isotope effect in the IR spectra and often used for the mode assignment [6]. For $C_6H_3Cl_2$-CH_2D, the number of peaks at 2830 – 3020 cm^{-1} (Fig. 5.7(b)) is less than that of $C_6H_3Cl_2$-CH_3, while a double peak appears at 2210 cm^{-1} (Fig. 5.7(a)). For $C_6H_3Cl_2$-CHD_2, there is only one peak left at the higher frequency range (Fig. 5.6(b)) while many peaks are observed below 2250 cm^{-1} (Fig. 5.7(a)). For $C_6H_3Cl_2$-CD_3, all the peaks in Fig. 5.7(b) disappear. The spectrum of $C_6H_3Cl_2$-CD_3 in Fig. 5.7(a) is analogous to that of $C_6H_3Cl_2$-CH_3 in Fig. 5.7(b). For all compounds, there are two more peaks at 3082 cm^{-1} and 3066 cm^{-1} corresponding to the C-H stretching modes of benzene ring, which is not shown in Fig. 5.7.

Fig. 5.8 shows the IR spectra of 26DCT and its methyl deuterated analogs obtained by the DFT calculation for single molecule. Since only the normal modes are given, five peaks are visible; the

two peaks at the highest frequency correspond to the C-H stretching of the benzene ring and the other three peaks are the C-H or C-D stretching modes of methyl groups. Compared to the experimental spectra (Fig. 5.7), the absolute values of the frequencies are systematically shifted upward. However the qualitative feature of the experimental and calculated spectra is in good agreement with each other.

The main focus here is on the temperature variation of the spectrum intensities. Fig. 5.9 shows the temperature evolution of the IR spectra for $C_6H_3Cl_2$-CH_2D at 2100 – 2250 cm^{-1}. It is clearly visible that four peaks change in intensity with temperature. The two peaks at 2140 cm^{-1} and 2190 cm^{-1} diminish with decreasing temperature, while the double peak at 2210 cm^{-1} becomes stronger. The intensity of each peak was integrated and scaled with arbitral factor (Fig. 5.10). The scaled intensities agree quite well with the occupancy curve of three energy levels obtained from the heat capacity measurement. The similar tendencies are also observed for the other peaks associated with methyl groups. These results can be interpreted in such a way that the different stretching peaks correspond to the different orientations of the methyl groups, and the intensities of the peaks change with decreasing temperature due to their orientational ordering. It is interesting to note that two peaks observed at 2140 cm^{-1} and 2190 cm^{-1} correspond to the highest energy level (Fig. 5.10). There may be two or more number of non-equivalent methyl groups in the crystal.

The angle dependence of the vibrational frequency is mainly due to the variation of the normal modes with the internal angle α, i.e. the variation of the diagonal elements in the matrix of molecular motion. If the normal modes of intramolecular vibrations depend little on the intermolecular interactions, quantum mechanical calculations for the single molecule qualitatively provide an insight into the angle dependence of the normal modes. Fig. 5.11 shows the angle (α) dependence of the frequencies of the C-D stretching mode for -CH_2D obtained by DFT calculation. The calculation was carried out using the same computational setup described before. Since 2,6-dichlorobenzene is two-fold symmetric to the rotational axis of C-C bond, it is enough to investigate the angle dependence from $\alpha = 0$ to $\pi/3$ (= 60°) for three orientations. The orientation that D or H atom is on the same plane of the frame is taken to be zero degree. Comparing these computational results with the experimental spectra, the orientations of the methyl groups can be derived.

As shown in Fig. 5.9, the absorption bands of the lowest energy level (2212 cm^{-1}) and that of the middle level (2208 cm^{-1}) are similar in frequency, while the band frequency of the highest level (2140 cm^{-1} or 2190 cm^{-1}) is significantly lower than the other two levels. In short, two orientations have similar frequency in C-D stretching mode and the other orientation has lower frequency. Considering simply the relative position of the peaks, the experimental spectra correspond to the situation of $\alpha = 30°$ in Fig. 5.11, where one of the hydrogen atom points out almost perpendicularly from the molecular plane.

Interestingly the molecular configuration of 26DCT optimized by the DFT calculation for single

molecule is that one proton of the methyl group is on the molecular plane. The results of the calculation are the same for the deuterated 26DCTs because the nuclear mass has nothing to do with the atomic interactions. The different results between the experiment and calculation may be due to the intermolecular interactions, that is, the orientation of the methyl groups may be twisted by the intermolecular interaction in the crystal.

Fig. 5.12 shows the temperature evolution of the IR spectra for $C_6H_3Cl_2$-CHD_2 at 2890 – 3000 cm^{-1}. The two peaks at 2970 cm^{-1} and 2977 cm^{-1} get weaker with decreasing temperature, while the peak at 2910 cm^{-1} gets stronger. The peak intensities are integrated and scaled with an arbitral factor (Fig. 5.13). The scaled intensities of first two peaks (2970 cm^{-1} and 2977 cm^{-1}) agree quite well with the occupancies of the two upper levels obtained from the heat capacity measurement. The intensity of the peak at 2910 cm^{-1}, however, cannot be scaled to either occupancy curves. This may be because the peak consists of more than two components. The dashed curve in Fig. 5.13 shows the occupancy of the lowest energy level plus that of the highest level multiplied by 0.65, which fits well to the scaled intensity of the peak at 2910 cm^{-1} at low temperatures. If one considers that the main component of the peak at 2910 cm^{-1} corresponds to the lowest energy level and the other two peaks corresponds to the higher two energy levels, then it is possible to carry out the same discussion to that of $C_6H_3Cl_2$-CH_2D. Fig. 5.14 shows the frequency of C-D stretching mode in -CH_2D depending on the orientation of the methyl groups obtained from the quantum calculation of single molecule. Following the same logic applied to $C_6H_3Cl_2$-CH_2D, the most stable orientation was determined to be that one proton is pointing out almost perpendicularly from the plane of dichlorobenzene frame. This result is in good agreement with that of $C_6H_3Cl_2$-CH_2D.

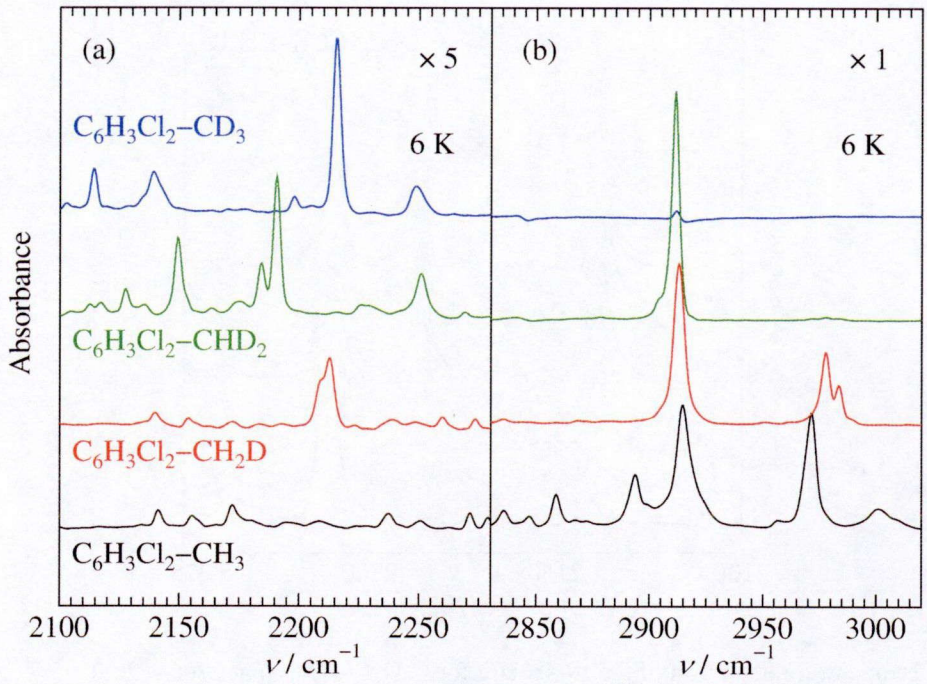

Fig. 5.7 Infrared absorption spectra obtained at 6 K for 2,6-dichlorotoluene and its methyl-deuterated analogs; (a) from 2100 cm^{-1} to 2280 cm^{-1}, (b) from 2830 cm^{-1} to 3020 cm^{-1}.

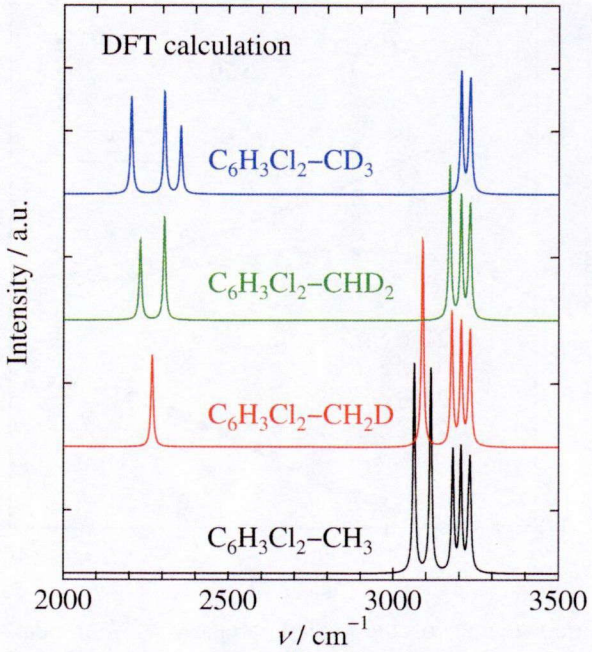

Fig. 5.8 Infrared absorption spectra obtained by DFT calculation for 2,6-dichlorotoluene and its methyl-deuterated analogs.

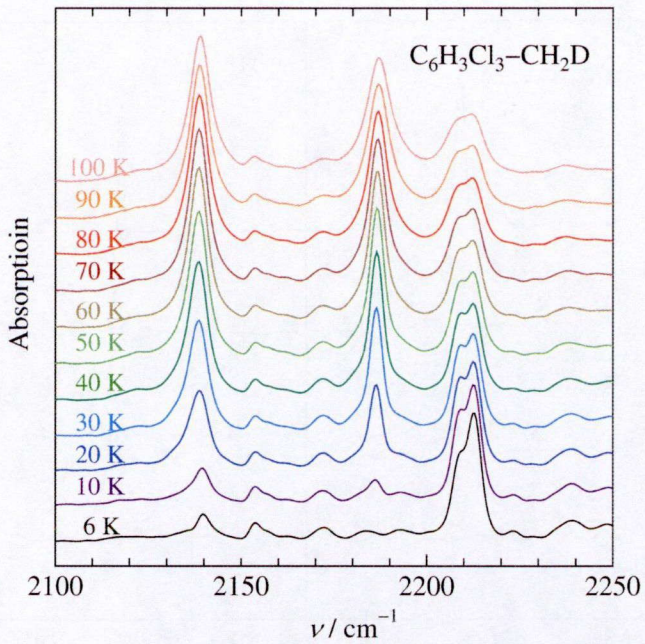

Fig. 5.9 Temperature evolution of the IR spectra for $C_6H_3Cl_2$-CH_2D at 2100 – 2250 cm^{-1}.

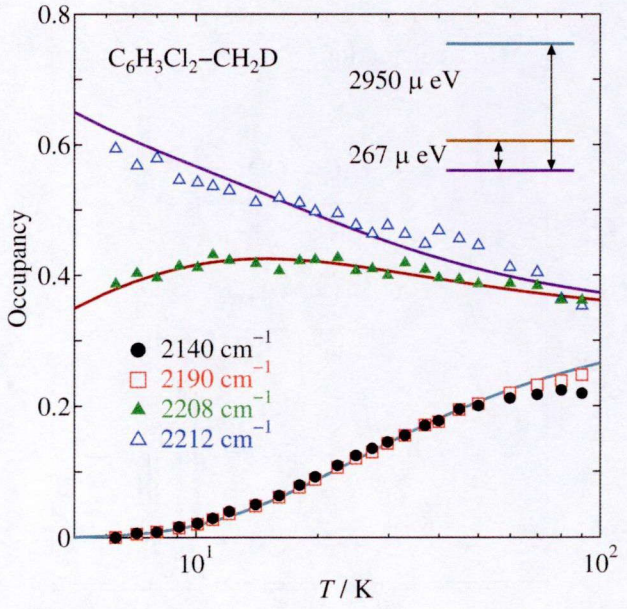

Fig. 5.10 Temperature dependence of the scaled intensity of four peaks connected with C-D stretching mode of -CH_2D obtained for $C_6H_3Cl_2$-CH_2D (see Fig.5.9), which are consistent with the occupancy for the three-level energy scheme obtained from the Schottky heat capacity (solid curves).

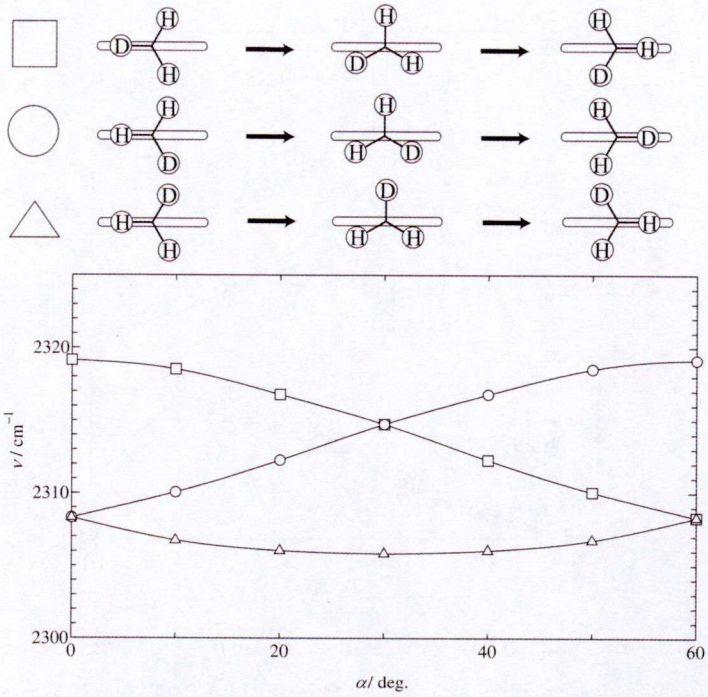

Fig. 5.11 Frequency of C-D stretching mode in -CH_2D for $C_6H_3Cl_2$-CH_2D as a function of internal rotational angle α obtained by DFT calculation for single molecule. The pictures above the figure show the orientations of the methyl groups projected parallel to the 2,6-dichlorobenzen frame.

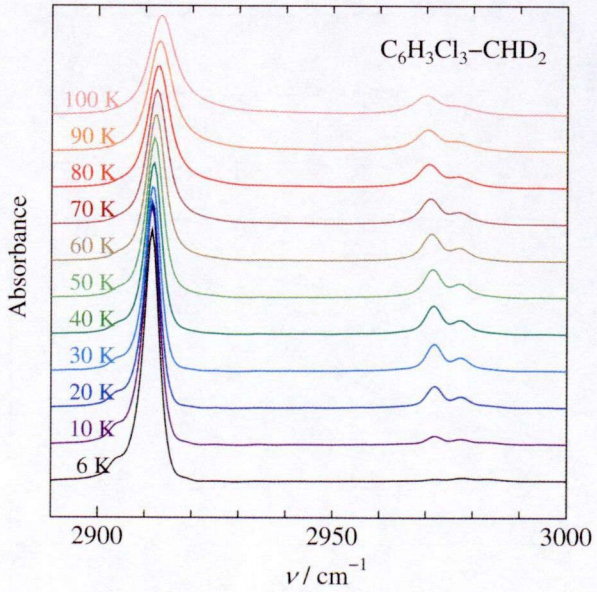

Fig. 5.12 Temperature evolution of the IR spectra for $C_6H_3Cl_2$-CHD_2 at 2890 – 3000 cm^{-1}.

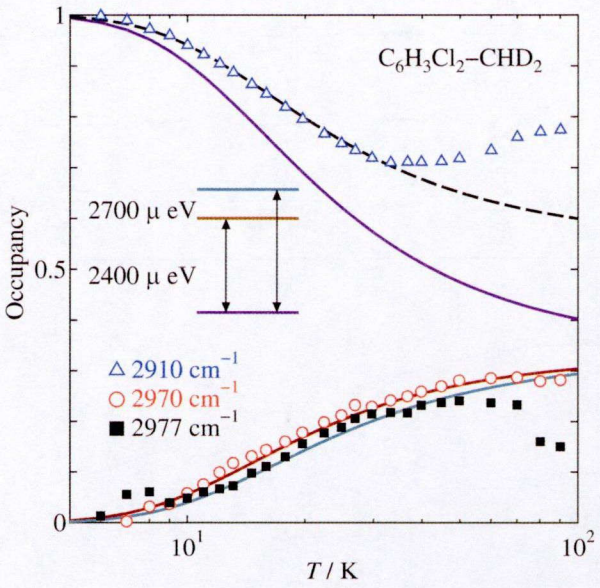

Fig. 5.13 Temperature dependence of the scaled intensity of three peaks obtained for $C_6H_3Cl_2$-CHD_2 (see Fig. 5.12). The data of 2970 cm^{-1} and 2977 cm^{-1} agree well with the occupancy for the three-level energy scheme obtained from the Schottky heat capacity (solid curves). The dashed curve shows the occupancy of the lowest energy level plus that of the highest level factored by 0.65, which fits well to the scaled intensity of the peak at 2910 cm^{-1}.

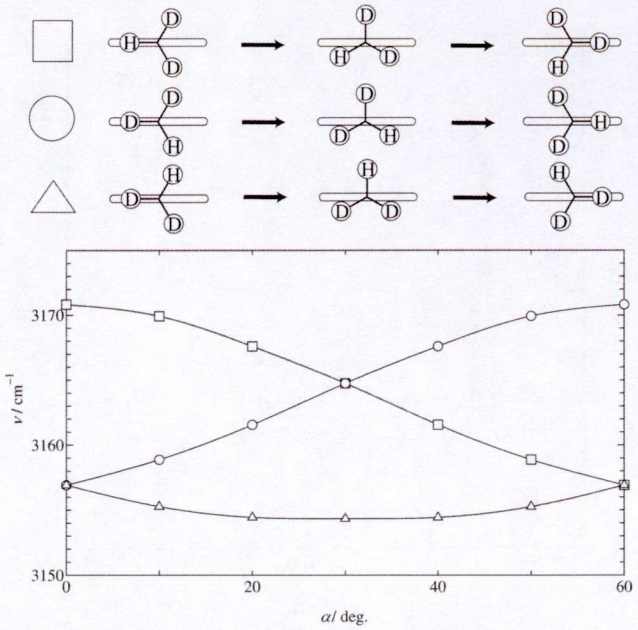

Fig. 5.14 Frequency of C-H stretching mode in -CHD_2 for $C_6H_3Cl_2$-CHD_2 as a function of internal rotational angle α obtained by DFT calculation for single molecule. The pictures above the figure show the orientations of the methyl groups projected parallel to the 2,6-dichlorobenzen frame.

5.4 Summary

Heat capacity measurements were made for 2,6-dichlorotoluene ($C_6H_3Cl_2$-CH_3) and its methyl-deuterated analogs, $C_6H_3Cl_2$-CH_2D, $C_6H_3Cl_2$-CHD_2, $C_6H_3Cl_2$-CD_3, between 0.35 K and 300 K by adiabatic calorimetry and relaxation calorimetry. A Schottky type anomaly was found for the two partially deuterated analogs, $C_6H_3Cl_2$-CH_2D and $C_6H_3Cl_2$-CHD_2, below 40 K. It is explained by an energy scheme involving three levels, $g_1/g_0 = g_2/g_0 = 1$. The spacing from the ground state is 267 μeV and 2950 μeV for $C_6H_3Cl_2$-CH_2D and 2400 μeV and 2700 μeV for $C_6H_3Cl_2$-CHD_2, respectively. The excess entropy amounts to R ln 3 (= 9.13 J K^{-1} mol^{-1}) which is due to the symmetry breaking of methyl group by partial deuteration.

Infrared absorption measurements were also made between 6 K and 100 K in the range from 400 cm^{-1} to 4000 cm^{-1} for the four compounds ($C_6H_3Cl_2$-CH_3, $C_6H_3Cl_2$-CH_2D, $C_6H_3Cl_2$-CHD_2 and $C_6H_3Cl_2$-CD_3). For $C_6H_3Cl_2$-CH_2D, four peaks associated with stretching modes of -CH_2D were detected in the range from 2100 cm^{-1} to 2250 cm^{-1}. The two peaks at 2140 cm^{-1} and 2190 cm^{-1} diminish with decreasing temperature, while the other two peaks around 2210 cm^{-1} become stronger. For $C_6H_3Cl_2$-CHD_2, three peaks were detected in the range from 2890 cm^{-1} to 3000 cm^{-1}, which were associated with stretching modes of -CHD_2. The two peaks at 2970 cm^{-1} and 2977 cm^{-1} diminish with decreasing temperature, while the other peaks at 2910 cm^{-1} become stronger. For bith compounds, the temperature dependences of the intensities of those peaks were explained successfully by the three-level energy scheme obtained from the Schottky heat capacity.

The angle dependence of the absorption frequency was estimated from the DFT calculation of the single molecule. Comparing the experimental IR spectra with the calculated frequencies, possible orientations of the methyl groups were determined. According to this result, the partially deuterated methyl groups are oriented in the crystal so that all the hydrogen atoms are pointing out of the molecular plane. For $C_6H_3Cl_2$-CH_2D, the most stable orientation is that one of the two protons is pointing almost perpendicular from the molecular plane. For $C_6H_3Cl_2$-CHD_2, the most stable orientation is that one of the two deuterons is pointing almost perpendicular from the molecular plane.

According to the quantum mechanical calculation for the single molecule of 26DCT, the most stable orientation is that one of the hydrogen atoms is in the molecular plane. The results obtained in the present study strongly indicate that the orientation of the methyl groups is twisted by the intermolecular interactions in crystal.

5.5 References of Chapter 5

[1] A. Boudjada, J. Meinnel, A. Boucekkine, O. J. Hernandez and M. T. Fernández-Diaz, *J. Chem. Phys.* **117** (2002) 22.

[2] J. Meinnel, W. Häusler, M. Mani, M. Tazi, M. Nusimovici, M. Sanquer, B. Wyncke, A. Heidemann, C. J. Carlile, J. Tomkinson and B. Hennion, *Physica B* **180** (1992) 711.

[3] J. Meinnel, H. Grimm, O. Hernandez and E. Jansen, *Physica B* **350** (2004) e459.

[4] M. Prager and A. Heidemann, *Chem. Rev.* **97** (1997) 2933.

[5] J.H.S. Green, D.J. Harrison and W. Kynaston, *Spectrochim. Acta* **27A** (1971) 793.

[6] J.M. Hollas, *Modern Spectroscopy* (John Wiley & Sons Ltd. 1987).

Chapter 6

Orientational Ordering of Partially Deuterated Methyl Groups in Solid 2,6-Dibromotoluene

6.1 Introduction

As mentioned in the Introduction in Chapter 5, the halogen size effect on the rotational dynamics of the methyl groups for trihalogenomesitylenes (THMs) is interesting because the bulky halogen atoms control the rotational potential of the methyl groups [1-3]. Similar effect is expected for 2,6-dihalogenotoluenes (26DHTs). After the important discoveries for 2,6-dichlorotoluene (26DCT) that the orientation of the partially deuterated methyl groups are ordered at low temperature in a non-cooperative manner, the deuteration effect on the methyl groups for 2,6-dibromotoluene (26DBT) was investigated. In this chapter, the results of heat capacity measurements as well as IR absorption measurements for 26DBT and its methyl-deuterated analogs are described.

Since bromine (Br) is larger in size than chlorine (Cl), several effects of halogen substitution can be expected for the rotational dynamics of methyl groups. In view of the intramolecular interactions, the methyl rotation seems to be more hindered by bromine substitution, simply because of the greater exclusive volume of the halogens. The effect to the intermolecular interaction, on the other hand, is not straightforward. If the basic crystal structure does not change with halogen substitution, the enlargement of the halogen size may extend the intermolecular distance, which eventually reduces the rotational potential of the methyl groups. If the crystal structure dramatically changes with halogen substitution, the surroundings of the methyl groups may also change drastically, so that the effect to the rotational dynamics is not certain.

The crystal structure of 26DBT has not been clarified. The tunnel excitation of the protonated 26DBT is reported to be 4.0 μeV at 43 K [4], which is slightly larger than 26DCT, indicating that the larger size of halogen may lower the hindering barrier of the rotor.

6.2 Experimental

6.2.1 Samples

The four 26DBTs ($C_6H_3Br_2$-CH_3, $C_6H_3Br_2$-CH_2D, $C_6H_3Br_2$-CHD_2 and $C_6H_3Br_2$-CD_3) were synthesized at Laboratory for Biomolecular Chemistry in Osaka University. The deuteration degrees were examined by NMR measurement, which were 98%D for $C_6H_3Br_2$-CH_2D, 98%D for $C_6H_3Br_2$-CHD_2 and 100%D for $C_6H_3Br_2$-CD_3, respectively. ^{1}H NMR (500 HMz, $CDCl_3$) δ 7.48 (2H at the *meta* positions of 2,6-dibrmobenzene), 6.88 (1H at the *para* position of 2,6-dibromobenzene), 2.55 (protons of the methyl groups). The deuteration degrees were estimated by taking the ratio of the peak integrals at δ 6.88 and δ 2.55. The chemical purities of the four samples were determined using the fractional melting method (Section 3.2.1), which were 97.14% for $C_6H_3Br_2$-CH_3, 95.70% for $C_6H_3Br_2$-CH_2D, 97.71% for $C_6H_3Br_2$-CHD_2 and 95.91% for $C_6H_3Br_2$-CD_3 respectively. Although the purities were not high enough, no further purification was made because of the limited sample amount. On determining the chemical purities, the $1/f$ plots were not straight line, so the Mastrngelo's equation (Eq. (3.14)) was applied involving the adjustable parameter α. The purities and the values of parameter α are listed in Table 6.1. In addition to these samples, another purer sample of $C_6H_3Br_2$-CH_2D was also prepared, which was, however, limited in amount (< 0.3 g), so the adiabatic calorimetry was not carried out on it. The deuteration degree and the chemical purity of this sample were 98%D and 98%, respectively, determined by NMR measurement.

6.2.2 Heat Capacity Measurement

Heat capacity measurements were made by adiabatic calorimetry between 5 K and 300 K and relaxation calorimetry between 0.35 K and 40 K. The amounts of samples used for the adiabatic calorimetry were 0.6742995 g (2.697978 mmol), 0.705967 g (2.81334 mmol), 0.53502 g (2.1123 mmol) and 1.01082 g (3.9961 mmol) for $C_6H_3Br_2$-CH_3, $C_6H_3Br_2$-CH_2D, $C_6H_3Br_2$-CHD_2 and $C_6H_3Br_2$-CD_3, respectively, after buoyancy correction.

The amounts of the samples used for the relaxation calorimetry were 0.934 mg (3.74 μmol), 0.71 mg (2.83 μmol), 1.08 mg (4.29 μmol) and 0.838 mg (3.31 μmol) for $C_6H_3Br_2$-CH_3, $C_6H_3Br_2$-CH_2D, $C_6H_3Br_2$-CHD_2 and $C_6H_3Br_2$-CD_3, respectively. The copper liquid sample cells (Section 3.1.5, Case 2) were used. The sample amounts were determined referring the heat capacities of adiabatic calorimetry. The sample amount of purer $C_6H_3Br_2$-CH_2D was 0.805 mg (3.21 μmol), which was determined by referring the heat capacity value of less purer sample at 40 K where the impurity presumably does not affect the absolute value of the heat capacity.

The heat capacity data of $C_6H_3Br_2$-CH_2D in this chapter are those of less pure sample unless

otherwise noted. As a matter of fact, the impurity does not significantly alter the low temperature heat capacities, which will be shown later.

6.2.3 IR Measurement

Infrared absorption measurements were made between 6 K and 100 K in the range from 400 cm^{-1} to 4000 cm^{-1}. Two pieces of KBr single crystals were used as a sample holder. After loading the sample into the cryostat, it was first cooled rapidly (~ −100 K min^{-1}) down to 200 K and then held at 250 K for 40 min to obtain the homogeneous stable crystalline phase. For $C_6H_3Br_2$-CH_2D, only the purer sample was measured.

6.2.4 DFT Calculation

In order to support the interpretation of the IR spectra, quantum mechanical DFT computations were also made using the B3LYP method with 6-31G(d) basis set for all atoms. The calculations were made on single molecule of four 26DBTs. At first the molecular geometries were optimized and then the vibrational frequencies as well as their relative intensities in IR absorptions spectra were calculated.

6.3 Results and Discussion

6.3.1 Heat Capacities

All the four 26DBTs do not undergo phase transitions, but several small exothermic behaviors as well as a small hump in heat capacity were detected above 150 K. Fig. 6.1 shows the (a) heat capacities and (b) temperature drift rates of $C_6H_3Br_2$-CD_3 above 100 K as a representative example. The sample rapidly cooled down (~ −7 K min^{-1}) from the room temperature shows small exothermic behaviors at 200 K and 234 K, while the sample annealed at 234 K for 4.5 h shows no such anomalies. The negative values of the drift rate around 280 K is due to the fusion. Heat capacities of two (rapidly cooled and annealed) phases are similar, both showing a small hump at 160 K even though no anomalous behavior is observed in the drift rate at this temperature. These behaviors are common for all the four samples. Although the exothermic behavior must be associated with some stabilization (from a metastable to a stable state), heat capacities of two states are similar at low temperatures. The rapidly cooled sample may contain very small portion of the metastable phase which stabilized at 234 K. In this chapter, heat capacity of the annealed phase is only described

unless otherwise noted. The origin of the hump in heat capacity at 160 K is not clarified yet. Since the drift rate at this temperature looks natural, it can not be attributed to a glass transition. It may be due to some motion of impurities. The thermodynamic quantities associated with the fusion are listed in Table 6.1.

At low temperatures a broad anomaly was found for $C_6H_3Br_2$-CH_2D and $C_6H_3Br_2$-CHD_2 (Fig. 6.2) as it was for the partially methyl-deuterated 26DCTs. Fig. 6.3 and Fig. 6.4 show the excess contributions in heat capacity and entropy respectively. On estimating the lattice heat capacities of these two compounds, the simple scaling of the heat capacity of $C_6H_3Br_2$-CH_3 against temperature was not successful unlike in the case of 26DCT, which may be because the significant contribution of the intramolecular vibrations to the total heat capacity cannot be scaled by the same factor of phonon heat capacities. Alternatively, the intramolecular contributions were subtracted first from the total heat capacity and then the temperature scaling was carried out. The heat capacities of intramolecular vibration were estimated by Einstein model using the frequencies obtained by the quantum mechanical computation. The excess entropies of both compounds (Fig. 6.4) are close to R ln 3 indicating that the excess contribution is due to the orientational ordering of the methyl groups. The excess heat capacity of $C_6H_3Br_2$-CH_2D is fitted well by a Schottky-type function with three levels (Fig. 6.3). The levels are spaced from the ground level by 1200 μeV and 1700 μeV. For $C_6H_3Br_2$-CHD_2, on the other hand, the fitting by a Schottky function with three levels is not quite, where the experimental curve is significantly broader than that of the Schottky model. Fig. 6.3 shows the result of the best fit, in which the energy levels are spaced by 240 μeV and 1700 μeV. The broadening behavior indicates some distribution in energy levels. It is likely that there are many kinds of potentials hindering the rotation of the methyl groups, which is possible if the orientation of the whole molecule is disordered. However no evidence of glass transition due to the freezing of the orientational ordering has been found yet.

It is important to note that the energy spacing between the highest and the lowest levels are almost the same for $C_6H_3Br_2$-CH_2D and $C_6H_3Br_2$-CHD_2. In addition, the spacing between the middle and the lowest level for $C_6H_3Br_2$-CH_2D is almost equal to the spacing between the middle and the highest levels for $C_6H_3Br_2$-CHD_2. In other word, the energy scheme of $C_6H_3Br_2$-CH_2D is similar to the inversed scheme of $C_6H_3Br_2$-CHD_2. This relation was also found for 26DCTs, which may be a universal feature of partially deuterated methyl groups.

The remarkable difference between the results of 26DCT and 26DBT for the same -CH_2D (-CHD_2) compound is the ratio of energy spacing. For example, the two higher energy levels of $C_6H_3Cl_2$-CH_2D are close to each other while the two lower levels are close for $C_6H_3Br_2$-CH_2D. It means that the methyl groups in two systems are located in the different potential fields presumably because of the different crystal structures and/or different orientations of the methyl groups.

The inset of Fig. 6.3 shows the excess heat capacities in a double logarithmic plot. The excess

heat capacity of $C_6H_3Br_2$-CH_2D deviates from the Schottky function below 2 K, which is similar to the results of $C_6H_3Cl_2$-CHD_2.

Effect of impurities to the excess heat capacity was also investigated for $C_6H_3Br_2$-CH_2D using two samples with different purities, 95.7% and 98% (see Table 6.1). Fig. 6.5 shows the low temperature heat capacities of two samples, in which the two heat capacities do not differ significantly. The purer one has slightly larger heat capacity than the impure sample, which may be due to the difference in the lattice heat capacity. The shape of excess heat capacity depends little on the impurity.

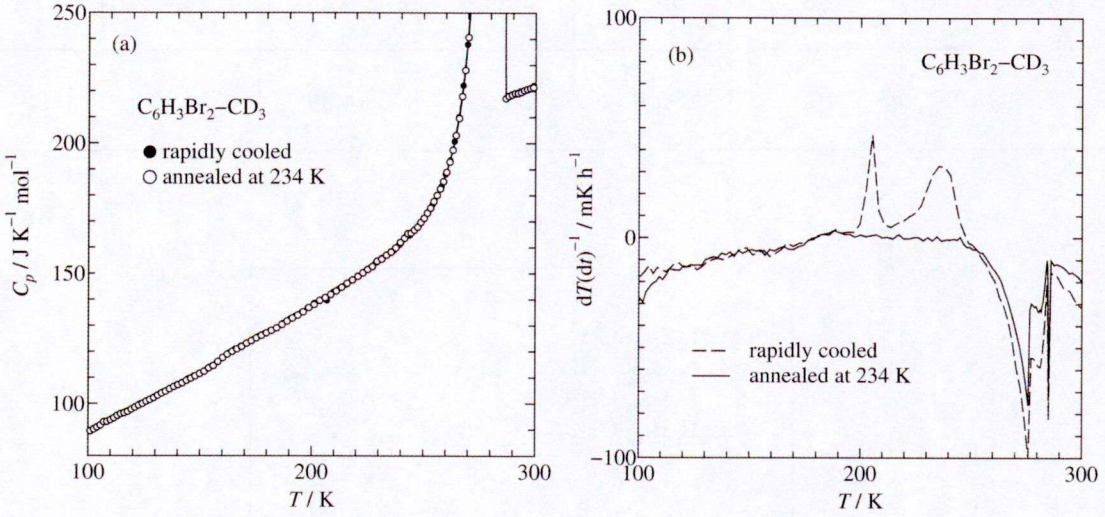

Fig. 6.1 (a) Molar heat capacities and (b) temperature drift rates of $C_6H_3Br_2$-CD_3 above 100 K.

Table 6.1 Thermodynamic quantities associated with fusion of 2,6-dibromotoluene and its methyl-deuterated analogs.

Sample	deuteration	purity	T_{fus}	$\Delta_{fus}H$	$\Delta_{fus}S$	α
	%D	%	K	kJ mol^{-1}	J K^{-1} mol^{-1}	
$C_6H_3Br_2$-CH_3	-	97.14	286.94	14.27	50.37	0.06
$C_6H_3Br_2$-CH_2D	98	95.7	286.67	14.71	52.53	0.05
$C_6H_3Br_2$-CHD_2	98	97.71	286.99	14.88	52.42	0.05
$C_6H_3Br_2$-CD_3	100	95.91	286.63	14.39	51.13	0.09

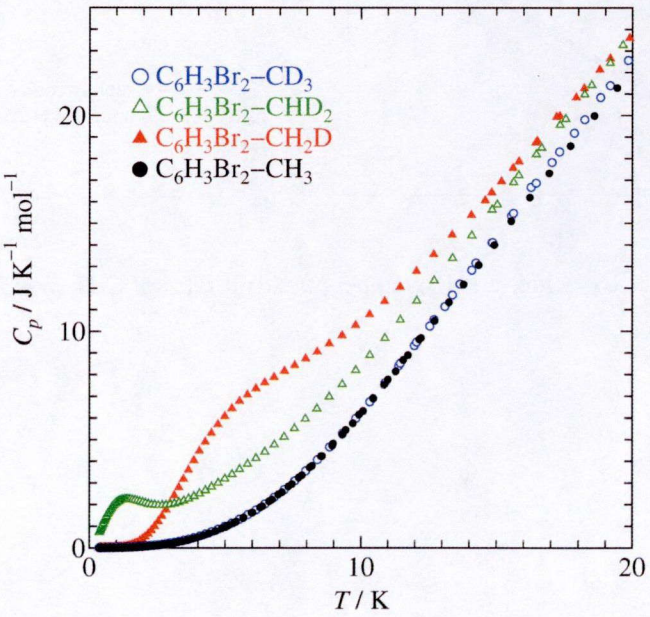

Fig. 6.2 Molar heat capacity of 2,6-dibromotoluene and its methyl-deuterated analogs below 20 K.

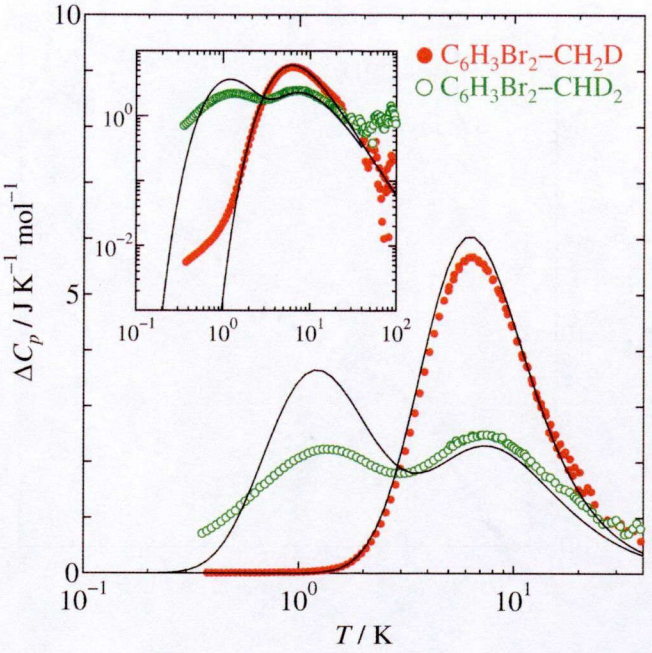

Fig. 6.3 Excess heat capacity of $C_6H_3Br_2$-CH_2D and $C_6H_3Br_2$-CHD_2. The inset shows the double logarithmic plot. The solid curves show the Schottky functions with three levels spaced from the ground level by 1200 μeV and 1700 μeV for $C_6H_3Br_2$-CH_2D and 240 μeV and 1700 μeV for $C_6H_3Br_2$-CHD_2, respectively.

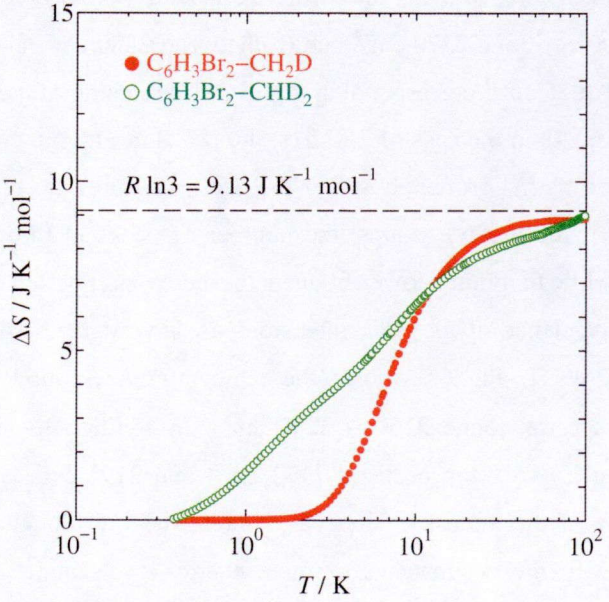

Fig. 6.4 Excess entropies of $C_6H_3Br_2$-CH_2D and $C_6H_3Br_2$-CHD_2.

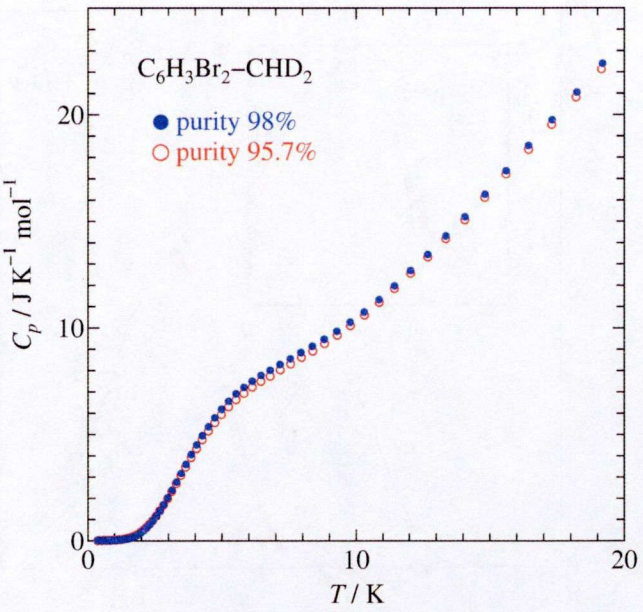

Fig. 6.5 Low temperature heat capacities of $C_6H_3Br_2$-CH_2D with different sample purities.

6.3.2 IR Measurement

The structures of IR spectra of 26DBTs are quite similar to those of 26DCTs because of their similarity in molecular structure. Fig. 6.6 shows the IR spectra of four compounds in two spectral ranges: (a) between 2100 cm^{-1} and 2270 cm^{-1} and (b) between 2880 cm^{-1} and 3025 cm^{-1}. There are three more peaks above 3025 cm^{-1} corresponding to the C-H stretching of the benzene ring, which is not shown in the Fig. 6.6. As in the case of 26DCTs, the peaks in Fig. 6.6 correspond to the C-H or C-D stretching modes of methyl groups, however the peak structures are rather complex. With the successive deuteration of the methyl groups, the number of peaks in the higher frequency range decreases (Fig.6.6 (b)) while that in the lower frequencies increases (Fig. 6.6 (a)).

The temperature dependence of the peak intensities are investigated using the same analytical procedure applied to 26DCT. Fig. 6.7 shows the temperature evolution of the IR spectra for $C_6H_3Br_2$-CH_2D in the spectral range 2160 – 2250 cm^{-1}. In addition to the two strong peaks at 2212 cm^{-1} and 2224 cm^{-1}, two weak peaks at 2173 cm^{-1} and 2191 cm^{-1} also show a remarkable temperature dependence of the intensity. The scaled intensities are plotted against temperature in Fig. 6.8, which agree with the occupancies of three energy levels under Boltzmann distribution spaced by 1200 μeV and 1700 μeV from the ground level. The spacing was obtained from the Schottky heat capacity. Similar temperature dependences are also observed for the C-H stretching peaks at high frequencies (~ 2950 cm^{-1}). Fig. 6.9 shows the temperature dependence of spectra for $C_6H_3Br_2$-CHD_2 in the spectral range 2900 – 3000 cm^{-1}. Intensities of the peaks at 2930 cm^{-1},

2945 cm^{-1}, 2981 cm^{-1} and 2994 cm^{-1} (very weak) show a strong temperature dependence. Their scaled intensities are plotted against temperature in Fig. 6.10 where the peak at 2930 cm^{-1} is decomposed into two parts by curve fitting. It is interesting that all of the five peaks can be scaled on the occupancy curves of three levels spaced by 240 μeV and 1700 μeV from the ground state, even though this three-level scheme fails to reproduce the excess heat capacity of $C_6H_3Br_2$-CHD_2 (Fig. 6.3). This unexpectedly good agreement may be because the IR peaks represent the averaged sum of the vibrational excitations of methyl groups, of which the orientations as well as the energy levels are centrally-distributed around some position, or because the orientational distribution has sufficiently small contribution to the peak intensities and vanished by the scaling process.

Fig. 6.11 shows the angle dependence of the frequency of C-D stretching in $C_6H_3Br_2$-CH_2D obtained by DFT calculation for single molecule. The result is comparable with that of $C_6H_3Cl_2$-CH_2D (Fig. 5.10) because of the similarity in molecular structure. The IR spectra in Fig. 6.7 show that the peaks at relatively higher frequencies (at 2212 cm^{-1} and 2224 cm^{-1}) become stronger with decreasing temperature while those at lower frequencies (at 2173 cm^{-1} and 2191 cm^{-1}) diminish. The former peaks correspond to the lowest energy level and the latter peaks to the two higher levels. Stated another way, the IR peaks at higher frequency correspond to the single lowest level and those of lower frequency correspond to the two levels with higher energy. Considering only the relative position of the peaks, the experimental spectra correspond to the situation of $\alpha \sim 0$ in Fig. 6.11, and the lowest level corresponds to the orientation that the deuteron is on the plane of 2,6-dibromobenzene. This result shows remarkable contrast to that of 26DCT in which all the protons and deuterons are pointing out of the molecular plane. Fig. 6.12 shows the angle dependence of the frequency of C-H stretching mode in $C_6H_3Br_2$-CHD_2 obtained by the DFT calculation. The IR spectra (Fig. 6.9) show that the peaks at relatively higher frequencies (at 2981 cm^{-1} and 2994 cm^{-1}) become weaker with decreasing temperature while those at lower frequencies (at 2927 cm^{-1}, 2930 cm^{-1} and 2946 cm^{-1}) become stronger. This situation corresponds to the rotational angle $\alpha \sim 0$, and the lowest level corresponds to the orientation that one of the deuteron is on the molecular plane.

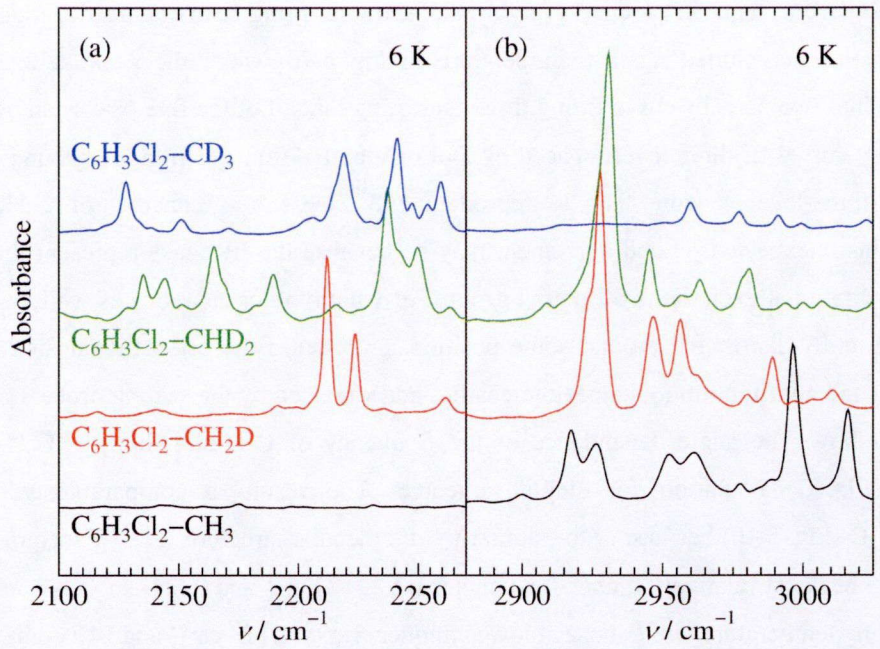

Fig. 6.6 Infrared absorption spectra obtained at 6 K for 2,6-dibromotoluene and its methyl-deuterated analogs; (a) from 2100 cm^{-1} to 2270 cm^{-1}, (b) from 2880 cm^{-1} to 3025 cm^{-1}.

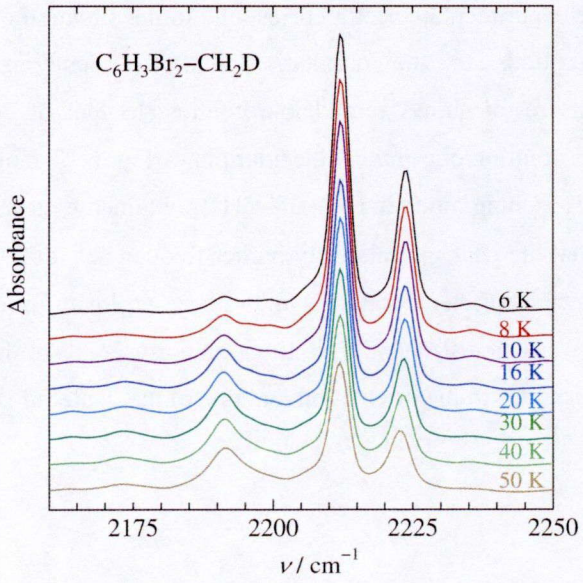

Fig. 6.7 Temperature evolution of the IR spectra for $C_6H_3Br_2$-CH_2D in the spectral range 2160 – 2250 cm^{-1}.

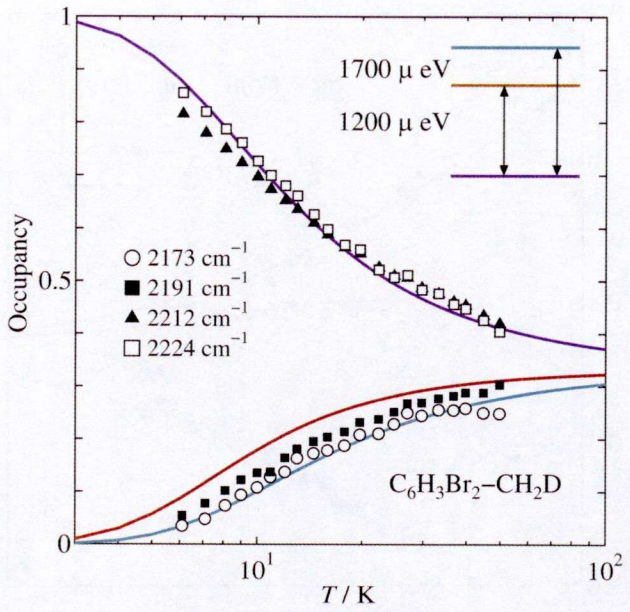

Fig. 6.8 Temperature dependence of the scaled intensity of four peaks obtained for $C_6H_3Br_2$-CH_2D (see Fig.6.7), which are consistent with the occupancy for the three-level energy scheme obtained from the Schottky heat capacity (solid curves).

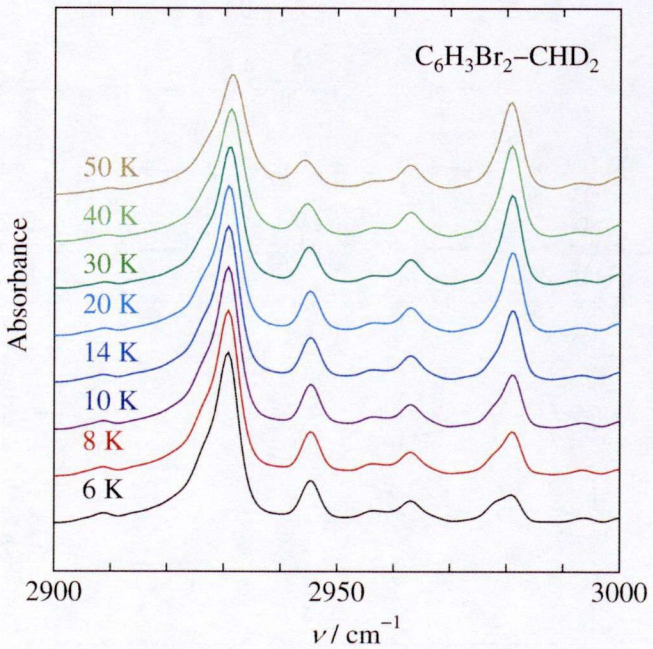

Fig. 6.9 Temperature evolution of the IR spectra for $C_6H_3Br_2$-CHD_2 in the spectral range 2900 – 3000 cm^{-1}.

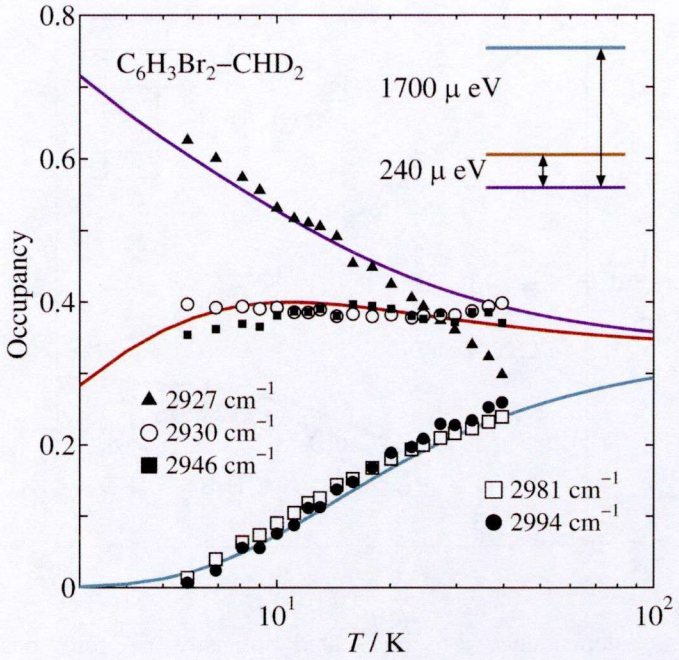

Fig. 6.10 Temperature dependence of the scaled intensity of four peaks obtained for $C_6H_3Br_2$-CHD_2 (see Fig.6.9), which are consistent with the occupancy for the three-level energy scheme obtained from the Schottky heat capacity (solid curves).

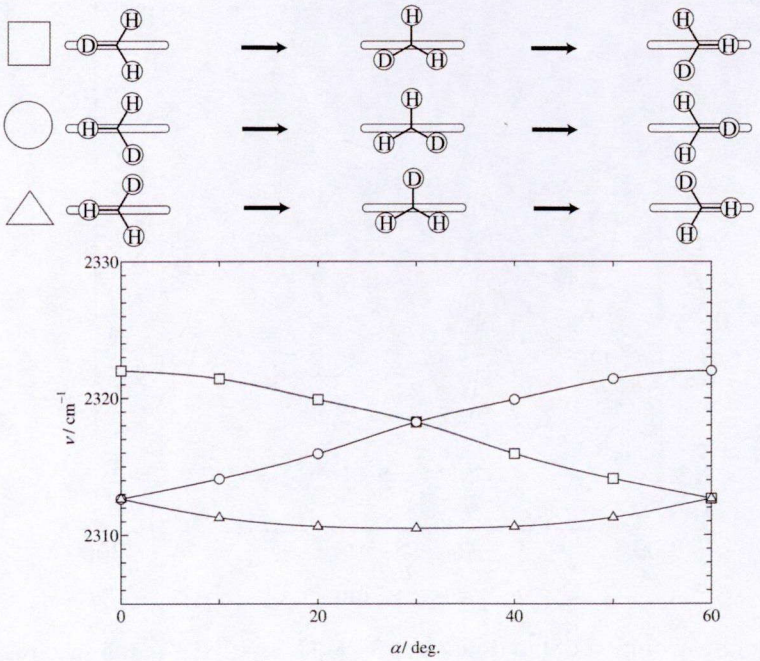

Fig. 6.11 Frequency of C-D stretching mode in -CH_2D for $C_6H_3Br_2$-CH_2D obtained by DFT calculation for single molecule. The pictures above the figure show the orientations of the methyl groups projected parallel to the 2,6-dibromobenzen frame.

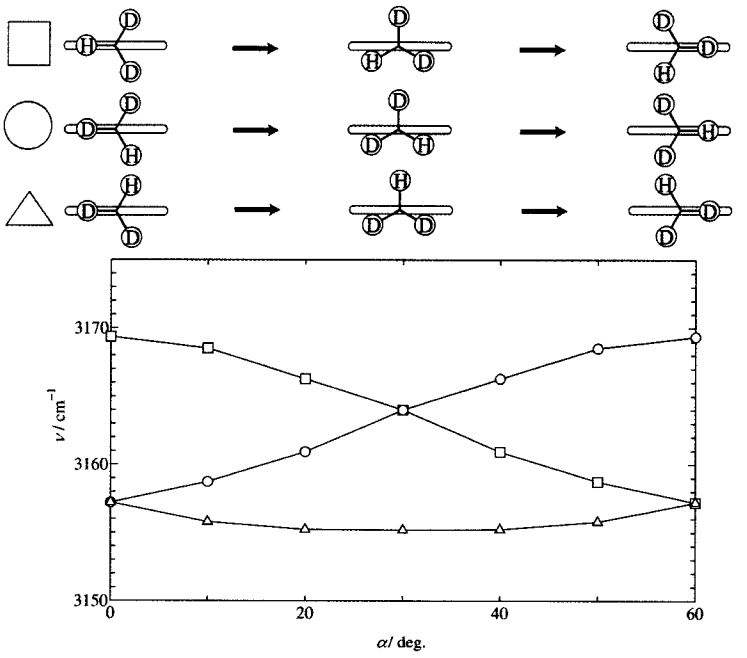

Fig. 6.12 Frequency of C-H stretching mode in -CHD_2 for $C_6H_3Br_2$-CHD_2 obtained by DFT calculation for single molecule. The pictures above the figure show the orientations of the methyl groups projected parallel to the 2,6-dibromobenzen frame.

6.4 Summary

Heat capacity measurements were made for 2,6-dibromotoluene ($C_6H_3Br_2$-CH_3) and its methyl-deuterated analogs ($C_6H_3Br_2$-CH_2D, $C_6H_3Br_2$-CHD_2 and $C_6H_3Br_2$-CD_3) between 0.35 K and 300 K by adiabatic calorimetry and relaxation calorimetry. A Schottky type anomaly was found for $C_6H_3Br_2$-CH_2D and $C_6H_3Br_2$-CHD_2 below 40 K. The excess heat capacity of $C_6H_3Br_2$-CH_2D was explained by an energy scheme involving three levels, $g_1/g_0 = g_2/g_0 = 1$, spaced by 1200 μeV and 1700 μeV from the ground level. The excess heat capacity of $C_6H_3Br_2$-CHD_2, on the other hand, was broader than the Schottky function, indicating some distribution in the energy levels. The best results of the Schottky model fitting gave the energy scheme of three levels spaced by 240 μeV and 1700 μeV from the ground level. The energy schemes of $C_6H_3Br_2$-CH_2D and $C_6H_3Br_2$-CHD_2 are in the inverse relation with each other, which is similar to the results of 26DCT. The excess entropies for both compounds are close to R ln 3 (= 9.13 J K^{-1} mol^{-1}), showing that the orientational ordering of the rotor completes at the lowest temperature of the measurement.

Infrared absorption measurements were also made between 6 K and 100 K in the spectral range from 400 cm^{-1} to 4000 cm^{-1}. The peaks connected with C-H or C-D stretching modes of -CH_2D and

-CHD_2 show a strong temperature dependence of their intensities. The scaled intensities agree well with the occupancy of three levels obtained from the excess heat capacities.

In order to understand the different frequencies of the C-H or C-D stretching modes depending on the rotational angle, DFT calculations for single molecule of $C_6H_3Br_2$-CH_2D and $C_6H_3Br_2$-CHD_2 were also carried out. The results of the calculation qualitatively reproduced the spectra observed by the experiment. In addition, the possible angle of rotation was derived by comparing the experimental and calculated results. According to that, the partially deuterated methyl groups of 26DBT are oriented in crystal in a way that one hydrogen atoms is placed (almost) on the molecular plane. This result shows a remarkable contrast to that of 26DCT, indicating that the different size of halogens control the orientations of the methyl groups.

6.5 References for Chapter 6

[1] A. Boudjada, J. Meinnel, A. Boucekkine, O. J. Hernandez and M. T. Fernández-Diaz, *J. Chem. Phys.* **117** (2002) 22.

[2] J. Meinnel, W. Häusler, M. Mani, M. Tazi, M. Nusimovici, M. Sanquer, B. Wyncke, A. Heidemann, C. J. Carlile, J. Tomkinson and B. Hennion, *Physica B* **180** (1992) 711.

[3] J. Meinnel, H. Grimm, O. Hernandez and E. Jansen, *Physica B* **350** (2004) e459.

[4] M. Prager and A. Heidemann, *Chem. Rev.* **97** (1997) 2933.

[5] S.V.R. Mastrngelo and R.W. Dornte, *J. Am. Chem. Soc.* **77** (1955) 6200.

Chapter 7

Orientational Ordering of Partially Deuterated Methyl Groups in Solid Toluene

7.1 Introduction

The investigations for 2,6-dihalogenotoluenes (26DHTs) revealed that the partially deuterated methyl groups undergo orientational ordering in a non-cooperative way at low temperature in solid. In addition, through this ordering process, the most stable orientations of the rotors were also estimated. According to these investigations, the halogens in 26DHT seem to play an important role in controlling the intermolecular distances, hence the orientations of the methyl groups. For further investigation, toluene was chosen.

The solid state of toluene has been extensively studied before. Toluene has two crystalline phases: the stable crystal called α-phase and the metastable crystal called β-phase. The melting point of the α-phase is reported to be 178.15 K [1]. The crystal structure of α-phase was first determined by X-ray diffraction measurement [2] and later it was refined by neutron diffraction experiment on $C_6D_5CD_3$ [3,4]. According to them, the α-phase has space group $P2_1/c$, $Z = 8$, $a = 0.74724$ nm, $b = 0.57882$ nm, $c = 2.70798$ nm, $\beta = 107.65°$ with unit cell volume of 1.11612 nm^3 and there are two inequivalent methyl groups (Fig. 7.1(a)). Both two methyl groups are oriented so that all the hydrogen atoms are out of the benzene plane (Fig. 7.1(b)). The rotational tunneling of methyl groups in the α-phase was observed at 26 μeV and 28.5 μeV, corresponding to the two inequivalent methyl groups by inelastic neutron scattering (INS) measurement [5]. The crystal structure of the β-phase was investigated by X-ray diffraction [6]. The β-phase has space group *Pbcn*, $Z = 8$, $a = 1.385$ nm, $b = 1.142$ nm, $c = 0.739$ nm with unit cell volume of 1.169 nm^3 and there is only one type of methyl group. The melting point of the β-phase is reported to be 154 K. In addition to these two crystalline phases, glass of isotropic liquid is also known. The rotational dynamics of methyl groups in the liquid glass was investigated by INS, and a distribution in tunnel frequency was detected [7]. The glass transition was observed by adiabatic calorimetry at 117 K [8]. Fig. 7.2 schematically shows the phase behavior of toluene. The glass of liquid can be obtained by vapor deposition onto the substrate

at low temperature. When the sample size is very small (about 1 mm^3) the liquid glass can also be formed by normal cooling (~ −10 K min^{-1}) [7]. When the sample is large (a few grams), it is difficult to obtain the glass of liquid by normal cooling because the (metastable) undercooled liquid is (kinetically) quite unstable. In order to avoid the stabilization to the crystalline liquid phase, small amount of benzene is often mixed with toluene, which (kinetically) stabilizes the undercooled phase [8]. The β-phase is obtained by annealing the undercooled liquid around 120 K. The α-phase is formed by annealing the sample at 160 K. Many spectroscopic measurements have been performed for toluene and its deuterated analogs in the gas phase [8-11], the liquid phase [12] and the solid phase [13-15].

Despite of a large number of such investigations made in the past, little has been reported on the low temperature behavior of methyl-partially-deuterated toluene in solid. The aim of the work described in this chapter was to investigate the thermodynamic properties of methyl-partially-deuterated toluenes in solid, and to discuss the orientational ordering of the methyl groups comparing with the results of 26DCT and 26DBT.

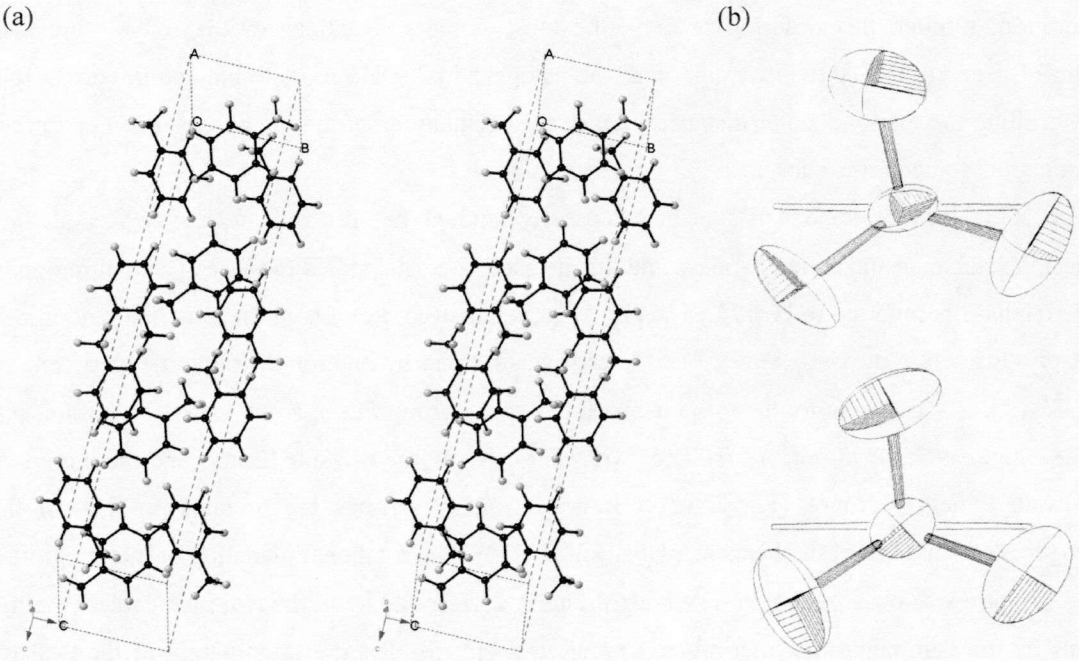

Fig. 7.1 (a) Stereo image of the α-phase of toluene. (b) The orientation of methyl groups of the independent toluene molecules as projected parallel to their ring plane [2].

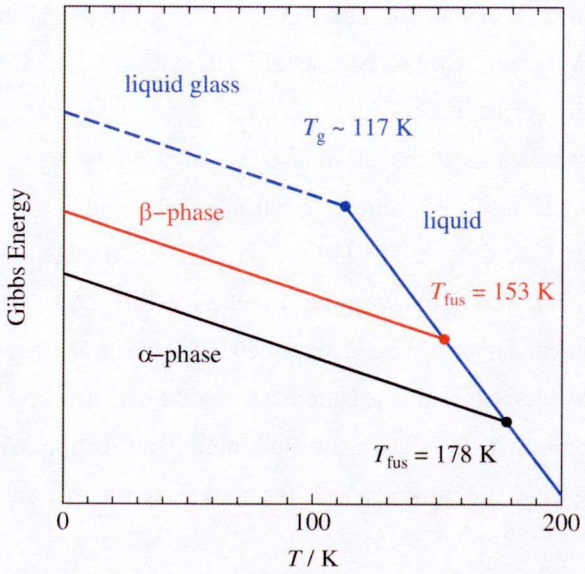

Fig. 7.2 Schematic diagram of Gibbs energy for toluene.

7.2 Experimental

7.2.1 Samples

$C_6H_5CH_3$, $C_6H_5CH_2D$ (109.5%D) and $C_6H_5CHD_2$ (104.2%D) were purchased from Wako Pure Chemical Industries. $C_6H_5CD_3$ (98%D) was purchased from Cambridge Isotope Laboratories (CIL). The deuteration degrees were examined by NMR measurement. ^{1}H NMR (500 HMz, $CDCl_3$) δ 7.27 (2H at the *meta* positions of benzene), 7.18 (3H at the *ortho* and *para* positions of benzene), 2.37 (protons of the methyl groups). The deuteration degrees were estimated by taking the ratio of the peak integrals at δ 7.18 and δ 2.37. The chemical purities were determined using the fractional melting method (Section 3.2.1) to be 99.9929%, 99.9891%, 99.4984% and 99.9833% for $C_6H_5CH_3$, $C_6H_5CH_2D$, $C_6H_5CHD_2$ and $C_6H_5CD_3$, respectively. In addition to these four compounds, two ring deuterated compounds $C_6D_5CH_3$ (99.96%D, Sigma Aldrich) and $C_6D_5CD_3$ (99.62%D, Isotec) were also purchased. The chemical purities were 99.9496% for $C_6D_5CH_3$ and 99.9949% $C_6D_5CD_3$, respectively.

7.2.2 Heat Capacity Measurement

The heat capacity measurements were made between 5 K and 200 K by adiabatic calorimetry, and between 0.35 K and 20 K by relaxation calorimetry. The amounts of samples used for the adiabatic calorimetry were 1.770974 g (19.22080 mmol), 1.799589 g (19.32038 mmol), 1.898478 g

(20.16424 mmol), 19.37655 g (20.36374 mmol), 1.84900 g (19.02867 mmol) and 2.057867 g (20.54011 mmol) for $C_6H_5CH_3$, $C_6H_5CH_2D$, $C_6H_5CHD_2$, $C_6H_5CD_3$, $C_6D_5CH_3$ and $C_6D_5CD_3$, respectively, after buoyancy correction.

The amounts of the samples used for the relaxation calorimetry were 0.340 mg (3.69 μmol), 0.400 mg (4.29 μmol), 0.425 mg (4.51 μmol), 0.360 mg (3.78 μmol), 0.355 mg (3.65 μmol) and 0.326 mg (3.25 μmol) for $C_6H_5CH_3$, $C_6H_5CH_2D$, $C_6H_5CHD_2$, $C_6H_5CD_3$, $C_6D_5CH_3$ and $C_6D_5CD_3$, respectively. The copper cell for liquid samples (Section 3.1.5, Case 2) was used. The sample amounts for the relaxation calorimetry were determined referring to the heat capacities of adiabatic calorimetry. In addition to this series of measurement, additional measurement with larger sample size for $C_6H_5CH_2D$ was also carried out using the aluminum pan (Section 3.1.5, Case 3). The sample amount was 16.11786 mg (173.041 μmol) which is about forty times more than that in the copper cell.

With the adiabatic calorimetry, only the α-phase was measured for all compounds, while the glass of liquid phase as well as the α-phase was measured with the relaxation calorimetry. The measurement of the β-phase was not carried out, since the homogeneous β-phase could not be obtained.

7.2.3 IR Measurement

Infrared absorption measurements were made for $C_6H_5CH_3$, $C_6H_5CH_2D$, $C_6H_5CHD_2$ and $C_6H_5CD_3$ between 6 K and 100 K in the spectra range from 400 cm^{-1} to 4000 cm^{-1}. KBr single crystals were used as a sample holder. The sample was first rapidly cooled down (~ – 100 K min^{-1}) to 100 K in order to obtain the glass of liquid. After the measurement of the glass, the sample was heated up to 160 K and annealed for about 1 hour to obtain the homogeneous α-phase.

7.3 Results and Discussion

7.3.1 Heat Capacities

Fig. 7.3 shows the heat capacities of the α-phase for the whole temperature range. There is no anomaly at high temperatures except for the fusion at 178 K. The thermodynamic quantities associated with the fusion are listed in Table 7.1. All the six compounds have similar value of fusion entropy. At low temperature, $C_6H_5CH_2D$ and $C_6H_5CHD_2$ show a broad anomaly in heat capacity below 20 K (Fig. 7.4), which is of the same type as observed for the partially methyl-deuterated 26DCTs or 26DBTs. The other four compounds ($C_6H_5CH_3$, $C_6H_5CH_2D$, $C_6H_5CHD_2$ and $C_6H_5CD_3$)

do not show such an anomaly in heat capacity, which differ to each other only by the lattice contribution due to the different molecular mass. The excess heat capacities of $C_6H_5CH_2D$ and $C_6H_5CHD_2$ were estimated in the following way. First the vibrational heat capacities (38 modes) were subtracted from the total heat capacities for four compounds ($C_6H_5CH_3$, $C_6H_5CH_2D$, $C_6H_5CHD_2$ and $C_6H_5CD_3$). The vibrational heat capacities were calculated using Einstein model (Section 3.2.2). The frequencies of 38 intramolecular modes were obtained from ref. [12] in which all the modes were assigned by IR and Raman spectroscopy. The heat capacities, after subtracting the contributions of 38 modes, consist of 7 modes: three translational and three rotational modes of the whole molecule and one torsional mode of the methyl group. These heat capacities of $C_6H_5CH_3$, and $C_6H_5CD_3$ were scaled against temperature to finally obtain the base heat capacities of $C_6H_5CH_2D$ and $C_6H_5CHD_2$. Fig. 7.5 and Fig. 7.6 show the excess heat capacity and the excess entropy of $C_6H_5CH_2D$ and $C_6H_5CHD_2$. It is interesting that the excess entropies of both compounds are significantly smaller than R ln 3. The shape of excess heat capacities also considerably deviates from the Schottky function. As far as the equilibrium heat capacities are obtained, the deficient entropy has to be compensated somewhere. Since the entropy of fusion does not differ significantly with deuteration, and since there is no thermal anomaly at high temperatures, the deficient entropy must be hidden at low temperatures. One possibility is that the orientational ordering of the methyl groups freezes below 5 K where the excess heat capacity significantly deviates from the model curve. If this is the case, some evidence of glass transition could be observed. Since the measurement around 5 K was performed by relaxation calorimetry, it was not able to check the existence of slow dynamics typical for glass transitions. As a trial to detect some evidence of glass transition, another measurement of $C_6H_5CH_2D$ with larger sample amounts (about forty times more) were also carried out using aluminum pan. In relaxation calorimetry, the relaxation time constant is proportional to the total heat capacity. Hence the time constant is long for the large size of sample. In general, the time constant of relaxation due to the glass transition is independent of the sample size, thus enlargement of the sample amount was expected to make a difference in heat capacity curve. However the result of the measurement was exactly the same as that of the small-size sample, which indicates at least that the ordering process does not freeze at once in a cooperative manner like liquid glass. The freezing of ordering may occur continuously with decreasing temperature over the wide temperature range. The possibility of continuous (or gradual) freezing is also supported by the fact that the excess heat capacity curve is definitely broader than Schottky functions. If the freezing occurs cooperatively at one temperature point, the excess heat capacity would be stepwise and the curve below that temperature would be fitted by another Schottky function.

Another possibility to explain the small excess entropy is that some excitations are hidden below 0.35 K, the lowest temperature of the measurement. This is the same idea proposed on the methyl-partially-deuterated 4-methylpyridines (4MPs). If this is true, some quantum mechanical

tunneling mode should be responsible for those excitations at low frequencies. Since the tunneling among the three H and/or D atoms only gives three tunneling states at most, some cooperative quantum mode among several methyl groups is expected. The distance between the nearest neighboring methyl groups is 3.98 Å which is similar to that of 4MP (3.95 Å). It is still open to question whether the methyl groups in the α-phase can form a network providing some cooperative quantum modes such as the breather modes in the sine-Gordon theory proposed for 4MP.

In the glass of liquid phase, $C_6H_5CH_2D$ and $C_6H_5CHD_2$ also show anomaly in heat capacity below 20 K (Fig. 7.7), which are much broader than those of the α-phase. Figs. 7.8 (a) and (b) show the excess contributions in heat capacity and entropy, respectively. The procedure to obtain the excess heat capacities is the same to that of the α-phase. The broad excess heat capacities indicate that there are various kinds of potentials surrounding the methyl groups, which is possible because the molecular orientation is highly disordered in this phase. It is also interesting that the two excess heat capacities are almost identical, indicating that the averaged rotational potential are quite similar for $-CH_2D$ and $-CHD_2$. The excess entropies are also less than $R \ln 3$. Since this glassy phase definitely involves disorder in structure, the small excess entropy is reasonable.

Table 7.1 Thermodynamic quantities associated with fusion of toluene and its methyl-deuterated analogs. The sample purities are also listed here.

Sample	deuteration	purity	T_{fus}	$\Delta_{fus}H$	$\Delta_{fus}S$
	D%	%	K	kJ mol^{-1}	J K^{-1} mol^{-1}
C_6D_5-CD_3	99.62	99.9949	178.489	6.607	37.01
C_6H_5-CD_3	99.96	99.9496	178.106	6.587	37.01
C_6H_5-CD_3	98	99.9833	178.458	6.640	37.22
C_6H_5-CHD_2	104.2*	99.4984	178.401	6.636	37.47
C_6H_5-CH_2D	109.5*	99.9891	178.252	6.622	37.16
C_6H_5-CH_3	-	99.9929	178.134	6.612	37.13
C_6H_5-CH_3 (ref. [1])	-	99.999	178.15	6.636	37.25

* The deuteration degree more than 100% indicates the existence of fully methyl-deuterated compounds.

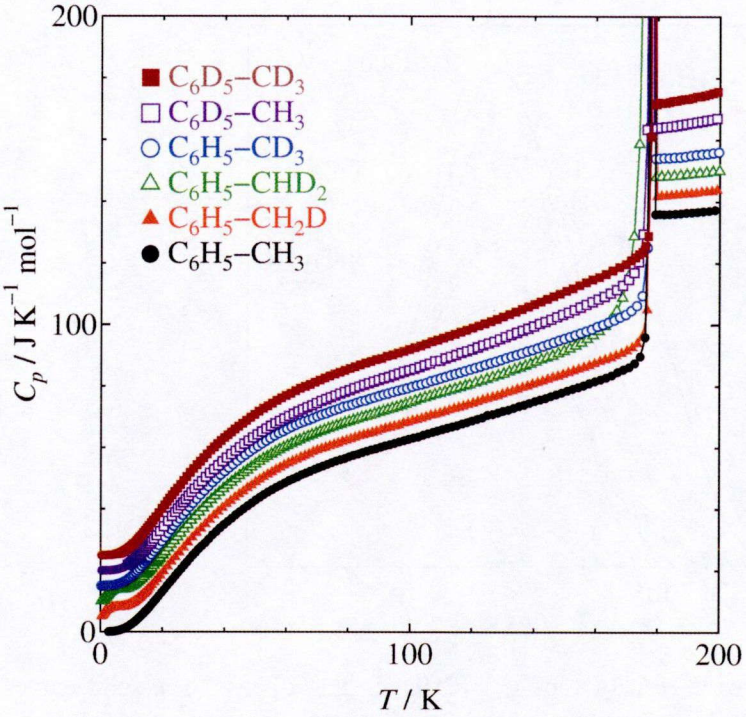

Fig. 7.3
Molar heat capacity of toluene and its methyl-deuterated analogs. The ordinate is for $C_6H_5CH_3$. The results for other five compounds are successively shifted upward by 5 J K^{-1} mol^{-1}

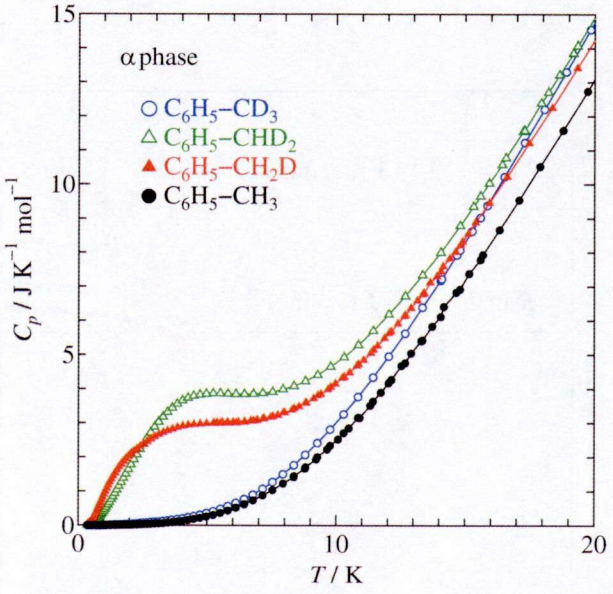

Fig. 7.4 Molar heat capacities of toluene and its methyl-deuterated analogs in the α-phase below 20 K.

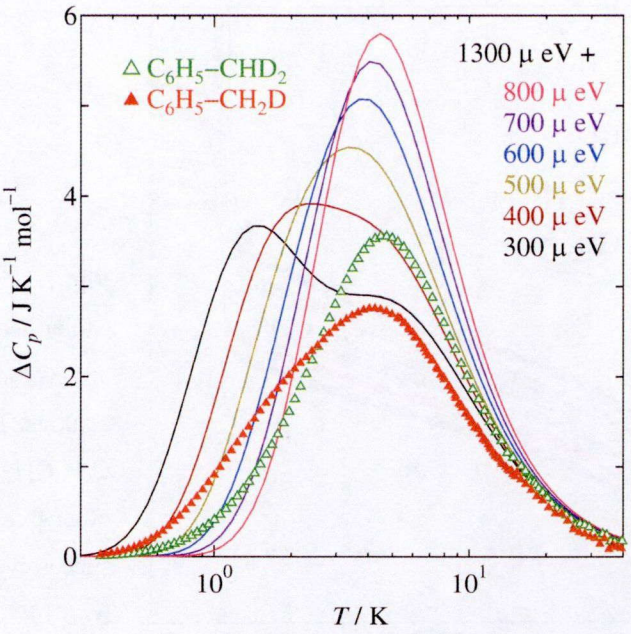

Fig. 7.5 Excess heat capacities of $C_6H_5CH_2D$ and $C_6H_5CHD_2$ in the α-phase. The solid curves show the Schottky functions with three levels. The list of spacing from the ground level is given in the figure.

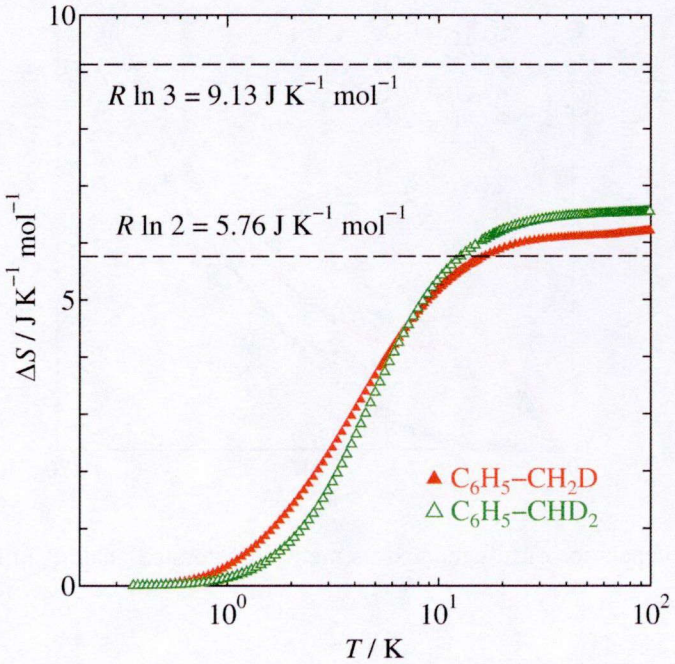

Fig. 7.6 Excess entropies of $C_6H_3Cl_2$-CH_2D and $C_6H_3Cl_2$-CHD_2.

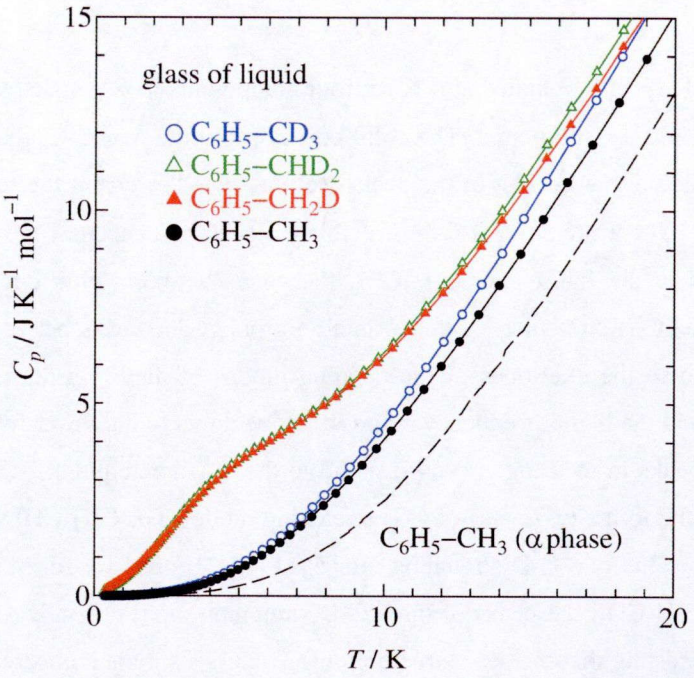

Fig. 7.7 Molar heat capacities of toluene and its methyl-deuterated analogs in the glass of liquid phase below 20 K.

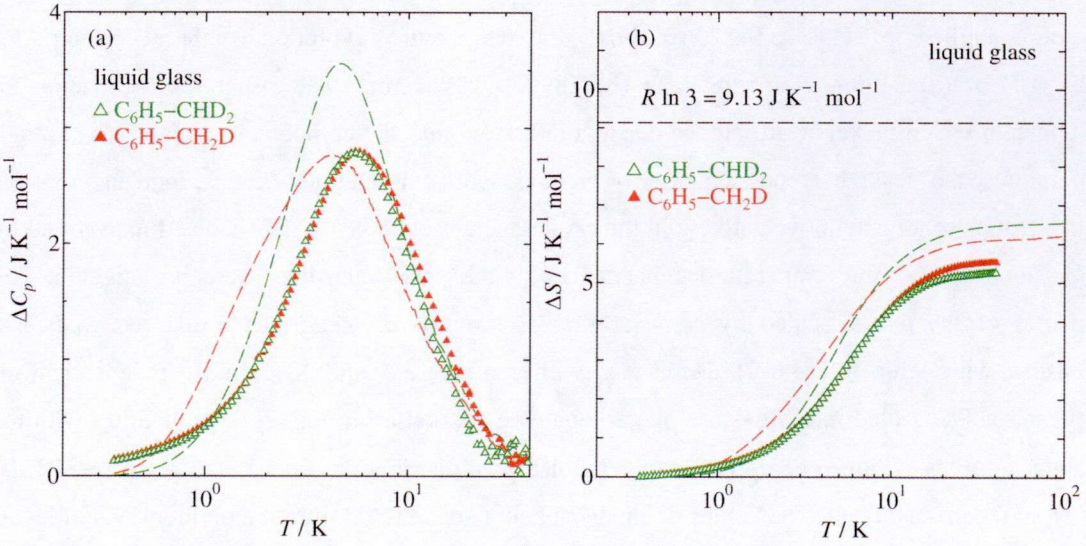

Fig. 7.8 (a) Excess heat capacities and (b) excess entropies of $C_6H_5CH_2D$ and $C_6H_5CHD_2$ in the glass of liquid phase. The dashed lines show the results for the α-phase.

7.3.2 IR measurement

Fig. 7.9 shows the IR spectra obtained at 6 K for four compounds in two spectral ranges: (a) 2100 – 2270 cm^{-1} and (b) 2820 – 3000 cm^{-1}. The solid curves show the results of the α-phase and the dotted curves of the liquid glass. Most of the peaks were assigned referring the results reported for the liquid phase [13]. There are several C-H stretching modes of benzene ring above 3000 cm^{-1} which are not shown in the figure. For $C_6H_5CH_3$, the peaks between 2900 cm^{-1} and 3000 cm^{-1} correspond to the three C-H stretching modes of methyl groups. The peaks between 2820 cm^{-1} and 2900 cm^{-1} correspond to the overtones of the bending modes of methyl groups. With successive deuteration, the peaks in the higher frequency range (b) move down to the lower frequency range (a). For $C_6H_5CH_2D$, the peaks in the range (a) correspond to the C-D stretching of -CH_2D and those in the range (b) correspond to the two types of C-H stretching modes. For $C_6H_5CHD_2$, the peaks in the range (a) correspond to the two C-D stretching modes of -CHD_2 and those in the range (b) to the C-H stretching. For $C_6H_5CD_3$, the peaks of three C-D stretching modes of -CD_3 are clearly seen in the range (a). It is interesting that the peak structure of $C_6H_5CD_3$ is simple compared to the spectra of $C_6H_5CH_2D$ and $C_6H_5CHD_2$. The peaks of liquid glass (plotted by dotted lines) are generally broader than those of the α-phase (solid lines). The broadening comes from the heterogeneity of the surroundings of the methyl groups. The discussion hereafter is limited to the α-phase.

The temperature dependences of the peak intensities are investigated following the same analytical procedure applied to 26DCT. Fig. 7.10 shows the temperature evolution of the IR spectra for $C_6H_5CH_2D$ at (a) 2100 – 2260 cm^{-1} and (b) 2890 – 2990 cm^{-1}. The structures of spectra are complicated, which makes it difficult to deconvolute them into the components. In addition at high temperatures, the peaks become significantly broader due to the Doppler effects, indicates that the methyl groups of toluene move actively in the crystal. The spectra below 50 K were finally fitted by Voigt functions and the temperature dependences of the peak intensities were investigated. The intensities of the peaks, scaled by some arbitral factors, were categorized into three types, (1) increasing with temperature, (2) decreasing with temperature and (3) almost independent of temperature. The scaled intensities are plotted against temperature in Fig. 7.11, comparing with the occupancy curves of three energy levels under Boltzmann distribution spaced by 300 μeV and 1300 μeV from the ground level. The values of energy spacing are selected from the optional sets of levels shown in Fig. 7.4, which actually does not fit well with the excess heat capacity. As expected, the scaled intensities do not follow the model curves as well. For example, one of the scaled intensities corresponding to the highest level deviates to upward side of the model curve at low temperature, which shows that the real occupancy drops with decreasing temperature more gradually than expected from the Boltzmann distribution law. These results seem to support the view that the orientational ordering of the methyl groups is frozen continuously with decreasing temperature over

the wide temperature range.

Fig. 7.12 shows the temperature evolution of the IR spectra for $C_6H_5CHD_2$ and Fig. 7.13 shows the scaled intensities. The solid curves in Fig. 7.13 are the occupancies of three energy levels spaced by 500 μeV and 1300 μeV from the ground level. The calculated occupancy curves deviate from the experimental values, which is analogous to the results of $C_6H_5CH_2D$.

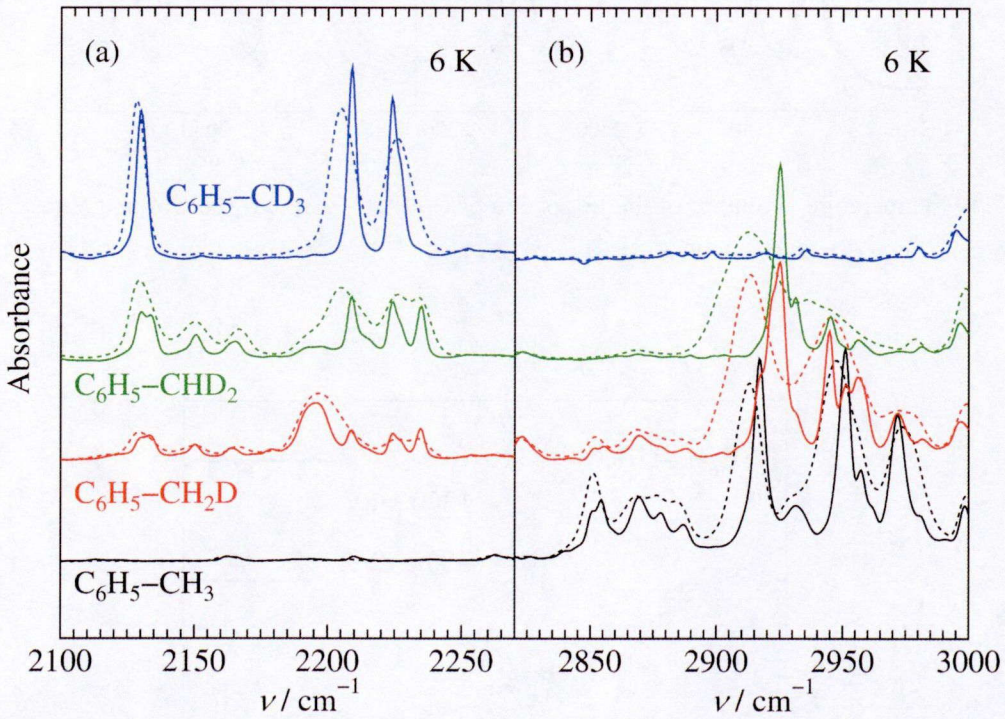

Fig. 7.9 Infrared absorption spectra obtained at 6 K for toluene and its methyl-deuterated analogs: (a) from 2100 cm^{-1} to 2270 cm^{-1}, (b) from 2820 cm^{-1} to 3000 cm^{-1}. The solid curves show the spectra of the α-phase and the dotted curves are those of the liquid glass.

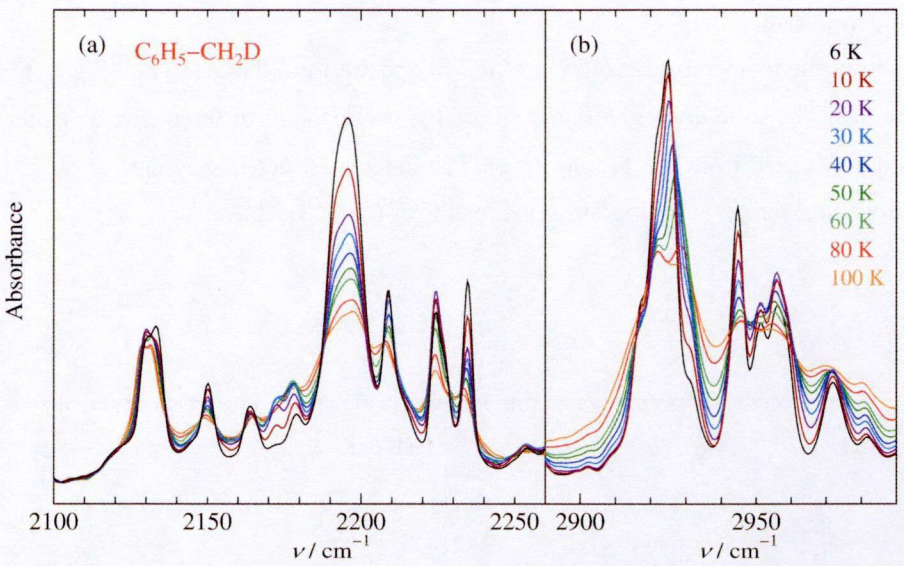

Fig. 7.10 Temperature evolution of the IR spectra of $C_6H_5CH_2D$ at two spectral range; (a) 2100 – 2260 cm^{-1} and (b) 2890 – 2990 cm^{-1}.

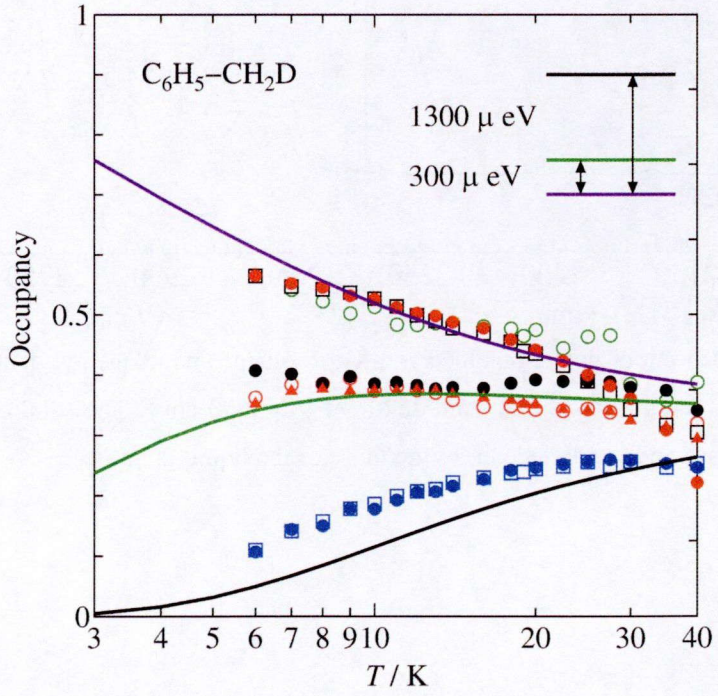

Fig. 7.11 Temperature dependences of the scaled intensities of seven peaks observed for $C_6H_5CH_2D$ (see Fig.7.10). The solid curves show the occupancies of three energy levels shown

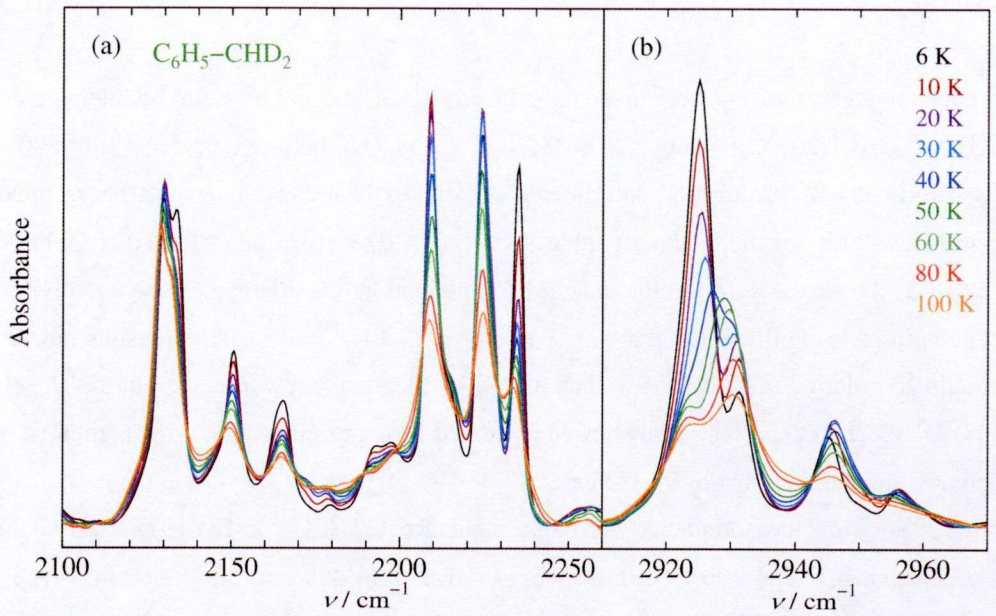

Fig. 7.12 Temperature evolution of the IR spectra for $C_6H_5CHD_2$ at two spectral range; (a) 2100 – 2260 cm^{-1} and (b) 2880 – 2980 cm^{-1}.

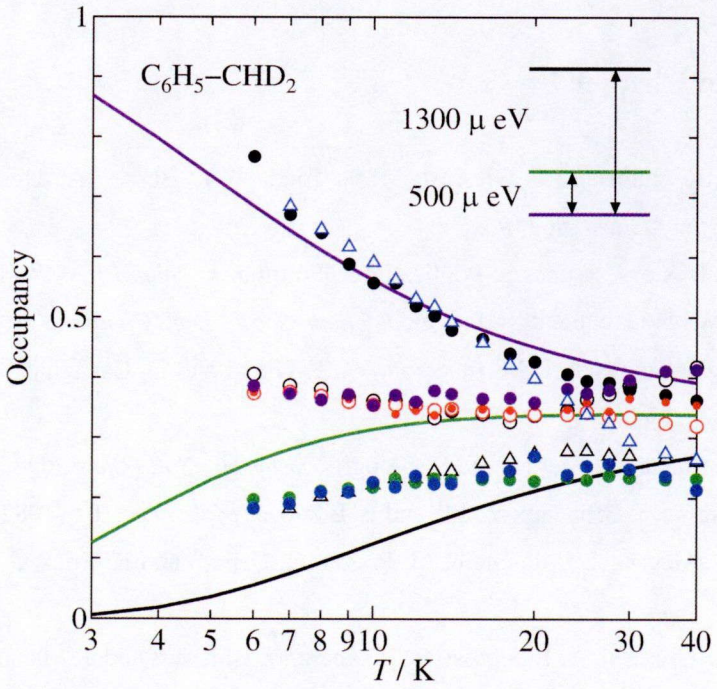

Fig. 7.13 Temperature dependences of the scaled intensities of seven peaks observed for $C_6H_5CHD_2$ (see Fig.7.12). The solid curves show the occupancies of three energy levels shown in the figure.

7.4 Summary

Heat capacity measurements were made for toluene ($C_6H_5CH_3$) and its methyl-deuterated analogs ($C_6H_5CH_2D$, $C_6H_5CHD_2$, $C_6H_5CD_3$, $C_6D_5CH_3$ and $C_6D_5CD_3$) between 0.35 K and 200 K by adiabatic calorimetry and relaxation calorimetry. An excess heat capacity with a broad maximum was found below 20 K for the α-phase (stable crystal) of $C_6H_5CH_2D$ and $C_6H_5CHD_2$. Unlike in the case of 26DCT, the excess contribution cannot be explained by the energy schemes involving three levels. The entropy is significantly less than R ln 3 (= 9.13 J K^{-1} mol^{-1}). These results indicate that the orientational ordering of -CH_2D as well as -CHD_2 is frozen in at lower temperatures. The glass of liquid $C_6H_5CH_2D$ and $C_6H_5CHD_2$ also showed an excess heat capacities at low temperatures, but the shape is much broader than that of the α-phase.

Infrared absorption measurements were also made for $C_6H_5CH_3$, $C_6H_5CH_2D$, $C_6H_5CHD_2$ and $C_6H_5CD_3$ between 6 K and 100 K in the spectral range from 400 cm^{-1} to 4000 cm^{-1}. The peaks connected with the C-H or C-D stretching modes of -CH_2D and -CHD_2 show significant temperature dependence for their intensities. The scaled intensities of the peaks show that the occupancy of the levels does not follow the Boltzmann distribution, which also indicates the freezing of the orientational ordering of the methyl groups.

7.5 References for Chapter 7

[1] D.W. Scott, G.B. Guthrie, J.F. Messerly, S.S. Todd, W.T. Berg, I.A. Hossenlopp and J.P. McCullough, *J. Phys. Chem.* **66** (1962) 911.

[2] M. Anderson, L. Bosio, J. Bruneaux-Poulle and R. Fourme, *J. Chim. Phys.* **74** (1977) 68.

[3] R.M. Ibberson, W.I.F. David and M. Prager, *J. Chem. Soc., Chem. Commun.* (1992) 1438.

[4] M. Prager, M. Monkenbusch, R.M. Ibberson, W.I.F. David and D. Cavagnat, *J. Chem. Phys.* **98** (1993) 5653.

[5] D. Cavagnat, A. Magerl, C. Vettier and S. Clough, *J. Phys. C: Solid State Phys.* **19** (1986) 6665.

[6] D. Andre, R. Fourme, J. Bruneaux-Poulle and L. Bosio, *J. Mol. Struct.* **81** (1982) 253.

[7] A.J. Moreno, A. Alegria, J. Colmenero, M. Prager, H. Grimm and B. Frick, *J. Chem. Phys.* **115** (2001) 8958.

[8] O. Yamamuro, I. Tsukushi, A. Lindqvist, S. Takahara, M.Ishikawa and T. Matsuo, *J. Phys. Chem. B* **102** (1998) 1605.

[9] K.S. Pitzer and D.W. Scott, *J. Am. Chem. Soc.* **65** (1943) 803.

[10] W.A. Kreiner, H.D. Rudolph and B.T. Tan, *J. Mol. Spectrosc.* **48** (1973) 86.

[11] W.J. Balfour and R.S. Ram, *Can. J. Phys.* **72** (1994) 1225.

[12] W. Siebrand, M.Z. Zgierski, F. Zerbetto, M.J. Wójcik, M. Boczar, T. Chakraborty, W.G. Kofron and E.C. Lim, *J. Chem. Phys.* **106** (1997) 6279.

[13] W.J. Balfour and Y. Fried, *Can. J. Phys.* **72** (1994) 1218.

[14] D. Cavagnat and J. Lascombe *J. Chem. Phys.* **76** (1982) 4336.

[15] D. Cavagnat, J. C. Cornut, R. Cavagnat, and J. Lascombe, *J. Chim. Phys. Phys.-Chim. Biol.* **75** (1978) 969.

[16] D. Cavagnat and J. C. Cornut, *J. Chim. Phys. Phys.-Chim. Biol.* **76** (1979) 975.

Chapter 8

Orientational Ordering of Partially Deuterated Methyl Groups in Solid Methyl Iodide

8.1 Introduction

The results of the investigations for 2,6-dichlorotoluene (26DCT), 2,6-dibromotoluene (26DBT) and toluene have revealed that the low temperature anomalies in heat capacity for $-CH_2D$ and $-CHD_2$ compounds are related to the orientational ordering of the methyl groups. The three energy levels obtained from the excess heat capacities were ascribed to the ground torsional levels of three different orientations. This interpretation was also supported by the infrared absorption spectroscopy.

There remains one issue unsolved yet that which physical factor is responsible for the energy differences among the three levels. Although it has been believed that deuteration induced anomalies are closely related to the tunneling motion of proton, the results of the investigations for the above three compounds showed that the spacing of three levels of $-CH_2D$ or $-CHD_2$ depend little on the tunnel frequencies of the $-CH_3$. For example, the energy difference among the three levels for the $-CH_2D$ species of the above three compounds are similar in magnitude (2700 μeV for 26DCT, 1700 μeV for 26DBT and 1300 μeV for toluene), while the rotational tunnel splitting of $-CH_3$ differ more than an order of magnitude (ν_t = 1.56 μeV for 26DCT, ν_t = 4.4 μeV for 26DBT and ν_t =26 μeV and 28.5 μeV for toluene). Some other physical factor should be accountable for the energy differences.

The compounds investigated so far have one common point that the methyl groups are connected to a planar frame, i.e. benzene or 2,6-dihalogenobenzene. Considering that the energy differences of three levels are similar in magnitude among 26DCT, 26DBT and toluene, it seems interesting to investigate the methyl compound with non-planar frame. For this reason, methyl iodide was chosen for the next material to be investigated. In this chapter, the results of the heat capacity measurements for methyl iodide and its deuterated analogs are described.

Methyl iodide consists of a methyl group connected by an iodide atom which is circular symmetrical to the rotational axis. The methyl groups show rotational tunneling at 2.44 μeV [1] which is similar in size to 26DCT (ν_t = 1.56 μeV). The basic crystal structure of methyl iodide has

been clarified by X-ray diffraction measurement [2]; the space group is *Pnma*, $Z = 4$, $a = 0.4597$ nm, $b = 0.6987$ nm, $c = 1.0117$ nm and the unit cell volume is 0.3249 nm^3 at 193 K. The positions of deuterons in the crystal structure at 4.5 K were also determined for the CD_3I by neutron diffraction measurement [3].

8.2 Experimental

8.2.1 Samples

CH_3I was purchased from Wako Pure Chemical Industries. CH_2DI (98%D) CHD_2I (98%D) and CD_3I (99.5%D) were purchased from CIL. The chemical purities were determined using the fractional melting method (Section 3.2.1), which were 99.9907%, 99.9582%, 99.9920% and 99.9350% for CH_3I, CH_2DI, CHD_2I and CD_3I, respectively.

8.2.2 Heat Capacity Measurement

Heat capacity measurements were made between 5 K and 240 K by adiabatic calorimetry, and between 0.35 K and 20 K by relaxation calorimetry. The amounts of samples used for the adiabatic calorimetry were 4.261126 g (30.02083 mmol), 4.06760 g (28.45567 mmol), 4.338701 g (30.14006 mmol) and 4.1376 g (28.54354 mmol) for CH_3I, CH_2DI, CHD_2I and CD_3I, respectively, after buoyancy correction.

The amounts of the sample used for the relaxation calorimetry were 33.2404 mg (234.188 μmol), 11.0752 mg (77.479 μmol), 12.0638 mg (83.804 μmol) and 23.86364 mg (160.998 μmol) for CH_3I, CH_2DI, CHD_2I and CD_3I, respectively. Since methyl iodide is highly volatile, the aluminum pan was used as a liquid sample cell (Section 3.1.5, Case 3). As mentioned before, the disadvantage of aluminum pan is that the heat capacity below the superconducting transition at 1.2 K can be easily changed with mechanical deformation. In this respect, the subtraction of the aluminum heat capacity always involves some error. In the case of methyl iodide, CH_2DI and CHD_2I show huge heat capacity at this low temperature range, so the small error in aluminum pan is negligible. However the heat capacities of CH_3I and CD_3I are small enough at this temperature that the error from the aluminum pan is not negligible. For this reason, any detailed discussion on the heat capacities of CH_3I and CD_3I at this temperature range will not be undertaken.

8.3 Results and Discussion

Fig. 8.1 shows the heat capacities of four compounds in the whole temperature range. There is no anomaly at high temperatures except for the fusion at 206 K. The thermodynamic quantities associated with the fusion are listed in Table 8.1 together with the sample purities. All the four compounds have similar value of fusion entropy. At low temperature, CH_2DI and CHD_2I show dramatic increase in heat capacity below 5 K (Fig. 8.2) which does not reach to a maximum even at the lowest temperature of the measurement (0.35 K). The gradients of the heat capacity curves seem to obey T^{-2} tendency, which is typical for the Schottky functions in their high temperature limit (Fig. 8.2 inset). It is very interesting that the anomaly appears at much lower temperatures comparing to those of the previous compounds. Fig. 8.3 shows the excess heat capacities after subtracting the lattice heat capacities. The lattice heat capacities were estimated from the heat capacities of CH_3I and CD_3I, which are almost the same at low temperatures. Fig. 8.3 also shows the results of fitting by Schottky function with three energy levels. The spacing between the levels was 10.5 μeV (doubly degenerated) for CH_2DI and 10 μeV and 42 μeV for CHD_2I. Since the fitting was made only on the high temperature side of the anomalies, the results of the fitting are rather arbitral. Nevertheless it is clear that the three levels of CH_2DI and CHD_2I are not in the inverse relation, contrary to the results for 26DCT or 26DBT. The inverse relation may be related to the plane symmetry of the functional groups bonded to the methyl groups.

The IR measurements for the four compounds down to 6 K were also made, but the intensities of peaks connected with C-H or C-D stretching modes do not vary with temperature, which is consistent with the calorimetric results. The energy spacing by several tens μeV corresponds to less than 1 K in temperature unit, which is much lower than 6 K.

Table 8.1 Thermodynamic quantities associated with the fusion of methyl iodide and its deuterated analogs. The sample purities are also listed.

Compounds	deuteration	purity	T_{fus}	$\Delta_{fus}H$	$\Delta_{fus}S$
	%D	%	K	kJ mol^{-1}	J K^{-1} mol^{-1}
CH_3I	-	99.9907	206.664	7.351	35.58
CH_2DI	98	99.9582	206.267	7.327	35.54
CHD_2I	98	99.99120	205.800	7.299	35.48
CD_3I	99.5	99.9351	205.389	7.258	35.37

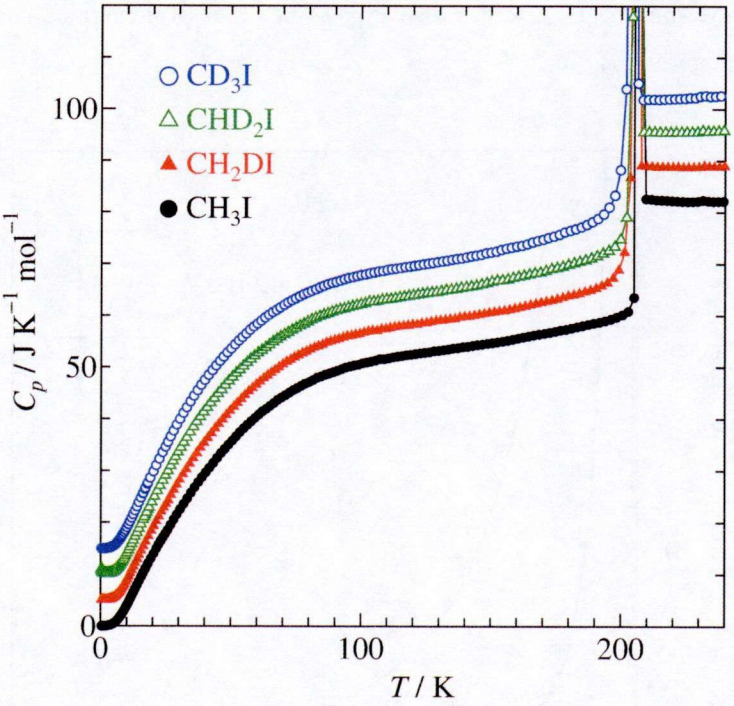

Fig. 8.1 Molar heat capacities of methyl iodide and its deuterated analogs. The ordinate is for CH_3I. The results for other three compounds are successively shifted upward by 5 J K^{-1} mol^{-1}.

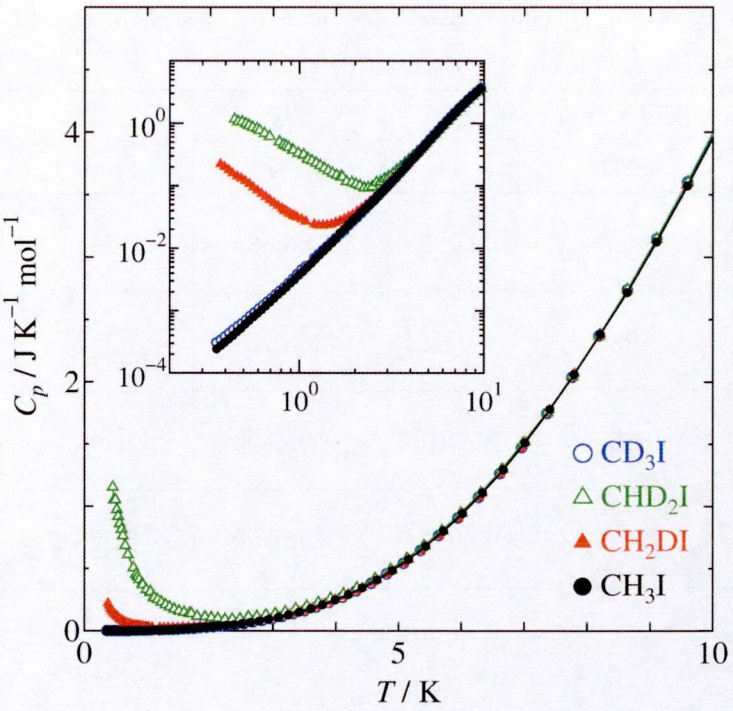

Fig. 8.2 Low temperature heat capacities of methyl iodide and its deuterated analogs. The inset shows the double logarithmic plot.

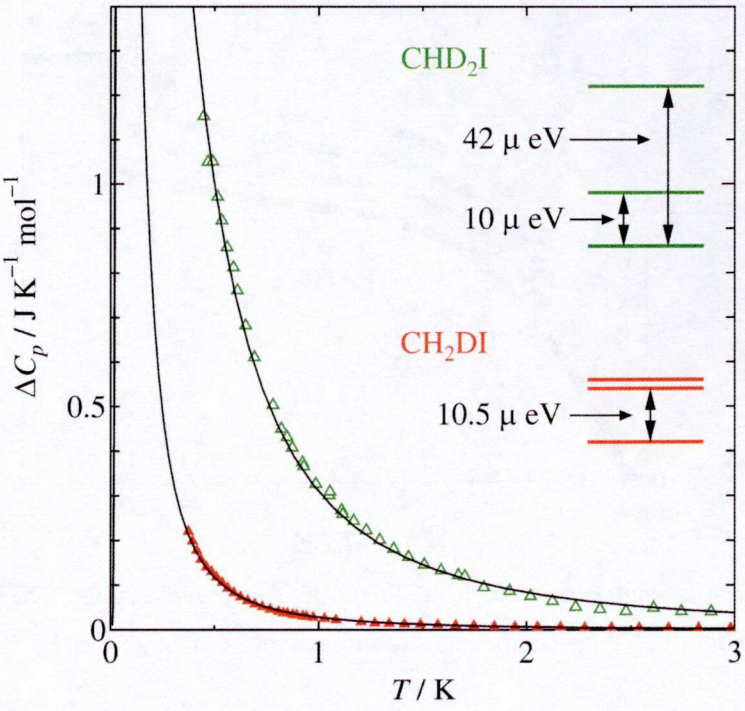

Fig. 8.3 Excess heat capacities of CH_2DI and CHD_2I. The solid curves show the Schottky functions with three energy levels. The energy scheme is also given in the figure.

8.4 Summary

Heat capacity measurements were made for methyl iodide (CH_3I) and its deuterated analogs, (CH_2DI, CHD_2I and CD_3I) between 0.35 K and 240 K by adiabatic calorimetry and relaxation calorimetry. Excess heat capacities were found only below 5 K for CH_2DI and CHD_2I, showing a remarkable contrast to the other partially deuterated compounds studied before such as 26DCT, 26DBT and toluene. The significantly small energy spacing indicates that the symmetry of the functional groups attached to the methyl groups is important for determining the energy scheme.

8.5 References for Chapter 8

[1] M. Prager, J. Stanislawski and W. Hausler, *J. Chem. Phys.* **86** (1987) 2563.

[2] T. Kawaguchi, M. Hijikigawa, Y. Hayafuji, M. Ikeda, R. Fukushima and Y. Tomiie, *Bull. Chem. Soc. Jpn.* **46** (1973) 53.

[3] R.M. Ibberson and M. Prager, *Z. Kristallogr.* **222** (2007) 416.

Chapter 9

Orientational Ordering of Partially Deuterated Methyl Groups in Solid Methanol

9.1 Introduction

The results of the investigation for methyl iodide strongly indicate that the structure of excess heat capacities for $-CH_2D$ and $-CHD_2$ compounds depends on the molecular structure, especially on the symmetry of the functional group bonded to the methyl group. In order to confirm this, methanol was chosen for the further investigation. The hydroxy group of methanol is plane symmetrical to the methyl group, but not two-fold symmetrical as in the case of 2,6-dichlorotoluene (26DCT), 2,6-dibromotoluene (26DBT) and toluene.

The phase behavior of solid methanol is rather complicated. It has at least two crystalline phases, α-phase and β-phase. The α-phase is stable below 160 K down to the lowest temperature, and the β-phase is stable above 160 K up to the fusion at 175 K. The phase transition between the two phases was first considered to be a second order transition [1]. Later a dilatometric measurement showed that two phase transitions, a first order transition at 159 K and a second order transition at 156 K [2]. However the precise heat capacity measurements made by adiabatic calorimetry [3] observed only one transition of first order at 157.34 K. The transition could be easily overheated and undercooled.

The crystal structures of the α-phase and the β-phase were investigated by X-ray diffraction measurements for CH_3OH [4] and neutron diffraction measurements on CD_3OD [5,6]. The structure of the α-phase is orthorhombic with space group $P2_12_12_1$, $Z = 4$, $a = 0.48727$ nm, $b = 0.46411$ nm, $c = 0.88671$ nm with a unit cell volume of 0.20053 nm^3 at 15 K, in which the hydroxy groups form infinite hydrogen bonded chains (Fig. 9.1). The molecular geometry of CD_3OD in the α-phase is close to that in the gas phase, i.e. one of the deuterons of the methyl group and the deuteron of the hydroxy group are in the *trans* configuration (Fig. 9.1). The structure of the β-phase is orthorhombic with space group *Cmcm*, $Z = 4$, $a = 0.64090$ nm, $b = 0.71993$ nm, $c = 0.46490$ nm with a unit cell volume 0.21451 nm^3 at 170 K. A very strong diffuse scattering was observed for the β-phase,

suggesting some disorder existing in the phase, which may be due to orientational disorder of the molecule around the C-O axis. The extent of disorder differs in different experimental runs, indicating that the disorder depends on the thermal history.

In addition to these two phases, the amorphous phase and the metastable crystalline phase is known [6-9]. The amorphous phase can be obtained by vapor deposition at low temperature (T_g ~ 102 K) [7,8]. The metastable crystalline phase can be obtained by rapidly cooling the sample from the room temperature. The metastable phase was evidenced only by Raman spectroscopy [6], so that it is not certain that the metastable phase is identical to the mixture of the α-phase and the β-phase [9].

To the best of my knowledge, the investigations on the partially deuterated methanol have been limited to the spectroscopic work on the gas phase. In this chapter the results of thermodynamic study as well as the IR spectroscopic study of methanol and its deuterated analogs (CH_3OH, CH_2DOH, CHD_2OH and CD_3OD) in the solid phase are described.

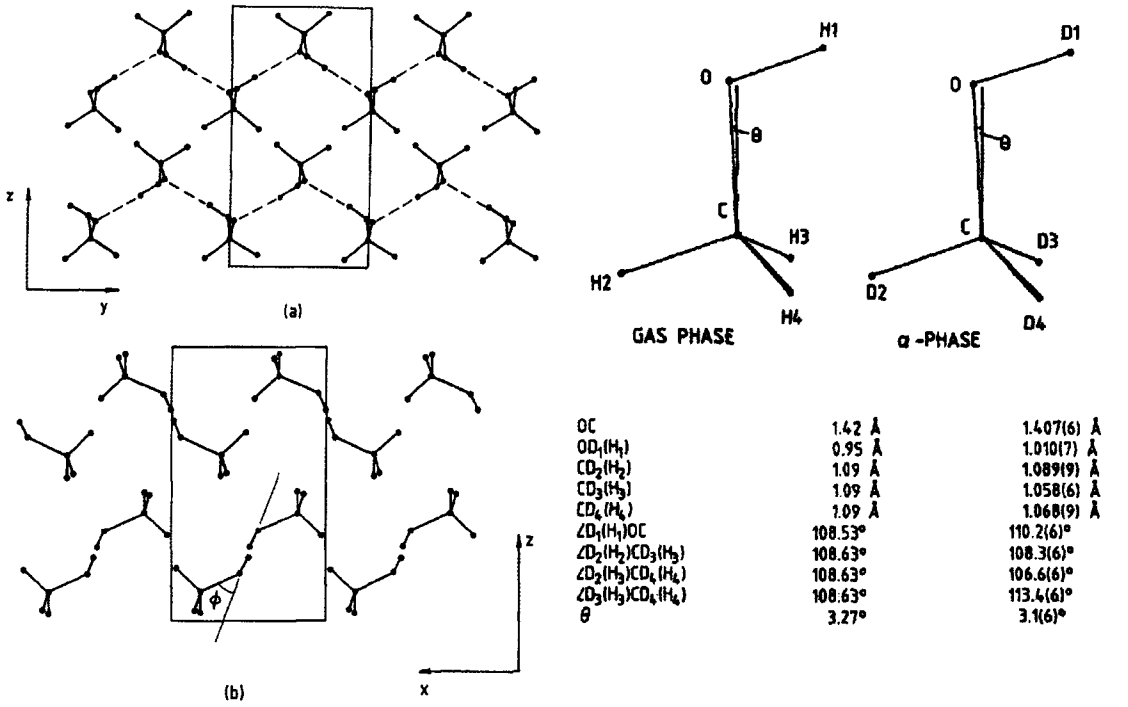

OC	1.42 Å	1.407(6) Å
$OD_1(H_1)$	0.95 Å	1.010(7) Å
$CD_2(H_2)$	1.09 Å	1.089(9) Å
$CD_3(H_3)$	1.09 Å	1.058(6) Å
$CD_4(H_4)$	1.09 Å	1.068(9) Å
$\angle D_1(H_1)OC$	108.53°	110.2(6)°
$\angle D_2(H_2)CD_3(H_3)$	108.63°	108.3(6)°
$\angle D_2(H_2)CD_4(H_4)$	108.63°	106.6(6)°
$\angle D_3(H_3)CD_4(H_4)$	108.63°	113.4(6)°
θ	3.27°	3.1(6)°

Fig. 9.1 (Left) Crystal structure of methanol in the α-phase showing the hydrogen bonding and the projection of the unit cell. (a) view down the *x*-axis, (b) view down the *y*-axis [5]. (Right) Geometry of the methanol molecule in the gas phase (CH_3OH) and the α-phase (CD_3OD) [5].

9.2 Experimental

9.2.1 Samples

CH_3OH was purchased from Wako Pure Chemical Industries. CH_2DOH (98%D), CHD_2OH (98%D) and CD_3OH (99.5%D) were purchased from CIL. The deuteration degrees were examined by NMR measurement. ^1H NMR (500 HMz, $CDCl_3$) δ 3.45 (protons of the methyl groups), 0.9 (1H of hydroxyl group). The deuteration degrees were obtained by taking the ratio of the integrals of these two peaks. The chemical purities were determined using the fractional melting method (Section 3.2.1), which were 99.976%, 99.789%, 95.807% and 99.943% for CH_3OH, CH_2DOH, CHD_2OH and CD_3OH, respectively. Since the purity of CHD_2OH was low, another sample of CHD_2OH was also purchased (C/D/N Isotope Inc. 99.2%D). The chemical purity of this sample has not been determined yet.

9.2.2 Heat Capacity Measurement

Heat capacity measurements were made between 5 K and 200 K by adiabatic calorimetry, and between 0.35 K and 20 K by relaxation calorimetry. The amounts of samples used for the adiabatic calorimetry were 1.71528 g (53.5326 mmol), 1.66122 g (50.2669 mmol), 1.81910 g (53.4179 mmol) and 1.83538 g (52.3491 mmol) for CH_3OH, CH_2DOH, CHD_2OH and CD_3OH, respectively, after buoyancy correction. For CHD_2OH, only the sample purchased from CIL (of not high purity) was measured by adiabatic calorimetry. For each sample, two types of phases were investigated, the rapidly cooled phase and the annealed phase. The first one was obtained by cooling the sample from the liquid phase with the rate of ~ -10 K min^{-1}. This phase showed exothermic behavior above 100 K due to some stabilization. The second phase was obtained by annealing the sample at 155 K for about an hour. The annealed phase is the homogeneous α-phase. The transition from the α-phase to the β-phase was detected around 160 K accompanied by huge endothermic heat due to the stabilization from the overheated α-phase to the stable β-phase. Such huge endothermic heat causes a loss of the adiabatic control of the calorimeter. This is because the adiabatic condition is achieved by taking the power balance between the cold source from coolant, such as liquid nitrogen or helium and the hot source from the heater coil. Since the former power cannot be regulated finely, the temperature of the outer adiabatic shield can easily be out of control when the temperature of the sample suddenly drops. For this reason, the data points are missing around the phase transition (see Fig. 9.2).

For relaxation calorimetry, both the rapidly cooled phase (~ -6 K min^{-1}) and the annealed phase (annealed at 155 K for 1 h) were investigated. The amounts of sample used for the relaxation

calorimetry were 0.370 mg (11.6 μmol), 0.340 mg (10.3 μmol), 0.307 mg (9.02 μmol) and 0.427 mg (12.2 μmol) for CH_3OH, CH_2DOH, CHD_2OH and CD_3OH, respectively. The copper liquid sample cells were used (Section 3.1.5, Case 2). The sample amounts for the relaxation calorimetry were determined referring the heat capacities of adiabatic calorimetry. For CHD_2OH, the sample purchased from C/D/N Isotopes was also investigated by relaxation calorimetry below 40 K. The amount of this sample was 0.344 mg (10.0 μmol). In the discussion of the low temperature heat capacities of CHD_2OH, the results of this sample are described unless otherwise noted.

9.2.3 IR Measurement

Infrared absorption measurements were made between 6 K and 100 K in the spectral range from 400 cm^{-1} to 4000 cm^{-1}. Two pieces of KRS-5 single crystal plates were used as a sample holder instead of KBr plates because methanol dissolves KBr. The sample was first rapidly cooled down (~ – 100 K min^{-1}) to 100 K. After measuring the spectra of the rapidly cooled phase, the sample was annealed at 155 K for 1 h and then measured from 100 K to 6 K.

9.2.4 DFT Calculation

In order to support the interpretation of the IR spectra, quantum mechanical DFT computation was also made using the B3LYP method with 6-31G(d) basis set for all atoms. The calculations were made on single molecule for all compounds (CH_3OH, CH_2DOH, CHD_2OH and CD_3OH). The molecular geometries were first optimized and then the IR spectra were calculated.

9.3 Results and Discussion

9.3.1 Heat Capacities

Fig. 9.2 shows the heat capacities of four compounds (CH_3OH, CH_2DOH, CHD_2OH and CD_3OH) over the whole temperature range. The step around 160 K is due to the phase transition between the α-phase and the β-phase. Several data points are missing at this temperature because the adiabatic control was out due to the endothermic stabilization. The heat capacity of rapidly cooled phase is almost equal to the annealed one in the temperature range from 20 K to 150 K, indicating that the rapidly cooled phase mainly consists of the α-phase with small portion of the β-phase. The peaks around 175 K show the fusion.

At low temperature, $C_6H_5CH_2D$ and $C_6H_5CHD_2$ show a broad anomaly in heat capacity in both

the rapidly cooled phase and the annealed phase, while CH_3OH and CD_3OH do not show such an anomaly. Fig. 9.3 shows the low temperature heat capacities of CH_3OH and CD_3OH in the C_p/T^3 plot. The difference between the rapidly cooled phase and the annealed phase may be due to the difference in the density. Since the β-phase is less dense than the α-phase, the heat capacity of the rapidly cooled phase, which presumably contains the β-phase, is slightly larger than that of annealed one. The deviation from the T^3 dependence below 2 K for the rapidly cooled phases also indicates that these phases are disordered [10]. The similar deviation observed for the annealed CH_3OH may be due to the tunnel excitation of the methyl groups.

Fig. 9.4 shows the heat capacities of CH_2DOH below 20 K. It is interesting that the heat capacities of the two phases differ significantly to each other. The peak obtained after rapid cooling is smaller and shifted toward lower temperature comparing to the one obtained after annealing. This difference is much more distinct comparing to the results for CH_3OH or CD_3OH (Fig. 9.3). The excess contributions were obtained by subtracting the lattice heat capacities, which were estimated from the values of CH_3OH and CD_3OH with proper temperature scaling. Fig. 9.5 and Fig. 9.6 show the excess entropies and the excess heat capacities for CH_2DOH. The excess entropies are close to $R \ln 3$ for both phases, which is the value expected from the model of orientational ordering of the methyl groups. The excess heat capacity of the annealed phase was fitted well by the Schottky function with energy scheme of two levels. The upper level is doubly degenerated. However the excess heat capacity of the other rapidly cooled phase does not fit well to the Schottky function, which is broader than the model curve especially below 1 K. The broadening of the excess curve indicates the possibility of disorder existing in the phase. Indeed significant orientational disorder of the molecules in the β-phase was suggested from the diffraction measurements.

For CHD_2OH, unexpected long thermal relaxation was observed below 10 K for both phases. The relaxation time was much longer for the rapidly cooled phase than for the annealed phase. Since the rotation of $-CH_2D$ by 120° does not change the nuclear spin state, the long relaxation cannot be attributed to the spin conversion. Another possible explanation is that there was a small amount of CH_3OH in the sample together with some magnetic impurities which induced the spin conversion of $-CH_3$. However, similar relaxation was also observed for the other sample (the one purchased from C/D/N Isotope) which is presumably purer than the first one. The long relaxation seems to be intrinsic for CHD_2OH. Such a long relaxation makes it difficult to obtain accurate data by relaxation calorimetry, because it is indistinguishable with the relaxation of the calorimetry. In order to overcome this problem, the temperature monitoring time was extended ten times longer than the first time constant (τ_1) of relaxation calorimetry (Section 3.1.4). In general, the extension of the monitoring time of temperature is not preferable especially when the heat capacity is small, because it essentially involves the noise from thermal fluctuation. However, fortunately since the heat capacity of CHD_2OH is large at this low temperature range, the data were finally obtained with

relatively high precision. Fig. 9.7 shows the results of two phases, which is similar to CH_2DOH. The maximum of the heat capacity peak for the rapidly cooled phase is shifted to lower in temperature comparing to that of annealed one. The difference would be due to the same reason to that of CH_2DOH. Fig. 9.8 and Fig. 9.9 show the excess entropies and the excess heat capacities of CHD_2OH. The excess entropy of the annealed phase is much smaller than R ln 3, which is rather close to R ln (3/2). The excess entropy of the rapidly cooled one is similar but slightly larger than that for the annealed one. The excess heat capacity of the annealed CHD_2OH is explained by the energy scheme of two levels, in which the lower energy level is doubly degenerated. The degeneracy of the lowest levels explains the absence of excess entropy of R ln 2. Therefore the excess entropy function should be drawn as in Fig. 9.10, i.e. the entropy of the two degenerated ground states is not released even at the lowest temperature of the measurement (0.35 K). It is not certain whether the residual entropy of R ln 2 will be released or frozen at the lower temperatures. The larger entropy of the rapidly cooled CHD_2OH may be from the β-phase where the lowest levels may not be degenerated.

It should be noted that the energy levels for the annealed phase fulfill the inverse relation with each other, as in the case of 26DCT or 26DBT. The degeneration of the two levels shows that two orientations are energetically equivalent. The neutron diffraction measurement for CD_3OD revealed that the methyl group is oriented in a way that one of the deuteron of the methyl group locates on the *trans*-position to the proton of hydroxyl group [5]. If this is true for CH_2DOH and CHD_2OH, and if the intermolecular interaction is ignored, the two equivalent orientations for $-CH_2D$ or $-CHD_2$ would correspond to the two degenerated levels. It is also important that the energy spacing of the deuterated methanol is significantly larger than that of methyl iodide. Since the mass of hydroxyl groups is much smaller than the iodide, it is clear that the mass of the functional group connected to the methyl groups is not responsible for the energy spacing. The symmetry of the functional groups seems to be the main factor. Of course the influence from the intermolecular interaction is not negligible. However, considering the difference between the results of the rapidly cooled phase and the annealed phase, which is much smaller than the difference between methanol and methyl iodide, the influence of the intermolecular interaction seems still minor effect compared to that of the symmetry of the molecular frame.

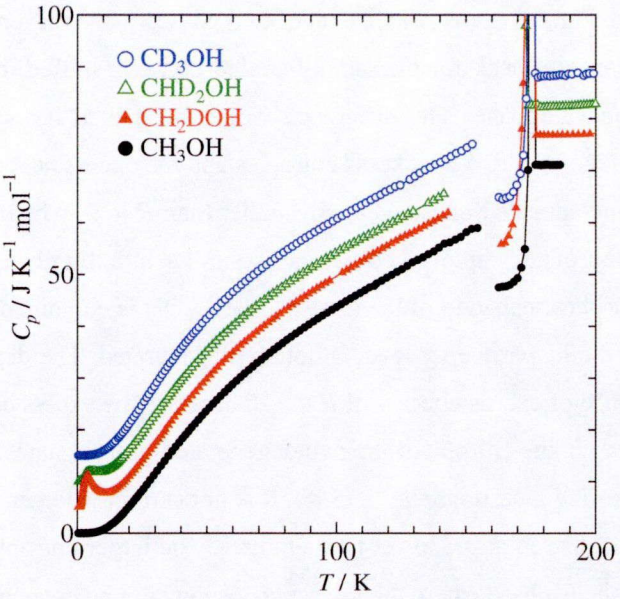

Fig. 9.2 Molar heat capacities of methanol and its methyl-deuterated analogs. The ordinate is for CH_3OH. The results for the other three compounds are successively shifted upward by 10 J K^{-1} mol^{-1}.

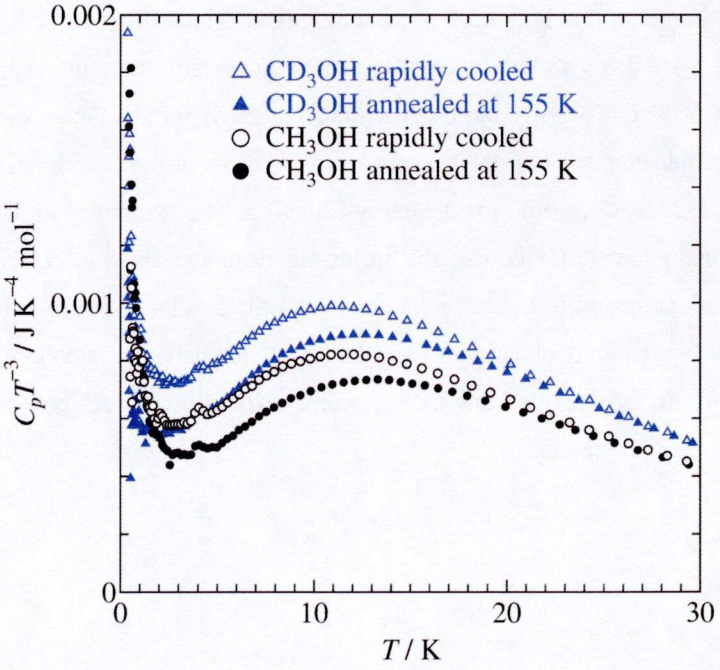

Fig. 9.3 C_p/T^3 plot for CH_3OH and CD_3OH for the rapidly cooled phases and the annealed phases.

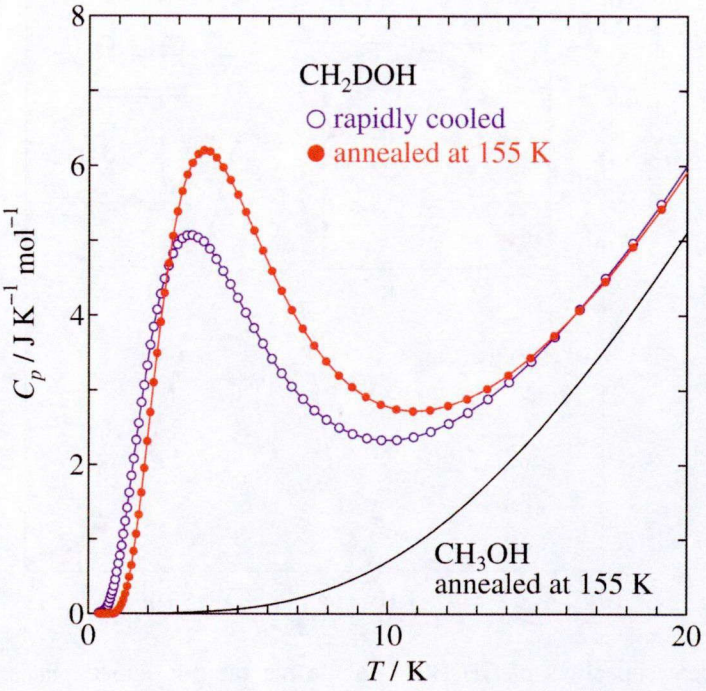

Fig. 9.4 Molar heat capacities of CH_2DOH below 20 K for the the rapidly cooled phase and the annealed phase.

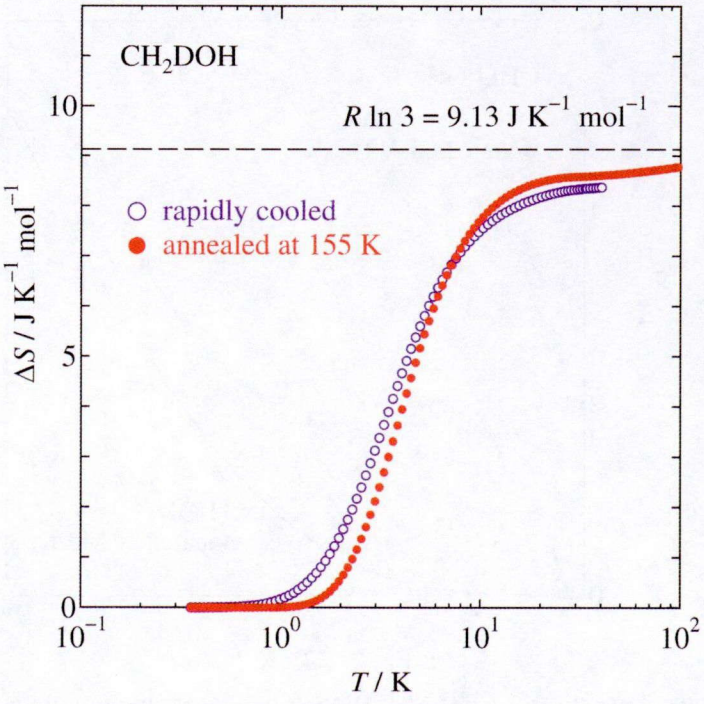

Fig. 9.5 Excess entropies of CH_2DOH for he the rapidly cooled phase and the annealed phase.

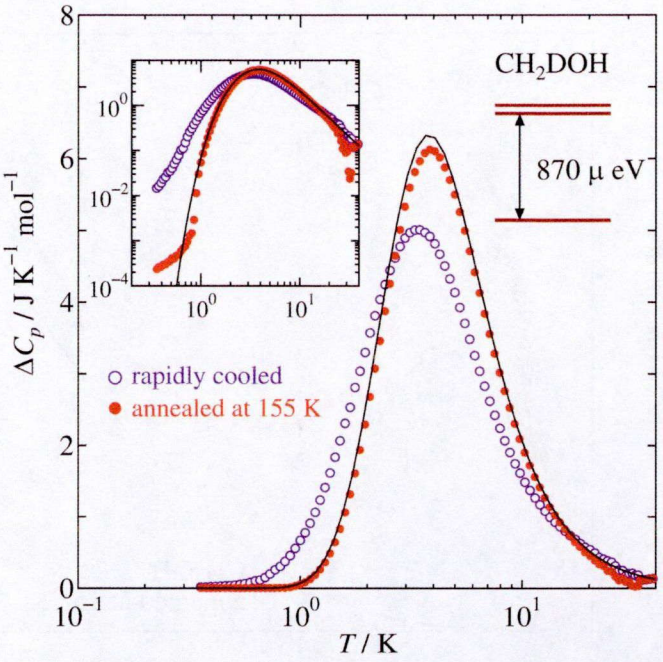

Fig. 9.6 Excess heat capacities of CH_2DOH for he the rapidly cooled phase and the annealed phase. The solid curves show the Schottky function calculated from the energy scheme shown in the figure. The inset show the double logarithmic plot.

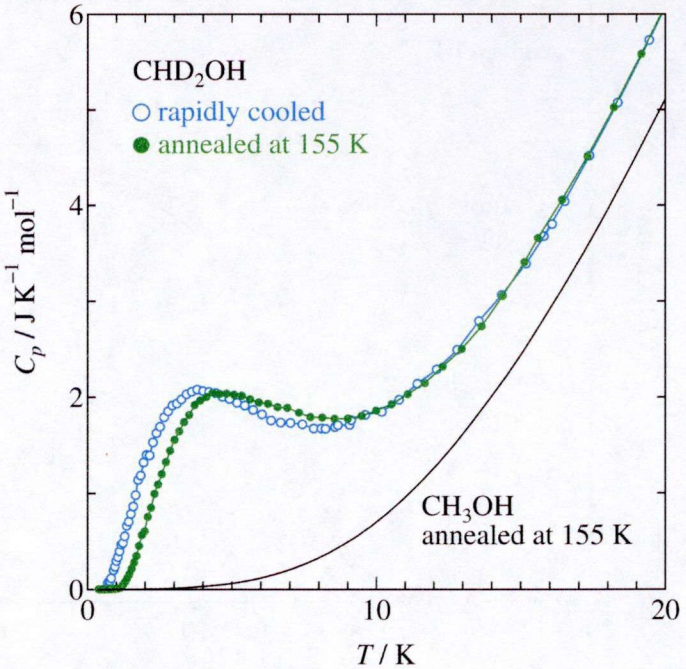

Fig. 9.7 Molar heat capacities of CHD_2OH below 20 K for he the rapidly cooled phase and the annealed phase.

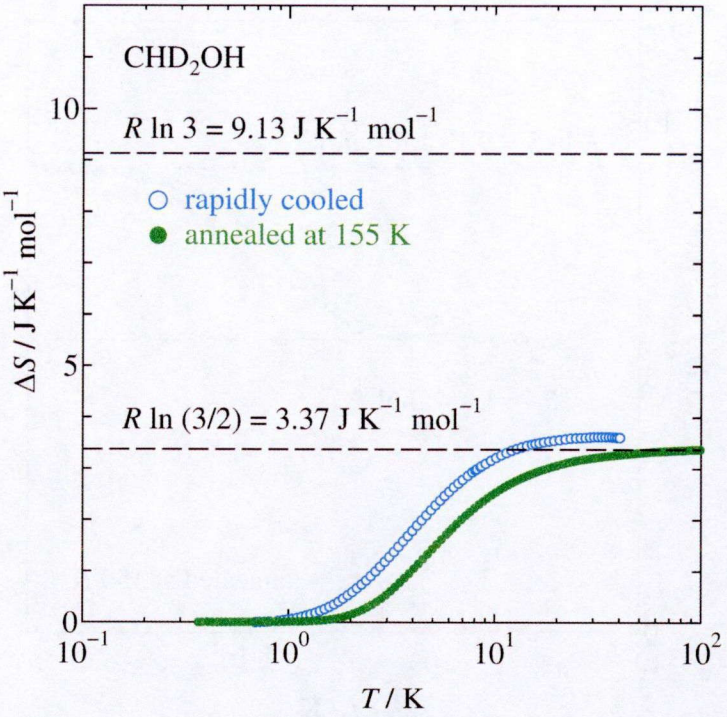

Fig. 9.8 Excess entropies of CHD_2OH for he the rapidly cooled phase and the annealed phase.

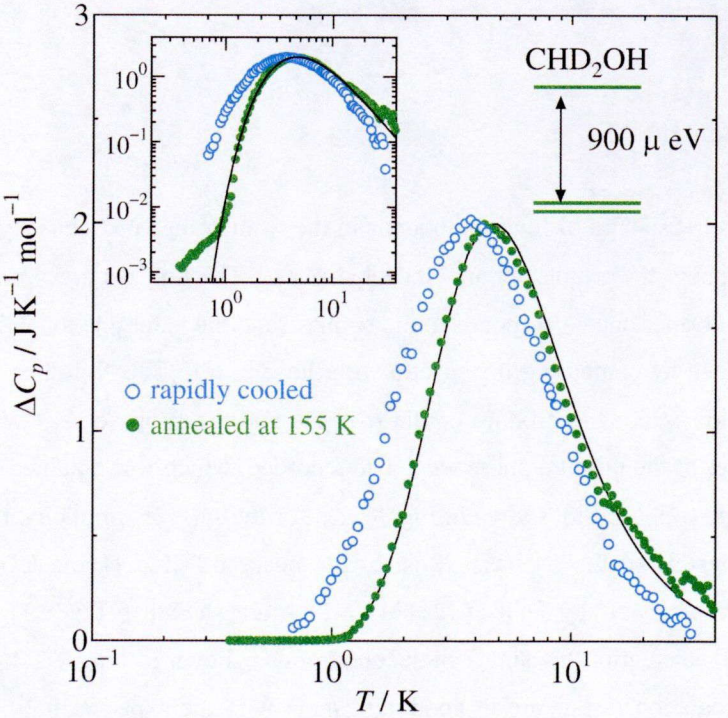

Fig. 9.9 Excess heat capacities of CHD_2OH for he the rapidly cooled phase and the annealed phase. The solid curves show the Schottky function calculated from the energy scheme shown in the figure. The inset show the double logarithmic plot.

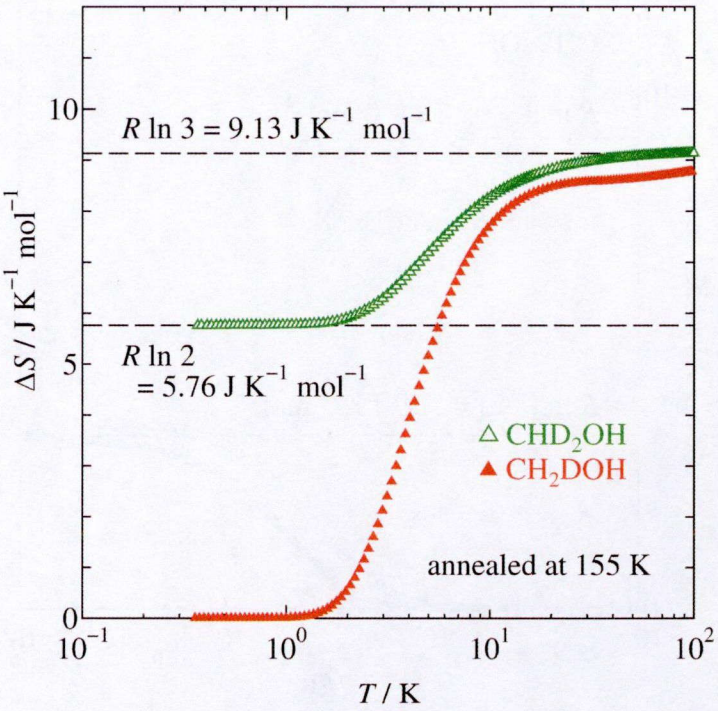

Fig. 9.10 The excess entropies of CH_2DOH and CHD_2OH for the annealed phase (α-phase). For CHD_2OH, the residual entropy of R ln 2 is assumed at the lowest temperature of the measurement, which derives from the degeneracy of the lowest levels.

9.3.2 IR Measurement

Fig. 9.11 shows the IR spectra of four compounds in the whole range of frequency registered at 6 K. The solid curves show the results for the annealed phase. The dotted curves are those of rapidly cooled phase. The former one corresponds to the α-phase and the latter one to the liquid glass. These phases were assigned by comparing the spectra with those in ref. [11]. Note that the rapidly cooled phase in this section is not the mixture of the α-phase and the β-phase as it was in the previous section. The spectra of the mixture phase were also recorded, which was obtained by rapidly cooling the sample from the β-phase (not shown in Fig. 9.11). For the sake of simplicity, the discussion here is limited to the results of the α-phase. Most of the peaks of CH_3OH and CD_3OH are assigned referring the previous report by Falk *et al.* [11], which are shown in Fig. 9.11 with arrows. The results of the DFT calculation for single molecule are also shown in Fig. 9.11 by bars below each spectrum. The calculation results are in good agreement with the experimental ones expect for the peaks associated with the motions of hydroxyl groups, which are extensively broader and shifted to lower frequencies in experiment due to the formation of hydrogen bond network in the crystal. The focus of the investigation is again on the C-H or C-D stretching modes of methyl groups. Suppose

that the results of DFT calculation for CH_2DOH and CHD_2OH have ~ 10% accuracy, the peaks around 2200 cm^{-1} and 2950 cm^{-1} observed in CH_2DOH and CHD_2OH are connected with the C-D and C-H stretching modes of methyl groups.

The temperature dependence of the peak intensities are investigated in the same analytical procedure applied to the previously described other compounds. Fig. 9.12 shows the temperature evolution of the IR spectra for CH_2DOH in the spectral range 2100 – 2300 cm^{-1}. The peak splitting may be due to the coupling with the vibrational modes of hydrogen bond network of the hydroxyl groups. The peaks in the spectra can be categorized into three groups, the peaks centered at 2145 cm^{-1}, the peaks around 2185 cm^{-1} and those around 2250 cm^{-1}. The first group diminishes with decreasing temperature, while the third one becomes stronger. The temperature dependence of the second groups is rather complicated, which is not used in the present analysis. The spectra were fitted by Voigt functions, and the temperature dependences of the components obtained by the fitting was investigated. Since the peak decomposition in each group was not quite, the total intensities were analyzed. The scaled intensities of two sets of peaks are consistent with the occupancy curves of two energy levels obtained from the Schottky heat capacity (Fig. 9.13).

Fig. 9.14 shows the temperature evolution of the IR spectra for CHD_2OH in the α-phase in the spectral range at 2880 – 2990 cm^{-1}. The peaks are also categorized into three groups, the peaks in the range from 2900 cm^{-1} to 2930 cm^{-1}, the single peak at 2940 cm^{-1} and the peaks in the range from 2950 cm^{-1} to 2980 cm^{-1}. The first group becomes stronger with decreasing temperature, while the third one becomes weaker. The second one does not depend on temperature. Since these peaks are located on the huge broad peak connected with O-H stretching mode, the second peak might be a part of it. The spectra were fitted and the intensities of the each component showing the same temperature dependence were summed up and then scaled. Fig. 9.15 shows the scaled intensities which agree well with the occupancy curves obtained from the Schottky heat capacity.

Fig. 9.16 shows the angle dependence of the frequency of C-D stretching mode in CH_2DOH obtained by DFT calculation for single molecule. The IR spectra in Fig. 9.12 show that the peaks diminishing with decreasing temperature are lower in frequency than that getting stronger with decreasing temperature. The former peaks correspond to the doubly-degenerated highest energy levels and the latter peaks correspond to the non-degenerated lowest level. Therefore the IR peaks at lower frequency correspond to the doubly-degenerated highest level and those of the higher frequency correspond to the non-degenerated lowest levels. According to the DFT calculation such a situation is possible for most of the rotational angle α except that $\alpha = 0$. Actually this result is inconsistent with the neutron diffraction measurement for CD_3OD [5], in which the orientation of $\alpha = 0$ is confirmed. The difference may come from the inaccuracy of the DFT calculation, in which the effect of hydrogen bond network is not taken into account. Another possibility is that the orientation of the methyl group varies with deuteration of the hydroxide groups which form the

hydrogen-bond network. The investigation for CH_2DOD or CHD_2OD may give some hint to solve this problem. Fig. 9.17 shows the angle dependence of the frequencies of C-H stretching mode in CHD_2OH obtained by the DFT calculation for single molecule. The IR spectra (Fig. 9.14) show that the peaks diminishing with decreasing temperature are higher in frequency than those getting stronger with decreasing temperature. This situation corresponds to the rotational angle $\alpha \neq 0$, which is consistent with the result of CH_2DOH, but again inconsistent with the neutron diffraction measurements for CD_3OD [5].

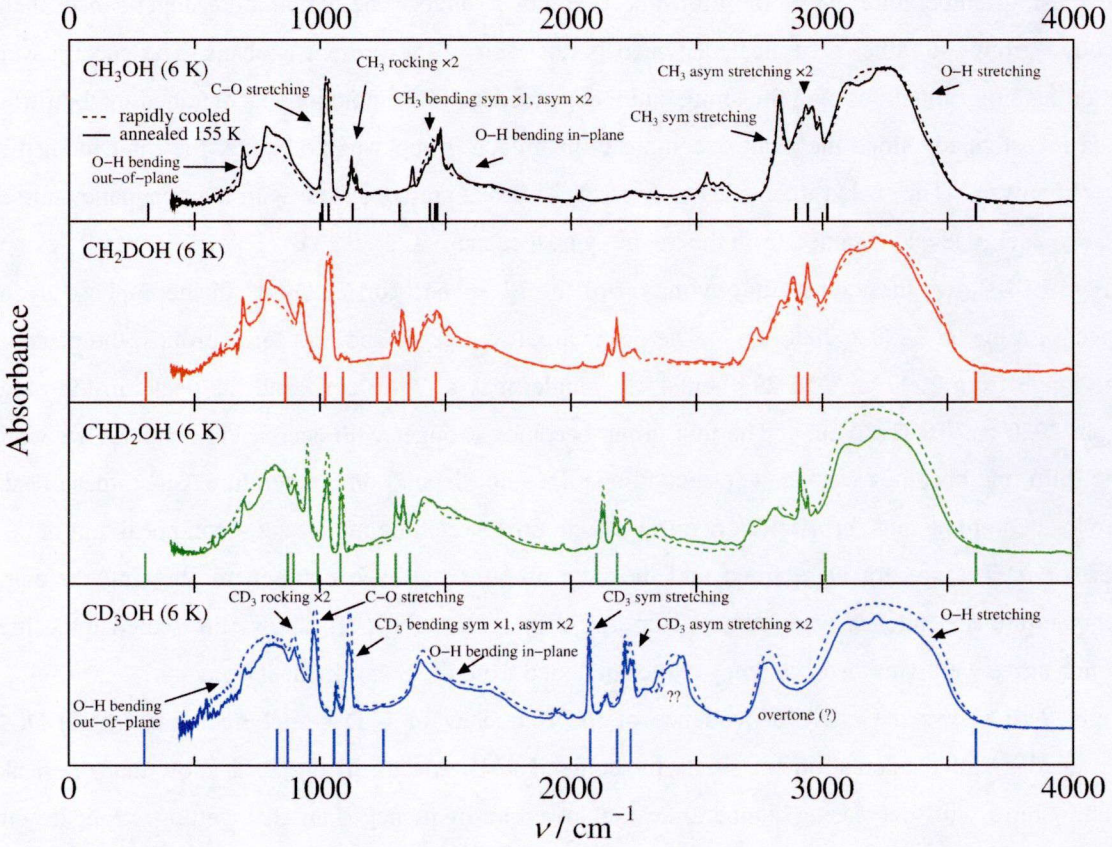

Fig. 9.11 The IR spectra of methanol and its methyl-deuterated analogs at 6 K in the spectral range 0 – 4000 cm^{-1}. The solid curves show the results for the α-phase. The dotted curves are those of the glass of liquid. The bars below the spectra show the frequencies of normal modes obtained by DFT calculation for single molecule.

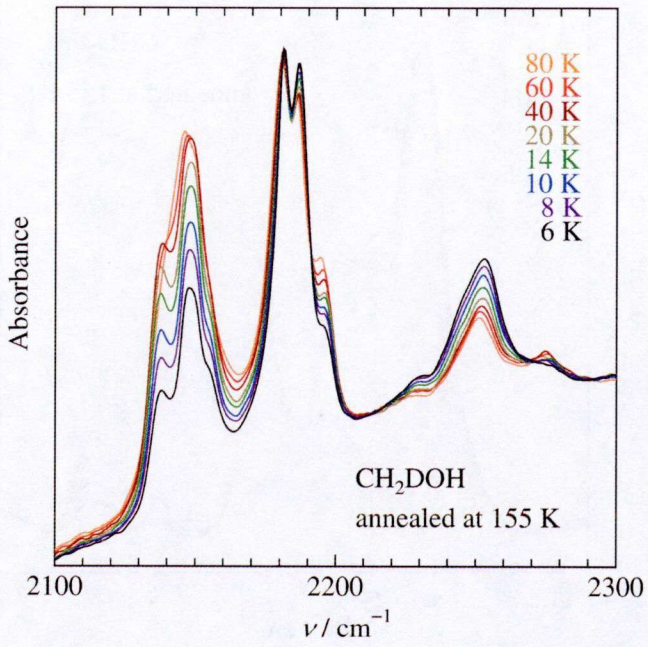

Fig. 9.12 The temperature evolution of the IR spectra for $C_6H_5CH_2D$ in the spectral range 2100 – 2300 cm^{-1}.

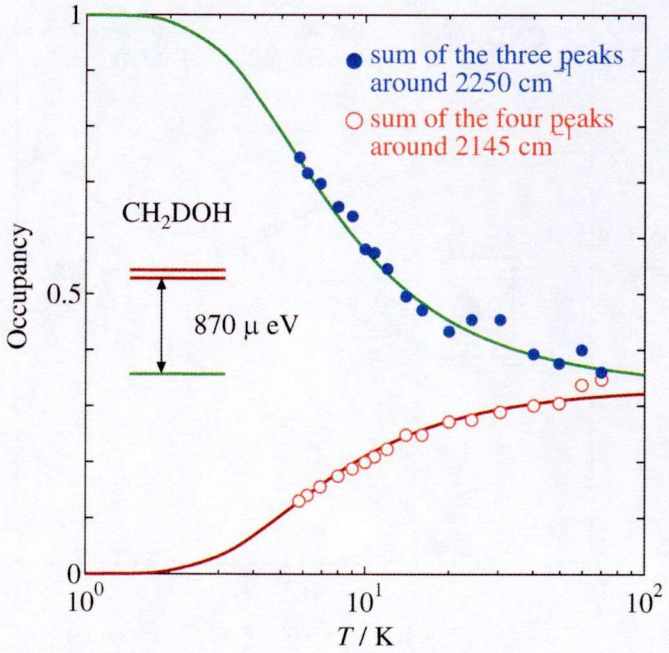

Fig. 9.13 Temperature dependences of the scaled intensities of two groups of peaks obtained for CH_2DOH (see Fig. 9.12), which are consistent with the occupancy for the two-level energy scheme obtained from the Schottky heat capacity (solid curves).

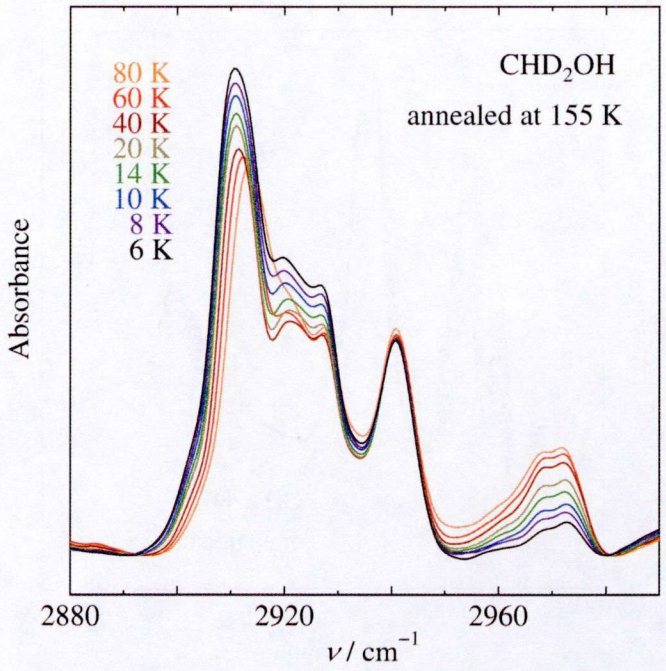

Fig. 9.14 The temperature evolution of the IR spectra for $C_6H_5CH_2D$ in the spectral range 2880 – 2990 cm^{-1}.

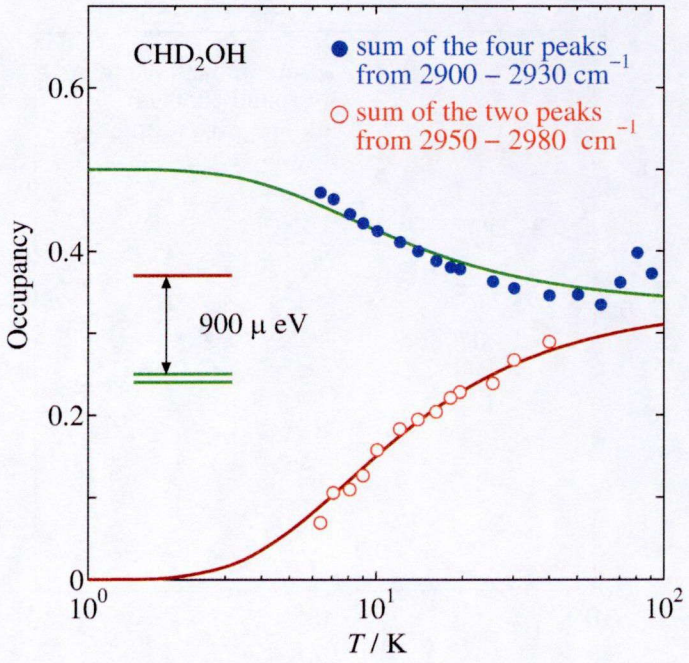

Fig. 9.15 Temperature dependences of the scaled intensities of two groups of peaks obtained for CHD_2OH (see Fig. 9.14), which are consistent with the occupancy for the two-level energy scheme obtained from the Schottky heat capacity (solid curves).

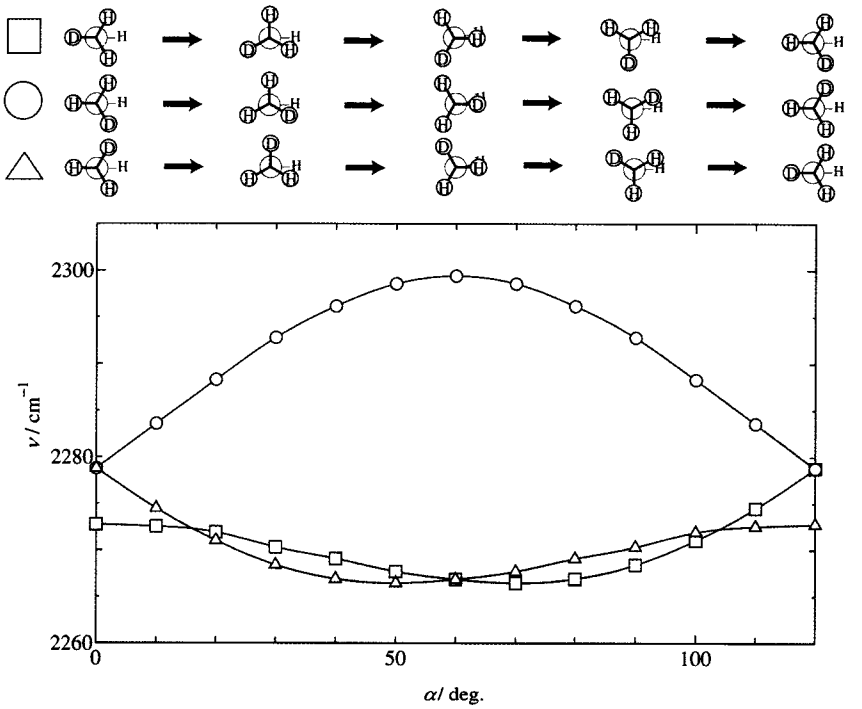

Fig. 9.16 Frequency of C-D stretching mode in CH_2DOH obtained by DFT calculation for single molecule. The pictures above the figure show the molecular configurations.

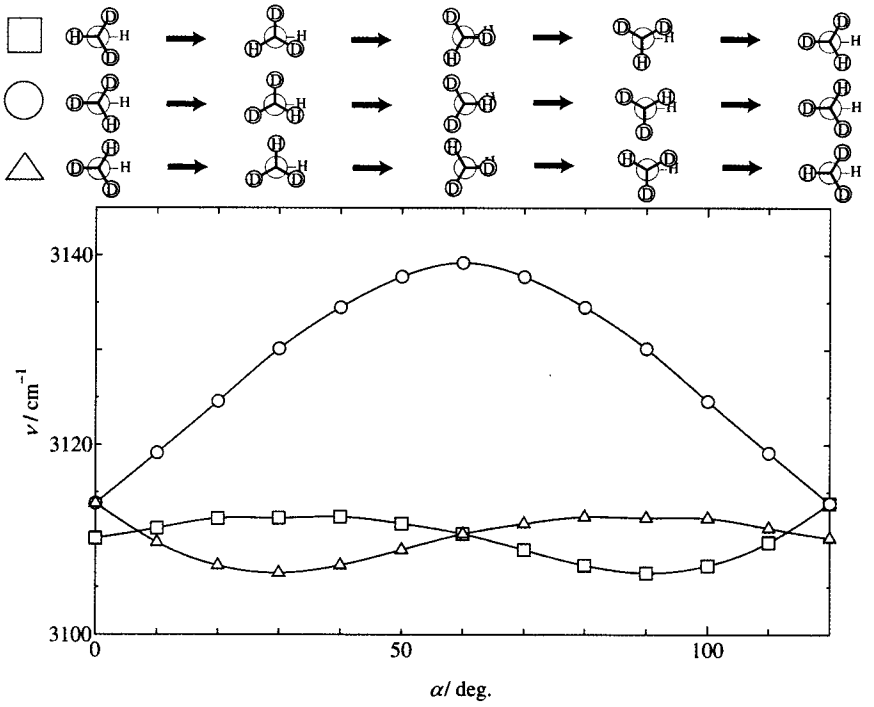

Fig. 9.17 Frequency of C-H stretching mode in CHD_2OH obtained by DFT calculation for single molecule. The pictures above the figure show the molecular configurations.

9.4 Summary

Heat capacity measurements were made for methanol (CH_3OH) and its methyl-deuterated analogs, (CH_2DOH, CHD_2OH and CD_3OH) between 0.35 K and 200 K by adiabatic calorimetry and relaxation calorimetry for two phases, the rapidly cooled phase and the phase annealed at 155 K for 1 h. The latter phase is the α-phase (the low temperature crystalline phase) while the former one is presumably the mixture of the α-phase and the β-phase. A broad excess heat capacity was found for the both phases of CH_2DOH and CHD_2OH. The excess entropy of CH_2DOH in the α-phase was about R ln 3 (= 9.13 J K^{-1} mol^{-1}) while that of CHD_2OH was R ln (3/2) (= 3.37 J K^{-1} mol^{-1}). The excess heat capacities were explained by an energy scheme of two levels. The upper one of the levels for CH_2DOH and the lower one for CHD_2OH are doubly degenerated, showing the inverse relation of the energy levels like 26DCT and 26DBT. The degeneration of the lower levels of CHD_2OH is the reason of missing entropy by R ln 2. For the rapidly cooled phase, the excess heat capacities were broader and shifted lower in temperature compared to those of the α-phase for both compounds. The broadening may be due to the orientational disorder of the molecule around the C-O axis in the β-phase. The excess entropy for the rapidly cooled phase of CH_2DOH is close to R ln 3 while that of CHD_2OH is slightly larger than R ln (3/2), which is also due to the contribution of the β-phase.

Infrared absorption measurements were also made for the four compounds (CH_3OH, CH_2DOH, CHD_2OH and CD_3OH) between 6 K and 100 K in the range from 400 cm^{-1} to 4000 cm^{-1}. The peaks connected with C-H or C-D stretching modes for CH_2DOH and CHD_2OH in the α-phase show strong dependence of their intensities on temperature. The scaled intensities of the peaks agree well with the occupancy curves of the two levels under the Boltzmann distribution obtained from the excess heat capacity.

Using the results of calorimetry, IR spectroscopic and DFT computation for the single molecule, the orientations of the methyl groups were estimated to be that one of the hydrogen atoms is in the *cis*-position to the proton of hydroxide group. This result is however inconsistent with the results derived from the neutron diffraction measurements for CD_3OD [5]. The deuteration of the hydroxyl group may influence the orientation of the rotor.

9.5 References for Chapter 9

[1] K.K. Kelley, *J. Am. Chem. Soc.* **51** (1929) 180.

[2] L.A.K.Staveley and M.A.P. Hogg, *J. Chem. Soc.* (1954) 1013.

[3] H.G. Carlson and E.F.Westrum, Jr., *J. Chem. Phys.* **54** (1971) 1464.

[4] K.J. Tauer and W.N. Lipscomb, *Acta Cryst.* **5** (1952) 606.

[5] B.H. Torrie, S.-X. Weng and B.M. Powekk, *Mol. Phys.* **67** (1989) 575.

[6] B.H. Torrie, O.S. Binbrek, M. Strauss and I.P. Swainson, *J. Solid State Chem.* **166** (2002) 415.

[7] M. Sugisaki, H.Suga and S. Seki, *Bull. Chem. Soc. Japan* **40** (1967) 2984.

[8] M. Sugisaki, H.Suga and S. Seki, *Bull. Chem. Soc. Japan* **41** (1968) 2586.

[9] O. Galvez, B. Mate, B. Martin-Llorente, V.J. Herrero and R. Escribano, *J. Phys. Chem. A* **113** (2009) 3321.

[10] *Amorphous Solids: Low temperature Properties*, ed. by W. A. Phillips (Springer, Berlin, 1981).

[11] M. Falk and E. Whalley, *J. Chem. Phys.* **34** (1961) 1554.

Chapter 10

Discussion and Conclusions

10.1 Summary

A series of investigations have revealed various important aspects of the orientational ordering of partially deuterated methyl groups in molecular solids. Table 10.1 shows the summary of the ordering processes and the associated entropies. The ordering process is categorized into two groups, cooperative ordering and non-cooperative ordering. The former one is accompanied by a phase transition, which was observed in 4-methylpyrdine (4MP) and lithium acetate dihydrate (LiAc) [1]. In both compounds, two methyl groups face to each other to form a coupled rotor. The interactions between the coupled rotors are also strong to form two-dimensional infinite chain network of interaction, which may be responsible for the cooperativity at the phase transition. In contrast to the results of LiAc, the transition entropies of partially deuterated 4MPs are significantly smaller than the expected value of (1/2) R ln 18, indicating two possibilities; either the freezing of the ordering or the existence of very low energy levels which were not observed in this study.

Another type of ordering, the non-cooperative one, was found in 2,6-dichlorotoluene (26DCT), 2,6-dibromotoluene (26DBT), toluene, methyl iodide and methanol. The non-cooperative feature is evidenced by the Schottky type excess heat capacities which presume Boltzmann distribution among the fixed energy levels. The energy schemes were obtained by fitting the Schottky functions to the excess heat capacities, which vary among different compounds. 26DCT shows the scheme of three levels. Methanol has two levels, one of which is doubly degenerated. 26DBT has three levels with some distribution in energy. Methyl iodide shows very small energy spacing. Toluene shows the freezing of orientational ordering where the occupancies of the levels do not follow the Boltzmann distribution.

The energy levels obtained from the heat capacity measurement correspond to the three ground torsional states of the methyl groups. The spacing from the lowest level is listed in Table 10.2 where "0", "1" and "2" denote the lowest, the middle and the highest one of the three levels. The values of two compounds (nitromethane and $(DMe\text{-}DCNQI)_2Cu$) reported in the past [2-4] are also added in

the table. It is interesting that the spacing of 0↔1 (1↔2) for -CH_2D is almost equal to that of 1↔2 (0↔1) for -CHD_2 for all the compounds investigated except for methyl iodide.

It seems that there is no correlation between the spacing of the ground torsional levels of -CH_2D or -CHD_2 and the tunnel frequency of -CH_3. From the view point of degrees of freedom, the three ground torsional states of -CH_2D or -CHD_2 correspond to the rotational tunneling states of A and E for -CH_3. Since the tunnel levels get lower with increasing the moment of inertia, the spacing between the levels also becomes smaller. The large energy difference among the levels for -CH_2D or -CHD_2, cannot be thus attributed to the simple mass effect on the rotational tunneling. From the other point of view, tunnel frequencies of -CH_3 is often used to estimate the barrier height of the potential. This is because the extent of tunneling (overlapping of the localized wave functions) depends on the potential width. If a sinusoidal curve is assumed for the potential surface like in Eq. (2.5), the width increases with the potential height. Stated another way, the larger tunnel frequency implies the lower potential barrier. Therefore the ground torsional levels of -CH_2D or -CHD_2, showing no correlation to the tunnel frequency of -CH_3, have little correlation to the magnitude of the potential barrier.

10.2 Discussion – Ground Torsional Levels of -CH_2D and -CHD_2 –

It is an important question which factor determines the energy scheme of the ground torsional levels for -CH_2D and -CHD_2. The energy scheme can be characterized by three aspects; (1) the absolute value of the spacing between 0↔2, (2) the ratio of the spacing between 0↔1 and 1↔2 and (3) the relation of the energy spacing between -CH_2D and -CHD_2. In all aspects, methyl iodide is different from the other compounds. The other compounds are common in the third aspect that the energy spacing between -CH_2D and -CHD_2 has inverse relation. For the second aspect, the compounds can be categorized into two types. One is that two levels have the same energy (doubly degenerated), which is observed for methanol and (DMe-DCNQI)$_2$Cu. The other one is that three levels have different energy, which is the case of all the other compounds (26DCT, 26DBT, toluene and nitromethane). The energy difference between the highest and the lowest levels (the first aspect) varies with different compounds ranging from 900 μeV to 3000 μeV.

There are several possible factors which can be responsible for the different ground torsional levels. One is the symmetry breaking of the three-fold rotational potential by deuterium substitution. If one or two of the three potential wells are deeper than the others, the energy levels of the torsional wave function in that well can be lower than the others. However interatomic interaction is generally determined by the electronic state which is not related to the nuclear mass, so the deuterium substitution itself does not deform the potential in principle. The indirect effect of the isotope

substitution to the interatomic interaction is possible, for example the shortening of C-H chemical bonds by isotope substitution. However according to the structural study of C_2H_2 and C_2D_2, the contraction of the C-H distance by the deuteration is less than 0.5% [5], which would not produce the energy difference of several meV.

Another possibility to explain the large energy difference is the mass effect on the zero point levels for each atom [6]. The point of this model can be illustrated by the example of two one-dimensional oscillators of masses M and m ($M > m$) in two wells with force constants F and f ($F > f$). There are two possible configurations (orientations); (1) M in the steep well (F) and m in the shallow well (f); (2) m in the steep well (F) and M in the shallow well (f). If the ground level of a configuration is expressed by the simple sum of the zero point energy of the two atoms, the harmonic approximation shows that the configuration of (1) is more stable than that of (2). If the same logic is applied to $-CH_2D$, the configuration that deuteron locates in the steepest well would be the most stable state. In the same way, the configuration that the deuteron is in the second steepest well corresponds to the middle level, and so on. Although this model looks reasonable, there is one important assumption hidden that the motions of two atoms (M and m) are independent of each other. This condition is not satisfied for the methyl group system because of the strong chemical bonds. Indeed if a methyl group is treated as rigid rotor, the identity of the atoms has no longer sense on the rotational state where only the value of moment of inertia can be used as an effective parameter. In that case, all the three levels must be identical if the potential is three-fold symmetric. Of course this is not always true because the methyl groups can be flexible enough to be distorted. Actually some structural studies of aspirin with partially deuterated methyl groups showed that the triangle formed by the three hydrogen atoms is isosceles rather than equilateral [7], which is the evidence that the rotor is not completely rigid under the crystal field. Nevertheless, the methyl groups still seem rigid so that the mass effect has minor contribution.

Another model explaining the large energy difference between the ground torsional levels of $-CH_2D$ or $-CHD_2$ is the rigid-top-rigid-frame model. The outline of this model has already been introduced in the theoretical section (Section 2.4.1). This model takes into account the rotation of the frame, the functional groups connected by the methyl groups. In this framework, the internal rotation is regarded as the twisting motion of the bond between the top and the frame. Therefore the moment of inertia is determined by the mass and the structure of top and frame as well as their relative configuration, which is called effective moment of inertia. If the top rotor is asymmetric, the effective moment of inertia shows angle dependence in its magnitude, which induces the difference in energy for different orientations. This model has been applied mainly on the behavior of gas phase where the intermolecular interaction is negligibly small. In order to apply this model to solid phases, a potential term of the frame has to be added to the total Hamiltonian in Eq. (2.12). For the torsioinal states, this contribution can be embedded in the potential term of $V(\alpha)$ in Eq. (2.13), so that the basic

theoretical treatment does not change except for the enlarged potential barrier of $V(\alpha)$. As mentioned in the theoretical section (Section 2.4.2), the energy difference calculated for CH_2DCHO are about 50 GHz (~ 200 μeV) and 35 GHz (~ 150 μeV). Although these values are ten times smaller than the values obtained in this study, considering the rough approximation of this model, it seems still acceptable offering a major reason of the large energy differences. In addition, the energy levels obtained from this model depend on the structure and symmetry of the frame connected to the asymmetric top, which is exactly what expected from the experimental results.

The larger energy spacing obtained in this study may come from the coupling of the torsion with other molecular motions. The experimental fact that the frequencies of the C-H (C-D) vibration vary with the orientation of the methyl groups explicitly shows that these stretching modes are coupled to the molecular dynamics of the frame. The angle dependence of the frequency indicates that the extent of coupling varies with the orientation of the rotor. Likewise it is quite probable that the torsion of the rotor is coupled to some modes of the frame.

Considering all described above, it was concluded that the difference in the ground torsional levels of $-CH_2D$ and $-CHD_2$ at three different orientations mainly derives from angle dependence of the effective moment of inertia which vary with the structure and the mass density of the top rotor (methyl groups) and the molecular frame. The coupling with other modes as well as the effect of flexibility in the methyl groups brings additional contribution.

In this framework, it is clear that two factors are responsible for the energy difference among the ground torsional levels; (1) the structure (and symmetry) of the frame functional groups and (2) the orientation of the rotor against the frame. If the frame is circular symmetric, the concept of "internal rotation" itself disappears, where the rotational angle is defined by the relative position to the unit cell of the crystal. The moment of inertia then depends less on the rotational angle, so that the energy levels tend to degenerate. This may be the case of methyl iodide. When the frame is not circular symmetric, the energy levels differ depending on the orientations. When the frame has plane symmetry and the methyl group is oriented to locate one hydrogen atom in the plane, the energy levels split into two, one of which is doubly degenerated. The non-degenereted state is the symmetric configuration in Fig. 2.3 and the doubly degenerated states are those of asymmetric configuration. This would be the case of methanol and $(DMe\text{-}DCNQI)_2Cu$. At least for methanol, the methyl groups are revealed to be in this configuration in the α-phase. When the methyl group is oriented that all the three hydrogen atoms are out of the frame plane, then the energy level split into three levels. This is the case of other compounds. Indeed neutron diffraction measurements have been revealed that the fully deuterated methyl groups of toluene (α-phase) [8] and nitromethane [9] have those orientations. For 26DCT, even though the crystal structures have not been clarified yet, the orientation expected in this study is also the same kind that all the hydrogen atoms pointing out from the frame plane. For 26DBT, however, the orientations of the rotor expected in this study is

that one hydrogen atoms is on the plane of 2,6-dibromobenzene, which is inconsistent with what expected from the model above. The difference may come from the interpretation of the IR spectra where the angle dependence of the C-H (C-D) stretching mode obtained by DFT calculation (Fig. 6.11 and Fig. 6.12) is linked to the IR frequencies observed. It is obvious that the analysis using the plot of Fig. 6.11 or Fig. 6.12 is too rough to detect the difference of small angle difference. Since the heat capacity reflects the ordering processes more sensitively than the other quantities in this work, it would be reasonable to conclude that the partially deuterated methyl groups in 26DBT seems to be oriented in the way that one of the hydrogen atoms is close to the frame plane, but not exactly on the plane. For the further investigation, neutron diffraction measurements are needed.

Table 10.1 Summary of the ordering processes and the associated entropies of seven compounds in solid.

	tunnel splitting $\nu_t(-CH_3)$ / μeV	entropy				ordering process	
		$-CH_3$	$-CH_2D$	$-CHD_2$	$-CD_3$		
lithium acetate dihydrate (LiAc) [1]	250	> 0	½ *R* ln 18	½ *R* ln 18	½ *R* ln 2	cooperative	perfect ordering
4-methypyridine (4MP)	519	0	< ½ *R* ln 18	< ½ *R* ln 18	½ *R* ln 2	cooperative	residual entropy
2,6-dichlorotoluene (26DCT)	0.56	0	*R* ln 3	*R* ln 3	0	non-cooperative	perfect ordering
2,6-dibromotoluene (26DBT)	4.0	0	*R* ln 3	*R* ln 3	0	non-cooperative	distribution in energy levels perfect ordering
toluene (α-phase)	28.5 26.0	0	< *R* ln 3	< *R* ln 3	0	non-cooperative	residual entropy (orientational glass)
methyl iodide	2.44	0	> 0	> 0	0	non-cooperative	small spacing between the energy levels
methanol (α-phase)	not known	0	*R* ln 3	*R* ln (3/2)	0	non-cooperative	perfect ordering ($-CH_2D$) degeneration of the ground level ($-CHD_2$)

Table 10.2 Summary of the non-cooperative ordering of partially deuterated methyl groups for seven compounds.

compound		tunnel splitting $\nu_t(\text{-CH}_3)$ / μeV	energy levels / μeV				degree of ordering
			$\text{-CH}_2\text{D}$		-CHD_2		
			0↔1	0↔2	0↔1	0↔2	
2,6-dichlorotoluene (26DCT)	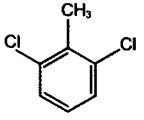	1.56	267	2700	2400	2950	perfect ordering
2,6-dibromotoluene (26DBT)	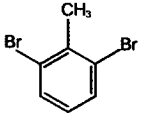	4.0	1200	1700	240	1700	perfect ordering
toluene (α-phase)	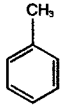	28.5, 26.0	(< 400)	~ 1300	(< 700)	~ 1300	freezing
methyl iodide	CH_3I	2.44	(~ 10)	(~ 10)	(~ 10)	(~ 42)	not certain
methanol (α-phase)	CH_3OH	not known	870	870	0	900	perfect ordering ($\text{-CH}_2\text{D}$) not certain (-CHD_2)
nitromethane [3]	CH_3NO_2	35.1	310	1991	1551	1897	perfect ordering
$(\text{DMe-DCNQI})_2\text{Cu}$ [4]	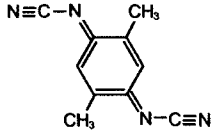 (DMe-DCNQI)	not known	1724	1724	not known	not known	perfect ordering

10.3 Conclusions

In this thesis, the results of the structural thermodynamic study on the orientational ordering of partially deuterated methyl groups in solids have been described in detail. One of the important discoveries is that the orientation of the methyl groups orders at low temperature in solid phase. When the methyl groups are partially deuterated, the ordering process can clearly be observed in low temperature heat capacities. The ordering occurs in either cooperative or non-cooperative manner. In the latter case, the energy differences among the three orientations were determined from the structure of the excess heat capacities. From the excess entropies, the freezing of ordering was also detected. From the energy difference of the levels derived from the heat capacity, various geometries of the methyl groups against the molecular frame were indicated.

The ordering process was also confirmed by IR spectroscopy, where the different orientations of the methyl groups provided different IR absorption peaks of the C-H (C-D) stretching mode. From the temperature dependence of the intensities of those peaks, each absorption peak was assigned to the three levels obtained from the heat capacity measurement.

The angle dependence of the absorption frequency was estimated from the DFT calculation of the single molecule. Comparing the results of calculation and the experimental spectra, possible orientations were determined. Combining these with the results of heat capacity measurement, the most stable orientation was also determined.

Since orientations of methyl groups in solids reflect the delicate balance of interactions, it is very difficult to expect them from the molecular calculation. In addition, it is also difficult to determine these orientations by X-ray diffraction measurements because of the small atomic scattering factor of hydrogen. Only the neutron diffraction measurement for the deuterated compounds provides the reliable information about the geometry of methyl groups in crystal. Therefore it is an achievement of this work that one possibility is demonstrated to determine the orientations of methyl groups by measuring the heat capacities of methyl partially deuterated compounds.

10.4 References for Chapter 10

[1] A. Inaba, unpublished.

[2] H.B. Brom, G. Mennenga, D. Cavagnat and L. Lascombe, *J. Phys. C: Solid State Phys.* **18** (1985) 3407.

[3] D. Cavagnat, H. Brom and R. Nugteren, *J. Chem. Phys.* **87** (1987) 801.

[4] Y. Nishio, Y. Mori, S. Sasaki, K. Kajita, S. Aonuma, H. Sawa, M. Tamura and R. Kato, *J. Phys. Soc. Jpn.* **71** (2002) 1701.

[5] L.S. Bartell, E.A. Roth, C.D. Hollowell, K. Kuchitsu and J.E. Young, Jr. *J. Chem. Phys.* **42** (1965) 2683.

[6] K.J. Lushington, K. Maki, J.A. Morrison, A. Heidemann and W. Press, *J. Chem. Phys.* **75** (1981) 4010.

[7] P. Schiebel, R.J. Papoular, W. Paulus, H. Zimmermann, A. Detken, U. Haeberlen and W. Prandl, *Phys. Rev. Lett.* **83** (1999) 975.

[8] R.M. Ibberson, W.I.F. David and M. Prager, *J. Chem. Soc., Chem. Commun.* (1992) 1438.

[9] S.F. Trevino, E. Prince and C.R. Hubbard, *J. Chem. Phys.* **73** (1980) 2996.